Characteristics and Meteorological Environment of Terrestrial Gamma-ray Flashes

Carolina Maiorana

Thesis for the degree of Philosophiae Doctor (PhD)
University of Bergen, Norway
2021

UNIVERSITY OF BERGEN

Characteristics and Meteorological Environment of Terrestrial Gamma-ray Flashes

Carolina Maiorana

Thesis for the degree of Philosophiae Doctor (PhD)
at the University of Bergen

Date of defense: 28.05.2021
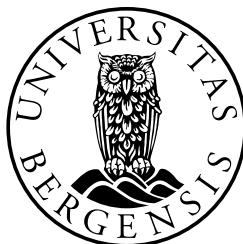
Year: 2021

Title: Characteristics and Meteorological Environment of Terrestrial Gamma-ray Flashes

Name: Carolina Maiorana

Print: Skipnes Kommunikasjon / University of Bergen

Scientific environment

This study was carried out at the Birkeland Centre for Space Science, University of Bergen. I was enrolled in the Science And Innovation with Thunderstorms (SAINT) group, a European Unions Horizon 2020 research and innovation program under the Marie Sklodowska-Curie Innovative Training Network (https://www.saint-h2020.eu/). The group is a collaboration between several European universities to investigate the fundamental mechanisms of atmospheric electrical discharges, combining observations, experiments and computer modeling and relying on a multidisciplinary approach. My project fell under the Work Package 2: "Satellite observations of thunderstorms".

Acknowledgements

Outline

This thesis consists of an introductory part and three scientific papers. The papers (chapter 7) have been published in international, peer-reviewed journal (Paper III is still in review).

1. C. Maiorana, M. Marisaldi, A. Lindanger, N. Østgaard, A. Ursi, D. Sarria, M.Galli, C. Labanti, M. Tavani, C. Pittori and F. Verrecchia, (2020) *The 3rd AG-ILE Terrestrial Gamma-ray Flashes Catalog. Part II: Optimized Selection Criteria and Characteristics of the New Sample*, Journal of Geophysical Research: Atmospheres **125/11**

2. Lindanger, A. and Marisaldi, M. and Maiorana, C. and Sarria, D. and Albrechtsen, K. and Østgaard, N. and Galli, M. and Ursi, A. and Labanti, C. and Tavani, M. and Pittori, C. and Verrecchia, F., (2020) *The 3rd AGILE Terrestrial Gamma-ray Flashes Catalog. Part I: Association to lightning sferics*, Journal of Geophysical Research: Atmospheres **125/11**

3. Maiorana, C. and Marisaldi, M. and Füllekrug, M. and Soula, S. and Lapierre, J. and Mezentsev, A. and Skeie, C. A. and Heumesser, M. and Chanrion, O. and Østgaard, N. and Neubert, T. and Reglero, V., (2021) *Observation of TGFs at Mid Latitude*, Journal of Geophysical Research: Atmospheres **-** (Under review, March 2021)

 I was also part of the following papers, which are not included in my thesis:

1. N. Østgaard, T. Neubert, V. Reglero, K. Ullaland, S. Yang, G. Genov, M. Marisaldi, A. Mezentsev, P. Kochkin, N. Lehtinen, D. Sarria, B. H. Qureshi, A. Solberg, C. Maiorana, K. Albrechtsen, C. Budtz-Jørgensen, I. Kuvvetli, F. Christiansen, O. Chanrion, M. Heumesser, J. Navarro-Gonzalez, P. Connell, C. Eyles, H. Christian, S. Al-nussirat, (2019) *First 10 Months of TGF Observations by ASIM*, Journal of Geophysical Research: Space Physics, **124/12**

2. D. Sarria, P. Kochkin, N. Østgaard, N. Lehtinen, A. Mezentsev, M. Marisaldi, B. E. Carlson, C. Maiorana, K. Albrechtsen, T. Neubert, V. Reglero, K. Ullaland, S. Yang, G. Genov, B. H. Qureshi, C. Budtz-Jørgensen, I. Kuvvetli, F. Christiansen, O. Chanrion, M. Heumesser, K. Dimitriadou, J. Navarro-González, P. Connell, C. Eyles, (2019) *The First Terrestrial Electron Beam Observed by the Atmosphere-Space Interactions Monitor*, Journal of Geophysical Research: Space Physics, **124/12**

List of Abbreviations

AGILE Astrorivelatore Gamma a Immagini Leggero

ASIM Atmosphere-Space Interaction Monitor

BATSE Burst and Transient Source Experiment

BGO Bismuth-Germanium Oxide

CAPE Convective Available Potential Energy

CG   Cloud-to-Ground (lightning flash)

CGRO Compton Gamma-Ray Observatory

CID Compact Intra-cloud Discharge

CTT Cloud Top Temperature

CZT Cadmium-Zinc-Telluride

EIP Energetic In-cloud Pulse

ELF Extremely Low Frequency

ENTLN Earth Networks Total Lightning Network

GBM Gamma-ray Burst Monitor

*GLD*360 Global Lightning Dataset

GRB Gamma-Ray Burst

HED High Energy Detector

IC   Intra-Cloud (lightning flash)

ISS   International Space Station

LED Low Energy Detector

MCAL Mini Calorimeter

MMIA Modular Multi-spectral Imaging Array

MXGS Modular X- and Gamma-ray Sensor

RHESSI Reuven-Ramaty High Energy Solar Spectroscopic Imager

ROI Region Of Interest

RREA Relativistic Runaway Electron Avalanche

TEB Terrestrial Electron Beam

TGE Thunderstorm Ground Enhancement

TGF Terrestrial Gamma-ray Flash

TLR TGF-to-lightning ratio

VHF Very High Frequency

VLF Very Low Frequency

WWLLN World Wide Lightning Location Network

Contents

Chapter 1

Introduction

Terrestrial Gamma-ray Flashes (TGFs) are sub-millisecond bursts of gamma radiation associated with lightning activity and are the manifestation of the most energetic natural particle acceleration processes on Earth. The goal of this thesis is to explore the impact of geography and the seasonal cycle in their production and the characteristics of the parent storms. TGFs were first discovered in 1991 by the Burst and Transient Source Experiment (BATSE) instrument onboard Compton Gamma-Ray Observatory and have subsequently been studied by a few other missions: Reuven Ramaty High Energy Solar Spectroscopic Imager (RHESSI) (*Smith et al.*, 2005), now decommissioned; Astro-rivelatore Gamma a Immagini Leggero (AGILE) (*Marisaldi et al.*, 2010); Fermi (*Briggs et al.*, 2013); and Atmosphere Space Interactions Monitor (ASIM) (*Neubert et al.*, 2019), launched in 2018.

CGRO, like all the other missions except ASIM, was designed for the study of high-energy astrophysics. The BATSE instrument was dedicated to Gamma Ray Bursts (GRBs), extremely energetic gamma-ray explosions thought to be produced by the collapse of massive stars or by merging of compact objects such as neutron stars. For this reason, the detection of events that were not only harder (i.e. composed by a larger fraction of more energetic photons) but also coming from the Earth side came completely unexpected: C. T. R. Wilson (*Wilson*, 1920) had predicted a few different energetic phenomena that could occur in the upper atmosphere, all subsequently observed, but in the case of TGFs had not predicted their energy range. The terrestrial origin of the bursts, as well as their connection with thunderstorm system was recognised since the beginning (*Fishman et al.*, 1994), however, scientists first attempted to connect them with the recently discovered sprites (*Fishman et al.*, 1994). As both phenomena were known better, though, it came out that TGFs were produced much lower in the atmosphere than sprites; so low, in fact, as to be directly linked with the lightning process inside a thundercloud. The already cited *Fishman et al.* (1994) suggested an altitude of production above 30 km (compatible with sprites) to avoid attenuation of the photons by absorption, but *Smith et al.* (2005) instead pointed to a lower altitude, as more absorption would explain the hardness of the TGF sample detected by RHESSI. The latter view proved the correct one, and TGFs have been explained as bremsstrahlung radiation produced by electrons accelerated inside the strong electric field of a thundercloud. In particular, they are directly associated with the initial phase of lightning discharges (*Cummer et al.*, 2005; *Inan et al.*, 1996). Various models have been proposed for the production process in detail. The key factor is the acceleration of electrons to rela-

tivistic speed, and there are two main theoretical frameworks to describe where and how this happens inside thunderclouds: acceleration and cascading multiplication of electrons inside a uniform ambient field (*Dwyer*, 2003; *Gurevich et al.*, 1992) and acceleration in the non-uniform field of the lightning streamers first, and in the field of the lightning leader afterwards. The lightning leader is a key player in the first scenario too, as its progression will greatly enhance the field in the space between itself and the charge reservoir towards which it is heading (*Dwyer*, 2003). Empirical evidence has remained ambiguous and both theories are currently still in the running. For this reason the focus of recent research has been on finding constraints for the production scenarios, by examining the characteristics of lightning discharges associated with TGFs, of the TGFs themselves, and the global distribution of TGF observations.

Between all missions, the list of TGF observations has grown long and a few questions have been answered, for example their duration and luminous intensity and their association with lightning discharges. Many more, however, are still eluding us, of which the most crucial are: how many TGFs are there, what is the exact relationship between TGFs and the lightning process, and how can thunderclouds develop the conditions needed for TGF production.

1.1 Objectives

One of the fundamental aspects in the physics of TGFs is the thunderstorm environment in which they are produced. A few studies have been conducted that specifically focused on it (*Chronis et al.*, 2016; *Fuschino et al.*, 2011; *Larkey et al.*, 2019; *Smith et al.*, 2010; *Splitt et al.*, 2010; *Ursi et al.*, 2019), but the high number of variables and unknowns at play means the question is still open. A few parameters have been identified and will be explored in Chapter 4, but a set of conditions that would predict the production of TGFs is still missing. Yet, TGFs are produced inside thundercloud, and so their detection has to follow meteorologic and climatic patterns around the globe. The goal of this thesis is to investigate the influence of meteorological and geographical conditions in TGFs production.

Papers I (*Maiorana et al.*, 2020) and II (*Lindanger et al.*, 2020) are two companion papers that focus on the construction of a new inclusive and consolidated TGF catalog for the AGILE mission. The large number of events allowed to focus on their geographical and seasonal characteristics. The papers are based on the TGF dataset from AGILE, which has a strictly equatorial orbit and thus covers regions which do not see great variations in meteorological conditions throughout the year; therefore, any trends in TGF detection can be ascribed to geographical patterns. However, an impact from the passage across the equator of the Inter Tropical Convergence Zone (ITCZ), which leads the alternance between dry and wet season, can also be observed.

Paper III (*Maiorana et al.*, 2021) instead takes a possible seasonal influence into account. The dataset used in this case was from ASIM, which covers the mid-latitude regions, up to $\pm 51°$. Among the previous missions, RHESSI reached the highest latitudes ($\pm 38°$), and so TGFs above this threshold are being observed for the first time. The paper also explores the geographic distribution of these mid-latitude TGFs, the characteristic of the storms that produced them and the role of atmospheric absorption in their rate of detection.

1.2   Outline

In chapter 2 we introduce the reader to the physics of atmospheric electricity: thundercloud electrification and inner electric field, the process of lightning discharge and the high-energy phenomena occurring in the atmosphere. Chapter 3 explores the characteristics and production process of TGFs and details the history of their observation by the various missions, with a particular focus on the AGILE and ASIM instruments. Chapter 4 describes the meteorological environment in which TGFs are produced and the relevant meteorological observations. Chapter 5 summarizes the results achieved by the papers and chapter 6 relates their conclusions in the context of the general aim of the thesis. Finally, all papers are presented in section 7.

Chapter 2

Introduction to Atmospheric Electricity

2.1 The electric field in a thundercloud

A thundercloud, also called a cumulonimbus cloud, is created when hot air from the ground rises upwards and is replaced by colder air in a convective cycle (*Cooray*, 2015). Under normal circumstances, the convection dissipates in about one hour, while under favourable conditions it can initiate new convective cells around itself (multicell storm) or become self-sustaining (supercell storm); in both cases, the lifetime of the storm will be much longer. Convection gives the cumulonimbus its characteristic tower shape. If the updraft is strong, the cloud can reach the tropopause, which acts as a barrier, and spread out (anvil clouds). An overshooting top is created by particularly strong updrafts, which penetrates into the tropopause for a few kilometers. As the altitude of the tropopause depends also on the latitude, the altitude reached by the cloud top can vary, from around 12 km at midlatitudes to 15 or more km at the equator; this has important consequences for TGFs, as described later.

The electrification of thunderclouds is thought to result from collision between water and ice particles inside the intense winds of the updraft. As they rise through the troposphere, the water droplets carried by the updraft cool down and reach the freezing temperature. Some droplets accordingly freeze into needle-like ice crystals, while others remain in the form of super-cooled liquid until $-40°$ C. These super-cooled droplets will attach to ice crystals on impact and the crystals will grow into bigger particles called graupel. As they become heavier, the graupel falls and collide with ice crystals moving upwards. Experiments in cloud chambers performed by *Takahashi* (1978) and *Jayaratne et al.* (1983) show that these collisions results in accumulation of positive charge at the top of the clouds, negative charge in the middle and again positive at the bottom; this effect is driven by the vertical temperature profile along the cloud.

Although the precise shape of the electric structure is more complex and dependent on the specific conditions, most thunderclouds can be described by a simplified model which includes a large, positive charge layer at the top, a large, negative charge layer in the middle, a small and sporadic positive layer at the bottom and a thin skin of screening negative charge at the very top (*Marshall and Rust*, 1991; *Vonnegut et al.*, 1962; *Williams et al.*, 1989; *Wilson*, 1920). Figure 2.1, taken from *Saunders* (2008), summarizes this simplified view of the electric field of a thundercloud, as well as the ice-graupel charging mechanism. Occasionally, this charge structure can be reversed, with the main negative charge above the main positive charge. Wide structures like
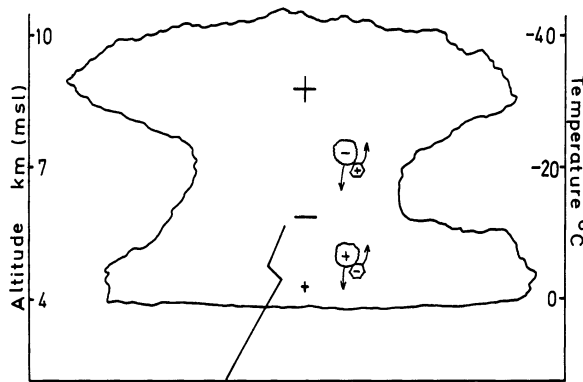
Figure 2.1: Tripole structure and charging mechanism at different altitudes of a thundercloud. From Saunders (2008).

Mesoscale Convective Systems (MCS) will have different structures in different regions (*Carey et al.*, 2005). The structure is also not static: the stage of the convective activity shows a strong relationship with the type and polarity of lightning flashes (*Williams et al.*, 1989), which is in turn dependent on the relative position of the main charge layers and the ground. For this reason, lightning activity has since been used to track the development and the severity of a storm.

2.2   Leaders, streamers and the lightning discharge process

Lightning discharges can be classified into several types, with the roughest distinction being based on whether they reach the ground or not. Flashes in the first category are called cloud-to-ground (CG), while the ones in the second category are called cloud discharges and can be intra-cloud (IC, between two charge layers of a single cloud), cloud-to-air (between a cloud and the surrounding air) or inter-cloud (between two clouds). Cloud discharges are by far the most common and IC in particular are the relevant ones when it comes to TGFs. The fraction of IC and CG lightning produced by a thundercloud depends on many factors, including its type and phase of development.
A further classification can be operated based on the polarity of the current. In this work we will define a positive lightning as one moving negative charge upwards as a net effect. An electric breakdown in a gap starts with cold discharges called streamers extending from one of the electrodes (in the case of lightning, usually the cloud). Streamers are column-shaped ionization fronts which move forward in air mostly due to photoionization occurring ahead of the front and are capable of propagating through the gap. Positive streamers have net positive charge at the tip and proceed from anode to cathode, while negative streamers have net negative charge at the tip and propagate from cathode to anode. In the case of a positive streamer, electrons from the surrounding air avalanche towards the streamer head and are absorbed into it, leaving behind a region of net positive space charge. If the electric field of this space charge is comparable to the ambient field (the so-called Meek criterion of streamer initiation, *Meek* (1940)), the space charge will attract secondary electron avalanches and increase in size as these electrons are neutralised inside it. The space charge will then advance towards

and eventually reach the streamer head, thus extending the streamer itself (*Cooray*, 2015). In the case of negative streamers, the electron avalanches proceed towards the anode, while the space charge is extended towards the cathode and induce emission of more electrons from the latter. The free electrons create a weakly conductive path between the cathode and the avalanche tip, which causes the streamer head to proceed further into the gap (*Cooray*, 2015). A leader is a hot, conductive channel formed by the joint stems of several streamers, which occurs when the temperature is high enough to produce thermal ionisation. It is formed by plasma in thermal equilibrium and is much bigger than a streamer: in the case of lightning, it has a diameter of a few cm and length of up to several km (*Rakov and Uman*, 2007). A positive leader extends positive streamers ahead, which will propagate as described and cause the leader to extend continuously into the gap. The propagation of negative leaders is slightly more complicated. The negative streamers cause the formation of a "space stem", a detached leader channel a few tens of meters ahead of the main channel (*Rakov and Uman*, 2007). This leader is bidirectional, with a positive head that propagates backwards towards the negative leader and a negative end that proceeds on the opposite side. When the original leader and the space stem are joined, the current in the channel is redistributed through a current wave that appears like a step, hence the name "stepped leader".

Around 90% of all CG lightning are initiated in the cloud. Negative CGs (-CG) lower negative charge from the cloud to the ground, while positive CGs (+CG) have the net effect of lowering positive charge, as electrons move towards the leader tip instead of ahead of it. The remaining portion of flashes instead proceeds from the ground to the cloud and can also carry either positive or negative charge. These "ground-to-cloud" flashes are initiated by the top of tall structures such as mountains or buildings taller than around 100 m (*Rakov and Uman*, 2007), which simultaneously behave as sharp tips at which electric field is enhanced and narrow the gap between ground and cloud. Figure 2.2 illustrates all four types of lightning flash, showing the initial leader and the polarity of the charge carried.

A downward -CG flash (*Dwyer and Uman*, 2014) starts with a pocket of charge of a few C, the stepped leader, making its way from the main negative charge region towards the ground. The leader conductivity is mostly due to free electrons, which have a much higher mobility than the heavier air molecules and ice particles. A stepped leader covers the distance between cloud and ground in about 20 ms, becoming faster as it approaches the ground and branching into several paths in the process. Once the leader tip is close enough to the ground, positive charge accumulates by induction in the ground beneath it and eventually initiates upward positive discharges that try to connect to it. When one of these discharges actually connects to the leader (a process called "attachment"), the lightning channel is complete and current can flow from the cloud to the ground; this is called return stroke and is the phase that is visible to our eyes. A first return stroke moves on average 30 kA, but currents up to around 100 kA have been recorded. In many cases, more charge is available after the first return stroke so subsequent ones can occur. After completion of one return stroke (in a series), a dart leader descends swiftly through the channel and is followed by another return stroke. The dart leader may turn into a stepping leader and even deviate from the previous path if this was interrupted, which means that CG lightning can make contact with ground at several locations. Dart leaders lower less charge than stepping leaders, and so subsequent
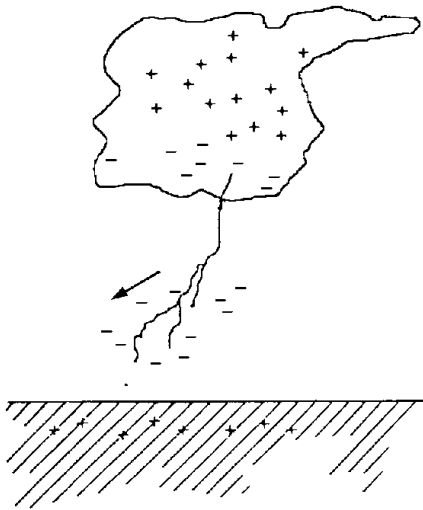
(a) Downward negative lightning
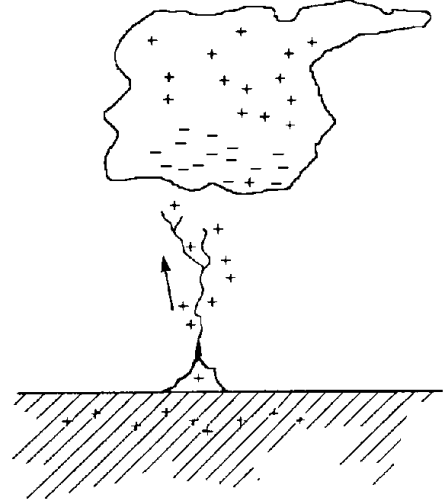
(b) Upward negative lightning
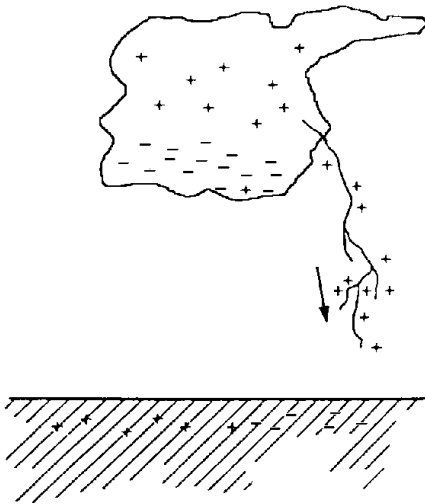
(c) Downward positive lightning
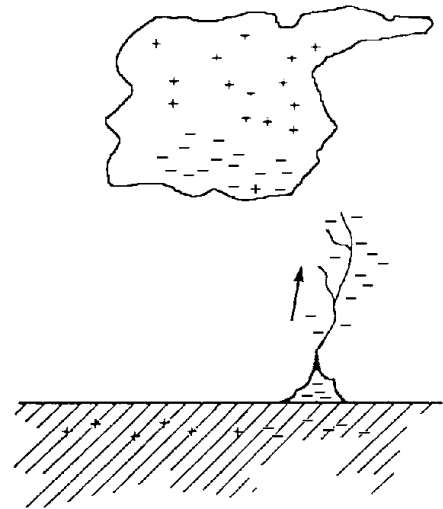
(d) Upward positive lightning

Figure 2.2: The four main lightning types: from left and clockwise, downward -CG, upward -CG, upward +CG and downward +CG. From Rakov and Uman (2007).

return strokes typically have lower and lower currents. Radio waves with characteristic shape are emitted in each phase and provide a valuable tool to infer the behaviour and magnitude of the charge.

+CG lightning can be initiated in either of the positive charge layers of a cloud. They do not branch as the negative leaders do, and tend to have no distinct steps. The lightning as a whole usually has only one return stroke, but that one can have currents that exceed 300 kA.

Cloud discharges (*Rakov and Uman*, 2007) are even less well understood than ground ones, since the fact that they happen entirely inside clouds makes them more difficult to observe. IC flashes connect the two main charge layers of the cloud, but more complex processes can happen due to a more complex structure of the electric field. They also consists of two phases, the early phase and the late phase. The early phase lasts for a few tens to a few hundreds of milliseconds and is thought to be very similar to the stepping leader of a -CG, with a small charge moving to bridge the gap between charge layers. The movement happens in a series of subsequent steps, each one emitting strong radio pulses. However, differently from CG flashes, the leader here is thought to be bidirectional, moving simultaneously towards the negative charge reservoir on one side and the positive one on the other. Once the leader stops propagating, negative charge (electrons) flows from the negative charge layer into the positive one, in a process that can be thought as the equivalent of a return stroke. Like with return strokes, this charge flow can happen in several waves, known as K-changes. This is the late phase of an IC flash.

The production of radio waves by the lightning channel is a very important feature for the study of lightning itself. The waves, called "sferics", are in frequency bands from ELF to VHF and are therefore easy to detect and record. They are an indirect measurement of the amount of charge involved, its polarity and the direction along which it is moving. Different frequencies are produced in different phases of the discharge, and so give insight into the whole process. The VLF portion (3 to 30 kHz) can travel without significant attenuation for thousands of km, being reflected by the ground and the lower ionosphere (the so-called Earth-ionosphere waveguide), so one can effectively detect lightning activity occurring on the other side of the planet. This allows lightning detection networks (see Section 4.4.1) to map flashes in real time across the globe. Finally, they are involved in the production of some of the phenomena that can happen in our atmosphere in conjunction with thunderstorms.

2.3   High-energy atmospheric physics

Lightning and the electric field in thunderstorms are associated with a number of high-energy phenomena that have all been discovered in the last few decades (*Dwyer et al.*, 2012a). Although C.T.R. Wilson had theoretically foreseen the production of highly energetic electrons in the atmosphere already in 1920, the first unequivocal observations came towards the end of the century. Figure 2.3 is an artistic representation of the main ones.

In addition to radio waves, lightning also emit X-rays. The evidence of this was very ambiguous, with some experiments detecting them, other not, other yet giving mixed results. *Moore et al.* (2001) was the first to report unequivocal detection of X-rays
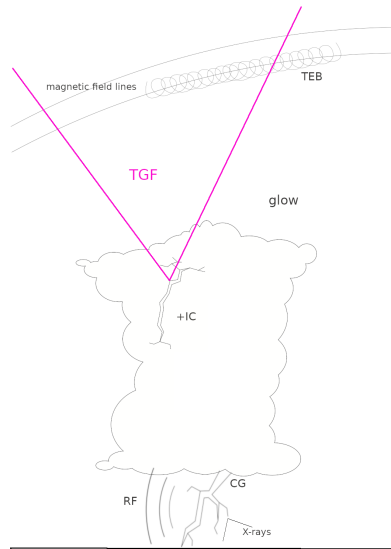
Figure 2.3: An artistic representation of the main high-energy atmospheric phenomena.

during the stepped leader phase of a flash. The conclusive evidence came from experiments with rocket-triggered lightning, in which a rocket attached to a metal wire is sent into the thundercloud and acts as a channel for the charge. Since the striking location is then known, it is possible to arrange the detectors as close as possible and at the same time shield them from other sources. The results (*Dwyer et al.*, 2003) showed intense bursts of X-rays during the stepping-leader phase, very similar to what had been observed in natural flashes but now with the certainty of their origin.

Electric field in thunderclouds and lightning activity are also associated with production of gamma rays (*Eack et al.*, 1996; *McCarthy and Parks*, 1985), photons with energies up to a few tens of MeV. The same acceleration mechanism (which will be explained in Chapter 3) responsible of TGF production can happen at lower flux and over bigger space and time scales (seconds to minutes), creating a steady glow of gamma radiation above vast portions of the thundercloud. Despite the common acceleration mechanism, the process as a whole is distinct from a TGF, that is, a gamma ray glow should not be considered as a dim, long-lasting TGF. The glow can be measured both from ground and from aircraft or balloons. The electric field in a thundercloud intensifies again after a flash, as more charge accumulates, and eventually reaches the threshold for the acceleration of electrons; this, in turn, keeps the field in a steady state by partially discharging it. It is then possible to have a continued emission of gamma rays as bremsstrahlung from the accelerated electrons. If a lightning flash occurs, however, charge is re-arranged and the field can drop below the threshold for acceleration and the emission is terminated, as it has been repeatedly observed. Glows can also be observed from ground, either by choosing a high-altitude site (*Chilingarian et al.*, 2010) or by studying storms with charge layers very close to the ground, like the winter storms over Japan (*Tsuchiya et al.*, 2011). The latter also compared glow spectra to measurements from spacecrafts (RHESSI and AGILE), thus suggesting that glows are also a brehmstrahlung emission. Glows observed from ground are sometimes referred to as

Thunderstorm Ground Enhancements.

Neutrons have also been observed in conjunction with lightning (*Chilingarian et al.*, 2010; *Enoto et al.*, 2017; *Shah et al.*, 1985). They probably result from photo-production as gamma photons collide with air nuclei and are therefore a valuable insight into the acceleration mechanism (*Babich and Roussel-Dupré*, 2007).

Finally, Terrestrial Electron Beams (TEBs) are also observed in association with lightning and TGFs (*Dwyer et al.*, 2008). The gamma photons of a TGF can produce new electrons via Compton scattering and pair production, and if this happens at 40-50 km of altitude these electrons are captured by the geomagnetic field and start gyrating along the field line. They can then travel up to the magnetic mirror and back, and hence be detected by a spacecraft twice. TEB can be recognised by the fact that they last at least a few milliseconds and that they appear associated with a lightning flash that is not directly beneath them, but under the footpoint of the magnetic line passing through the satellite that detected the TEB. Each TGF is associated with a TEB, but since the TEB is a very narrow beam it is much more difficult to observe.

Beside the high-energy ones, there exists another category of thunderstorm-related phenomena known as Transient Luminous Events (TLE). These do not involve high energies: they are optical emissions (elves, halos) or streamer discharges (sprites, blue jets) occurring high above thunderclouds and in association with lightning. In fact, sprites and jets can be seen as lightning discharges that connect to the ionosphere instead of to the ground. The physics of TLEs is different from the one of high-energy phenomena and outside the scope of this work. They are mentioned here for the sake of completeness, and because they are one of the main objectives of the ASIM mission, a key player for this study (see Section 3.1.1). Moreover, TGFs were initially thought to be associated with sprites. The association as was speculated in *Fishman et al.* (1994) and the early models has since been disproved, but the possibility of an indirect connection has recently resurfaced, as ASIM detected a few TGFs associated with lightning that also produced elves (*Neubert et al.*, 2020).

Chapter 3

Terrestrial Gamma-ray Flashes

3.1 Discovery and History of Observations

TGFs were discovered by chance by the space-borne instrument BATSE in 1991. BATSE's original sample consisted of 12 events (*Fishman et al.*, 1994), all with a duration on the order of a few millisecond but very different shapes in the temporal profile, sometimes with double or even multiple pulses. These characteristics were due to the fact that BATSE was designed for gamma astronomy and its trigger, designed for the much longer GRB, was operating on a 64 milliseconds window. Triggered systems only record data when certain conditions (in this case on the flux of incoming photons) are fulfilled. This saves up memory and telemetry but can introduce biases, especially when dealing with phenomena that have not been fully characterized yet, as TGFs were at the time.

After BATSE, RHESSI brought on a substantial improvement as all the event's data were downlinked: this allowed for a thorough search for TGFs, instead on relying on them triggering (*Grefenstette et al.*, 2009). Its germanium detectors cover the range between approximately 50 keV to 20 MeV. RHESSI's TGFs are significantly shorter than the BATSE sample, which was attributed to a bias caused by BATSE's trigger logic. At the time of RHESSI's decommissioning, its sample consisted of more than 3000 TGFs (*Smith et al.*, 2020), a much higher number than BATSE's rate of detection had implied. Moreover, this high number of detection allowed for cumulative spectral analysis of the TGFs (*Dwyer and Smith*, 2005) and for studies of geographic distribution. The spectral analysis, in turn, together with insight from lightning association, rejected the theory of emission associated with sprites in favour of a lower, in-cloud production altitude (*Cummer et al.*, 2005). RHESSI was also the first mission to report TGFs from mid latitude (*Smith et al.*, 2010), which is of particular interest for this study.

Fermi, a NASA mission for the study of cosmic gamma-ray sources, is also regularly observing TGFs. Onboard Fermi, the main instrument capable of detecting TGFs is the Gamma-ray Burst Monitor (GBM). It consists of 12 thallium-doped sodium iodide (NaI:Tl) detectors and two bismuth germanate (BGO) detectors. The former cover the energy range from 8 to 980 keV, the latter from 200 keV to 40 MeV and are thus the more important concerning TGF detection. Initially a triggered instrument, GBM has been operating in continuous mode since 2013, initially only over the regions where high production of TGFs is expected and then over the whole orbit (*Briggs et al.*, 2013). The trigger algorithm was also modified in 2009 to better detect TGFs and TEBs (*Fish-
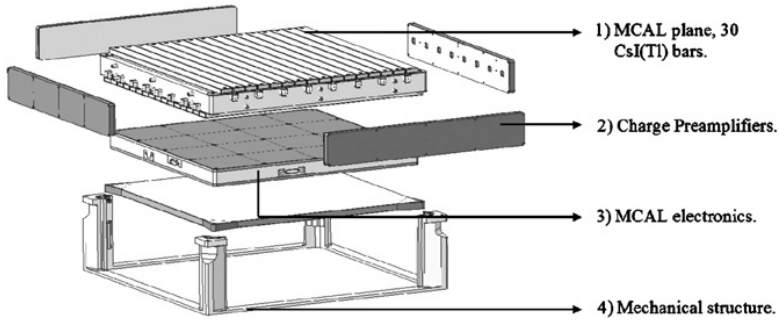
Figure 3.1: Schematic view of MCAL. Taken from Labanti et al. (2009)

man et al., 2011).

Table 3.1 summarises the specifications of the presented instruments. The two remaining missions, AGILE and ASIM, have been used in this study and so are described with more detail in the following section.

Spaceborne detectors remain the principal way to detect TGFs, but a small number of observations have been made from ground (*Abbasi et al.*, 2018; *Dwyer et al.*, 2012b; *Hare et al.*, 2016; *Tran et al.*, 2015).

Table 3.1: The instrumental characteristics of the main missions that observed TGFs.

Mission	Instrument	Year	Orbital Inclination	Detector type	Energy range	Triggered
CGRO	BATSE	1991-2000	28.5°	NaI(Tl)	20 keV - 2 MeV	Yes
RHESSI	-	2002-2018	38°	HP Ge	25 keV - 17 MeV	No
Fermi	GBM	2008 -	25.6°	BGO	150 keV - 30 MeV	Yes[1]
				NaI(Tl)	8 keV - 1 MeV	Yes
AGILE	MCAL	2007 -	2.5°	CsI(Tl)	300 keV - 100 MeV	Yes
ASIM	MXGS	2018	51.6°	BGO	300 keV - 30 MeV	Yes
				CZT	50-400 keV	Yes

[1] Changed to continuous mode in 2010.

3.1.1   Missions Used for this Study

AGILE

The Astrorivelatore Gamma a Immagini Leggero (AGILE) is a small satellite of the Italian Space Agency dedicated to gamma-ray astrophysics (*Tavani et al.*, 2009). Its payload includes several instruments, of which the Mini-Calorimeter (MCAL, shown in Figure 3.1) is the main one detecting TGFs. It is made of 30 thallium-doped cesium iodide (CsI:Tl) scintillator bars arranged in two superimposed planes, with orthogonal orientation of the bars; they are sensitive to the energy range from 300 keV to 100 MeV (*Labanti et al.*, 2009). The time accuracy of the instrument is $2\mu s$. Data saving happens on trigger and the TGFs are subsequently identified by an offline search. MCAL does not suffer from the duration bias of BATSE as it
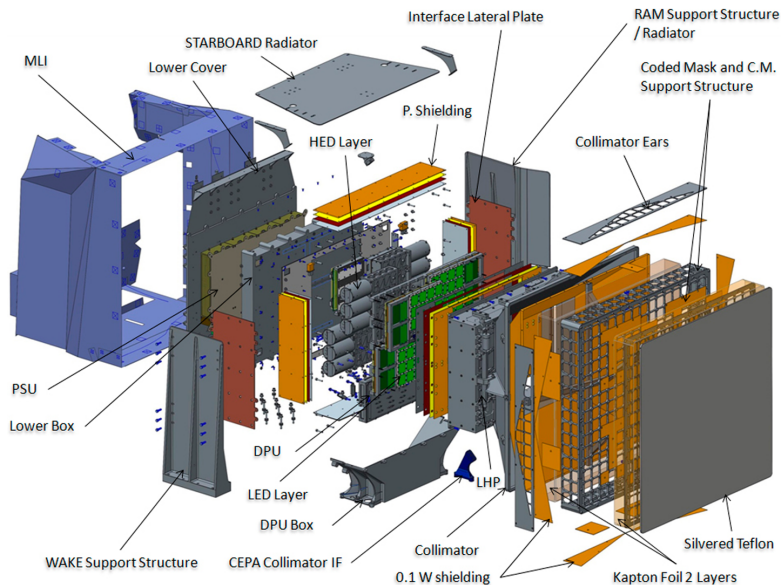
Figure 3.2: Schematic view of MXGS. Taken from Østgaard et al. (2019a)

was the first to introduce a shorter trigger window ($300\mu s$), which better fits the timescale of a TGF. In the first years, the dead time introduced by the anti-coincidence shield prevented the detection of events shorter than about $100\mu s$. This biased the sample towards longer duration and made the association with lightning sferics more unlikely, as this probability decreases as TGF duration increases (*Connaughton et al.*, 2013; *Dwyer and Cummer*, 2013). In March 2015 the anti-coincidence shield was switched off for MCAL and the TGF detection rate increases of one order of magnitude (*Marisaldi et al.*, 2015). It was also possible to match the new data with sferics from lightning detection networks (see Section 4.4.1). Association with lightning sferics also allowed to compensate for a failure in the internal clock that happened in 2015; the method is the subject of Paper II. Due to the very low orbital inclination, AGILE is only covering the equatorial region. This makes it particularly efficient in detecting TGFs, as those are among the regions with the highest production. Moreover, variations due to latitude are minimised and so the ones linked to season or longitude can be isolated with confidence. More detail on this can be found in Paper I.

ASIM

The Atmosphere-Space Interaction Monitor (ASIM) (*Neubert et al.*, 2019) is the first mission specifically dedicated to TGFs and TLEs. It was launched on April 2018 and it is placed on the Columbus module of the International Space Station (ISS). Because of its orbital inclination (see Table 3.1) it is also the first mission to cover temperate regions.

The scientific payload of ASIM is composed of two main instruments: the Modular X- and Gamma-ray Sensor MXGS (*Østgaard et al.*, 2019a), which is the one detecting TGFs, and the Modular Multi-spectral Imaging Array MMIA (*Chanrion et al.*, 2019). MXGS (Figure 3.2) in turn consists of two sets of detectors: the High Energy Detector (HED), sensitive to photons with energies from 300 keV to more than 30 MeV, and the Low Energy Detector (LED), which covers the range from 50 to 400 keV. HED consists of 12 Bismuth-Germanium

Oxide (BGO) scintillators organized in groups of 3 bars, each connected to a photomultiplier tube. It is always active, except when crossing the South Atlantic Anomaly (SAA). LED consists of 16384 pixels made of Cadmium-Zinc-Telluride crystals (CZT), with a coded mask to allow the reconstruction of the direction of arrival of the photons. It is only active on the nightside. MMIA is also only active at night. It is an optical detector with two cameras (337.0 nm and 777.4 nm) and three photometers sensitive in three different wavelength bands: 777.4, 337 and 180-240 nm. MXGS and MMIA have the ability to cross-trigger, with the goal of recording the flash associated with a gamma emission or, conversely, any high-energy photon that may be produced by a lightning. When cross-triggering, the two instruments have a relative time accuracy of $\pm 80 \mu s$ for events before April 2019 and $\pm 5 \mu s$ after, thanks to an update of the onboard software. Both instruments record and downlink 2 seconds of data around the trigger. MXGS operates over several trigger windows between $300 \mu s$ and 25 ms, specifically designed for TGFs. The time resolution is 28 ns for HED, $1 \mu s$ for LED and $10 \mu s$ for the MMIA photometers.

3.2 Observational Characteristics of Terrestrial Gamma-ray Flashes

The characteristics of TGFs have been established over the course of the years, putting together the different pictures that the different instruments were creating. Here we will discuss the intrinsic characteristics of the gamma emission, while Chapter 4 is dedicated to meteorological and geographical features and to the association with lightning.

Energy range. Energies of the photons have been reported up to around 40 MeV, making TGFs the natural process that produces the most energetic radiation on Earth. The intrinsic minimum and maximum values of the energy are however unknown, as the observations are limited by the sensitivity of the missions (most of which not built to observe TGFs), as well as affected by atmospheric interactions. Energies of about 100 MeV, which would be incompatible with the acknowledged production process process, were reported by AGILE (*Tavani et al.*, 2011). They were later explained as probably events of short duration and high flux being heavily affected by instrumental effects (*Marisaldi et al.*, 2019).

Fluence. The intensity distribution of TGFs follows a power law with exponent between -2.2 and -2.4, which is consistent across the samples from RHESSI, AGILE and Fermi (*Marisaldi et al.*, 2014; *Østgaard et al.*, 2012; *Tierney et al.*, 2013). As is the case with energy, measurement are affected by instrumental effects, including photon pileup and dead time of the detectors, and it is impossible to state the shape of the distribution outside the sensitivity range. The work of *Albrechtsen et al.* (2019), focused on observationally weak TGFs detected by RHESSI, found that the distribution seems to flatten out. *Smith et al.* (2020) instead address the other end of the spectrum and reports that the detectors of RHESSI are often paralysed by this type of events, which may mean that a significant portion of high-fluence events has so far escaped detection.

Spectrum. The cumulative spectrum of TGFs follows a power law with e-folding energy of around 7.3 MeV, as confirmed by both observations (*Dwyer and Smith*, 2005; *Marisaldi et al.*, 2014) and modeling (*Celestin et al.*, 2015; *Skeltved et al.*, 2017). The first spectra, obtained from the RHESSI and AGILE data, also supported the idea that TGFs are a bremsstrahlung emission from accelerated electrons (*Dwyer and Smith*, 2005; *Marisaldi et al.*, 2010; *Smith et al.*, 2005). Further comparison with models of atmospheric transmission put an upper limit to the altitude of production at about 20 km (*Carlson et al.*, 2007; *Gjesteland et al.*, 2010),

which corresponds to the altitude of the tropopause at tropical latitudes. The downside of cumulative spectra is that any specific detail about the structure of a single TGF is being lost in the averaging process. On the other end, obtaining the spectrum of a single TGF is not trivial, as one needs to find the middle ground between having a high enough photon count but a low enough flux to avoid deadtime-induced distortion. *Mailyan et al.* (2016) and *Mailyan et al.* (2019) present a sample of individual TGF spectra obtained from Fermi data and suggest there is significant individual variability among TGF sources.

Production altitude. The production altitude of TGFs was obtained from both the association with lightning sferics (see Section 4.1) and the analysis of the cumulative energy spectra. While the first data from BATSE and RHESSI seemed to imply a production altitude of at least 25 km (*Smith et al.*, 2005), further analysis including a better modeling of atmospheric interaction and instrumental effects reversed the conclusion, finding production altitudes between 12 and 20 km (*Carlson et al.*, 2007; *Dwyer and Smith*, 2005; *Hazelton et al.*, 2009; *Mailyan et al.*, 2016). These altitudes are compatible with the top regions of thunderstorms and the atmosphere immediately above, effectively ruling out a relationship with sprites. The connection between TGFs and lightning and thunderstorm is explored in detail in Chapter 4.

Duration. The durations of TGF are also heavily affected by the selection algorithms of the various mission. The estimates span from a few milliseconds for the BATSE sample, to a few hundreds μs for RHESSI (*Grefenstette et al.*, 2009), Fermi (*Roberts et al.*, 2017) and AGILE (*Maiorana et al.*, 2020), and even lower to below $100\mu s$ for ASIM (*Østgaard et al.*, 2019b). However, a direct comparison between the samples is not possible, as different collaborations have used different definitions of duration.

Beam morphology. Being the product of bremsstrahlung emission, TGFs have the shape of a cone with an opening angle that depends on the production model. Each production model is explained in Section 3.3. Here we will just state that the lightning leader models produce wide-beamed TGFs, while the big-scale electric fields of the relativistic feedback model give origin to narrow-beamed TGFs (*Carlson et al.*, 2009). The amplitude of the cone, combined with the position of the observing instrument, is one of the main obstacles in reconstructing the intrinsic energy spectrum of a single TGFs.

Pulse morphology. TGF usually present a single pulse of gamma radiation with fast risetime and a tail made of softer photons from Compton scattering (*Grefenstette et al.*, 2008; *Østgaard et al.*, 2008). The shape of the pulse can often be approximated with a gaussian or lognormal curve, in case of an asymmetric tail. Multi-pulse events have been reported by all missions (*Fishman et al.*, 1994; *Foley et al.*, 2014; *Maiorana et al.*, 2020; *Mezentsev et al.*, 2016; *Østgaard et al.*, 2019b). They can present different shapes, as illustrated in the two examples of Figures 3.3 and 3.4, from the samples of AGILE and ASIM respectively. For this reason, there is currently no confirmed explanation for the production of multi-pulse TGFs; the stepping process, or an ambient electric field that keeps going over and under the acceleration threshold are possibilities.

3.3 Mechanism for Production of TGFs

3.3.1 Relativistic Runaway Electron Avalanche

TGFs are produced when free electrons are accelerated to relativistic speeds by the electric field in which they are immersed and produce photons by bremsstrahlung. The process was first described by *Wilson* (1925), which also coined the term "runaway electrons" as there is
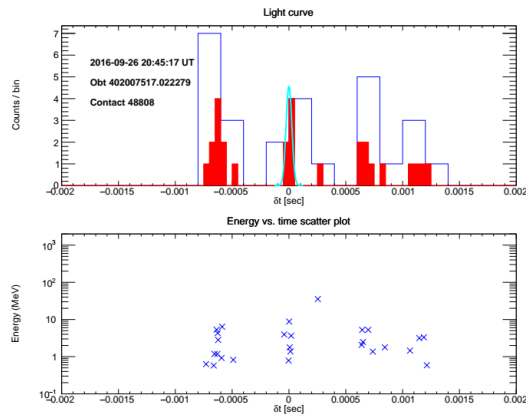
Figure 3.3: A multipeak event as imaged by AGILE. Top: the lightcurve (counts versus time); bottom: energy versus time. Taken from the third AGILE catalog (http://www.ssdc.asi.it/mcal3tgfcat).
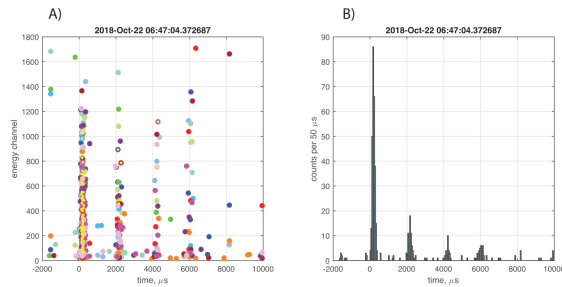

Figure 3.4: A multipeak event as imaged by ASIM (HED). Left: ADC channel versus time. Right: counts in 50μs bins versus time. Taken from Østgaard et al. (2019b).

a certain threshold of field intensity after which the energy gain from the electric field itself is greater than the energy loss from interaction with air particles, as illustrated in Figure 3.5, and therefore the electron will not stop. This threshold is called break-even field and depends on the density of air with respect to the sea-level value. Møller scattering (elastic scattering of electron over electron) can produce new electrons, which will also be accelerated by the field, resulting in a "snowball effect" (in Wilson's words) called Relativistic Runaway Electron Avalanche (RREA) (*Babich et al.*, 1998; *Gurevich et al.*, 1992). The theoretical threshold for the avalanche is only slightly higher than the break-even field, while in real atmosphere elastic scattering on both atomic nuclei and electrons, actually increases it of about 30% (*Dwyer*, 2003); however, this value remains within the range observed in real thunderstorms (*Rakov and Uman*, 2007).

As can be seen in Figure 3.5, the electrons need an initial, non-null kinetic energy in order to run away, which is smaller for greater electric fields. It is theoretically possible for the electric field to be so intense that electrons with any energy will run away; this is called "cold runaway", or "thermal runaway" (*Gurevich*, 1961). On the other hand, if the field is not strong enough, energetic electrons called seed particles are needed to initiate the process. Such free electrons are always present in the atmosphere, as a result of cosmic ray showers or, less commonly, radioactive decay from radon, but the electric field should grow to non-physical values or extend over unrealistically long distances to produce the intensities and energies of observed TGF through acceleration of the seeds alone. Additional processes are therefore necessary, and have been addressed by two separate models. The RREA mechanism is always the core part, but there is currently no consensus over where it happens. The relativistic feedback model is based on the effect of positrons and x-rays produced in the interaction of electrons with air; thermal runaway models have RREAs happen in the field of the streamer head first, and then at the leader tip. Both theoretical frames are analysed in more details in the following subsection, and illustrated in Figure 3.6. Observations so far do not allow to exclude one model in favour of the other and both models can be at play simultaneously.

3.3.2   Relativistic Feedback mechanism

This scenario explains the formation of a TGF through multiplication of free electrons via RREAs and multiplication of the RREAs with a mechanism called relativistic feedback (*Dwyer*, 2003). The free electrons are required to have an initial energy of about 1 MeV, and so need to be produced by other processes. It is commonly assumed that they are a byproduct of cosmic rays, but they might also be the ones produced by ionisation in front of streamer heads.

In this scenario, the accelerated seed electrons produce photons by bremsstrahlung, which in turn produce additional photons, electrons and positrons by Compton scattering and pair production. The positrons are then accelerated in the opposite direction and, if they reach high enough energy, they can travel long distances without annihilating, eventually reaching again the beginning of the avalanche region. Here they can produce secondary avalanches if they generate electrons via elastic scattering. Alternatively, the backscattered photons can produce electrons by Compton scattering, and these electrons can immediately create avalanches if the ambient conditions allow. Either way, there is an exponential multiplication of RREAs, which accounts for the flux of the TGFs observed from space. The (simplified) process is shown in Figure 3.7, taken from *Dwyer* (2003).
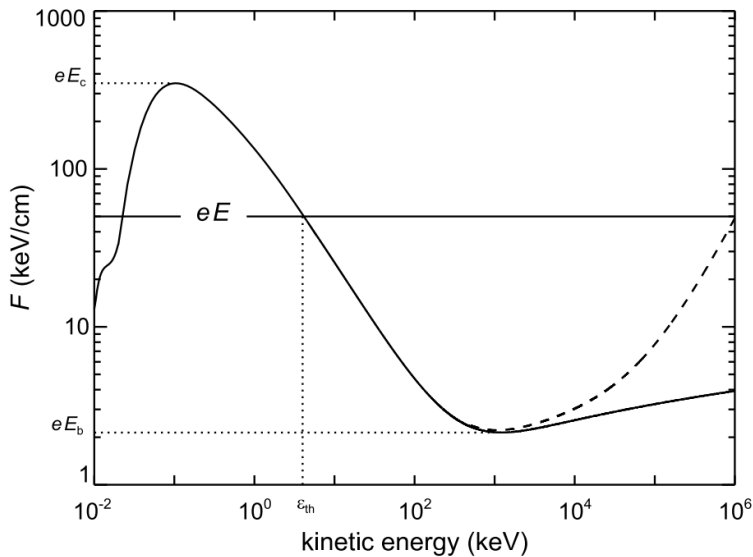
Figure 3.5: *The effective frictional force experienced by a free electron (or positron) moving through air at standard temperature and pressure as a function of kinetic energy. The solid curve represents inelastic scattering of the electron by air molecules, the dashed curve indicates the loss of energy due to bremsstrahlung emission. The horizontal line shows the electric force from a $5.0 \times 10^6 \mathrm{V/m}$ electric field. Runaway electrons occur for kinetic energies greater than the threshold energy. E_c is the critical electric field strength for which low-energy thermal electrons will run away, and E_b is the break-even field. Taken from Dwyer et al. (2012a).*
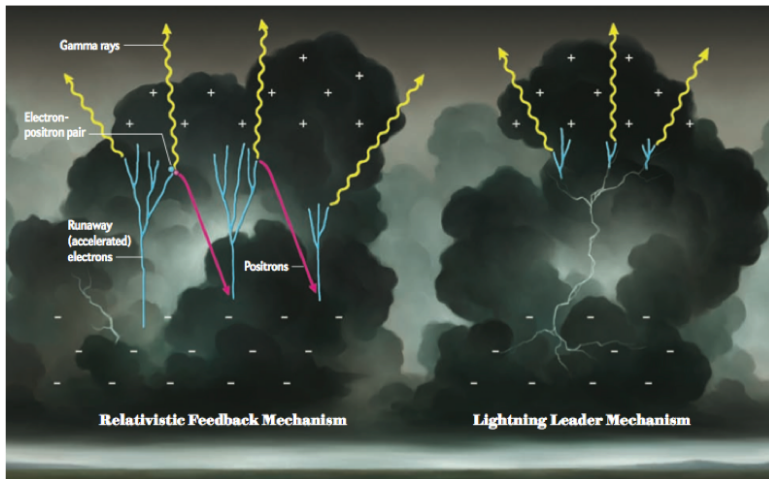
Figure 3.6: *A comparison of the relativistic feedback (left) and streamer-leader (right) models of TGF production. Taken from Dwyer and Smith (2012).*
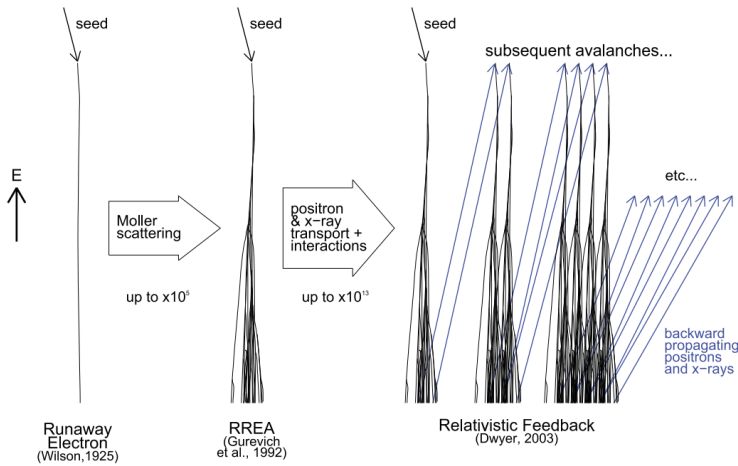
Figure 3.7: An illustration of the three mechanisms that generate relativistic electrons in the atmosphere, taken from Dwyer et al. (2012a). Møller scattering on a single runaway electrons produces a RREA, and positron and x-ray generate more RREAs with the relativistic feedback. Positrons and x-rays (blue arrows) are here shown bending to the right for clarity purpose only.

3.3.3 Thermal runaway

This theory is based on the assumption that the potential difference between a streamer head and the region ahead of it is sufficiently strong for the acceleration of thermal electrons (*Celestin and Pasko*, 2011; *Moss et al.*, 2006); that is, electrons without an initial kinetic energy over the ambient value, as required by the seeded models. This is the origin of the term "thermal", or "cold". In this scenario, the electric field at the streamer head is also responsible for the production and subsequent acceleration of the free electrons (*Celestin et al.*, 2012; *Köhn and Ebert*, 2015; *Moss et al.*, 2006). In this first step of the process, the cold electrons typically accelerate up to energies of the order of the keV. The voltage drop over the region where the electrons accelerate at the streamer tip may be insufficient for RREA (which requires a voltage drop of at least 7.3 MV), but after this first acceleration the electrons can act as seeds for a RREA.

In a second step of the process, the same mechanism is applied to the regions ahead of a lightning leader, where the electric field is weaker but spatially more extended. The same electrons that were already accelerated in the streamers region can be further multiplied and accelerated in this wider area (*Moss et al.*, 2006). It is also worth noticing that the electric field ahead of a leader must be over the conventional breakdown threshold for a new step to occur, which is close to the threshold for RREA initiation.

The multiplication happens through RREAs in this scenario too, but here the multiplication of RREAs via relativistic feedback is not necessary to justify the fluxes of TGFs (though not excluded either). Moreover, the electric field needs to go over the threshold in a limited region only, which is a less restrictive assumption. The energy gained by the electrons in this scenario depends on the configuration of the electric field, but if the latter is over the threshold for initiating RREAs, then the electrons can reach the MeV range.

Chapter 4

Meteorological Environment of TGFs

4.1   The connection between lightning discharge and TGFs

While it is established now that TGF are associated with lightning, the exact moment and process of production are still to be determined; the problem is further complicated by the fact that the leader process itself is still poorly understood. *Cummer et al.* (2005) showed that the time difference between TGF and closest lightning sferics implied that the TGFs were linked to the lightning stroke. They also showed that the charge moment change is orders of magnitude too low to generate at high altitude the electric field necessary for RREA, ruling out an association with sprites. They also observed that all associated lightnings had positive polarity, in accordance with the runaway breakdown theory that requires a downward electric field in order to have upward acceleration of electrons. *Williams et al.* (2006) and *Stanley et al.* (2006) were the first to point towards +IC lightnings, and further studies revealed that TGFs are most often produced by the upward IC negative leaders of such lightnings (e.g. *Cummer et al.* (2015); *Lu et al.* (2010); *Østgaard et al.* (2013); *Shao et al.* (2010)). *Cummer et al.* (2005) and *Stanley et al.* (2006) were able to define the simultaneity between RHESSI TGFs and radio sferics to a few milliseconds. *Connaughton et al.* (2010) narrowed it down to less than 50μs, thanks to the better time resolution of Fermi data. Subsequently, *Connaughton et al.* (2013) showed that the probability of association increases as the duration of the TGF decreases, which had already been explained in *Dwyer and Cummer* (2013) with the radio emission of the moving electrons responsible for the production of the TGF. The result has been confirmed for AGILE data in Paper II. *Cummer et al.* (2015) and *Pu et al.* (2019) showed that, for a subset of events, the TGF is simultaneous to a slow LF pulse in the waveform. This slow pulse has the same timescale of the lightcurve of the TGF and so it could be produced by the RREA, which means it could be the signature of the TGF itself. This hypothesis is supported by feedback models (*Dwyer and Cummer*, 2013) but more observations are needed to confirm it.

Shao et al. (2010) and *Lu et al.* (2010) found that the altitude of the leader associated with the TGF corresponded to the higher portion of the cloud: between 10.5 and 14.1 km in the first case, between 8.5 and 13 km in the second. *Cummer et al.* (2015) found that the moment of TGF production was midway in the leader development: that is, when the leader had reached a length of about 2 km, which takes 2 to 3 ms. This corresponds to an overall altitude of the leader tip of about 8 to 12 km, although the TGF may be produced at a lower altitude. Fast LF pulses indicate that the leader is stepping, but so far TGFs have not been linked to a specific one of these pulses. After producing the TGF, the leader keeps propagating for another ~2 km without significant changes in their characteristics except of their speed which, at least in the cases analysed, increased with altitude. Accelerating leaders have been reported (*Mar-*
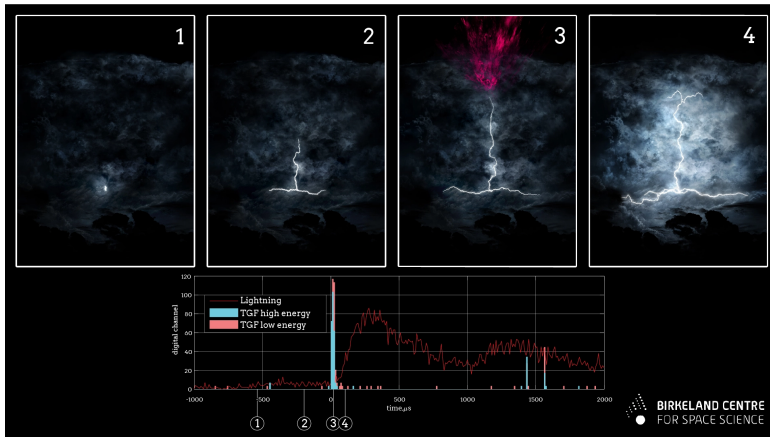
Figure 4.1: Artistic illustration of the production of a TGF during tan upward propagating leader. From the AGU press release of December 10th, 2019 (https: // news. agu. org/ press-release/ scientists-unveil-new-discoveries-about-gamma-ray-flashes-coming-from-thunderstorms/)

shall et al., 2013; *Wu et al.*, 2014), but it seems that they more commonly decelerate (*Behnke et al.*, 2005). The leaders were ordinary in all other ways, though relatively longer and faster than the average. These are possibly the only peculiar features of TGF-producing leaders and may suggest unusually intense ambient electric fields. It is not clear at the time of writing why TGFs are produced midway in the leader propagation, and not at a different moment. It is true, however, that the leader field in the early steps would not be strong enough and moreover an hypothetical TGF produced in the early stages of leader propagation would most likely be absorbed by the atmosphere and thus escape detection. *Østgaard et al.* (2019b) also supports the conclusion that TGFs are associated with leader propagation, using the unique combination of high-energy and optical detectors onboard ASIM. Their findings show that the TGF is produced immediately before the main optical pulse, which they interpret as an intense current pulse flowing into the leader channel. This is in contrast with the results of *Cummer et al.* (2015), where the leader kept propagating for longer after the TGF, but it might be an effect of the criteria used to select the events for the study.

TGFs have also been associated with Energetic In-cloud Pulses (EIP) (*Lyu et al.*, 2016). EIPs are a class of lightning events with a peak current greater than 200 kA (threshold set by the authors), as reported by NLDN (*Lyu et al.*, 2015). They have a slow timescale and occur in a different context, so they are distinguishable from Narrow Bipolar Events (NBE), with which they share the high current. These two classes of events represent the most energetic manifestation of IC discharge (see Section 2.2) but their underlying physics has not been understood yet. *Lyu et al.* (2016) showed that when positive EIPs were present in the field of view of Fermi, they were always the pulse associated with a TGF. Negative EIPs may produce downward TGFs (*Lyu et al.*, 2015), but at the time of writing we are not aware of any observations that would confirm it. While EIPs are always associated with TGFs, the opposite is not true, since TGFs are often associated to much less intense radio sferics and a large fraction is not associated to detectable sferics at all. It is then possible that the EIP is the radio signature of the TGF itself, but is only detectable (or recognised as EIP) under certain conditions.

4.2   Characteristics of TGF-producing storms

Several studies have investigated the characteristics of TGF-producing thunderstorms, in the hope that it would lead to an understanding of the more general conditions in which leaders capable of producing TGFs can develop. The results so far are not conclusive yet, but have evidenced some promising trends.

All studies agree that TGFs are mostly associated with tropical storms. This is likely a result of the fact that these storm reach higher altitudes thanks to both their stronger convection and the higher tropopause level in low latitude region. The stronger convection leads in turn to stronger electric fields, which are key to TGF production. A selection effect due to the orbit of the instruments used is not likely to have major influence as ASIM and RHESSI, which have the highest orbital inclination, found very few events at such high latitude (*Smith et al.* (2010, 2020), Paper III), despite spending most of the time there. One of the events in *Smith et al.* (2010) was linked to an unusual severe weather event, with extensive cold areas at the cloud top, but the study does not comment on the conditions of the other five. It can be said that TGF tend to occur in storms with high cloud tops (*Chronis et al.*, 2016; *Roberts et al.*, 2017; *Splitt et al.*, 2010; *Ursi et al.*, 2019), even though altitudes below 10 km were also reported. Moreover, *Ursi et al.* (2019) found that a third of the storms in their sample peak at a slightly higher temperature than the average range for storms in that latitude band, which implies a slightly lower cloud top altitude (see Section 4.4.2). *Chronis et al.* (2016) point out that the area associated with TGF production is high but not necessarily the single highest one of the cloud. Moreover, the cloud top may not be the altitude at which TGFs are produced: in fact, if they are associated with IC leaders, they are produced a few km below the cloud top. Interestingly, Paper III found out that, at least in the case of mid-latitude events, TGFs were produced near the main updraft (and overshooting top when present) but outside of it. Also interesting is the observation of *Roberts et al.* (2017) that when TGFs occur over cyclones, they happen in the outer rainband and never in the storm centre, as flash activity is much higher in the former than in the latter (*Cecil et al.*, 01 Apr. 2002). On the other hand, they reported that in multicell storm systems the central cells were just as likely to produce TGFs than the outer ones. An important point to be made in this regard is that a selection effect may be at play. Gamma photons interact with air molecules, mainly by Compton scattering, which means that their survival in the atmosphere is limited (*Williams et al.*, 2006). It may very well be that TGFs produced below a certain altitude (as well as many downward TGFs) are completely absorbed before they can reach a detector. This has important implications also for mid-latitude TGFs, as the tropopause altitude, and hence the maximum cloud top altitude, decreases with latitude, making photons generated by higher latitude storms cross a thicker layer of air (*Smith et al.*, 2010); this is the focus of Paper III. *Smith et al.* (2016), however, argues against the existence of a population of TGFs that are produced at low altitude and invisible from space. The main point is that, given the atmospheric absorption profile, unless these events all happen to be very weak some of them would still be bright enough to be detected from space and would create a bright summed signal that has so far not been observed. They would also be observed by aircraft detection campaigns like ADELE (*Smith et al.*, 2011) and ALOFT (*Østgaard et al.*, 2019c), which have observed gamma ray glows. Finally, positive EIP are also located in the same range of altitudes as TGFs and not below, so if TGFs and EIPs are manifestations of the same event, a low-altitude population seems unlikely (*Lyu et al.*, 2015). Interestingly, negative EIPs are much rarer than positive ones, implying that downward TGFs (which would also escape detection from orbit) are rarer than the upward ones.

A relationship with flash rate is also established. TGF-producing storms have unusually high

overall flash rate (*Fabró et al.*, 2015), but at the same time TGFs seem to happen after a period when the interflash rate is longer than the average for the storm (*Larkey et al.*, 2019), which could indicate a longer charging time for the electric field (*Chronis et al.*, 2015; *Hutchins et al.*, 2013). A high flash rate may simply be increasing the chances of a leader happening in the right conditions, but the longer charging times are in accordance with the feedback mechanism production (*Dwyer et al.*, 2008), which requires a high threshold for the electric field. The flash rate is also an indication of the development stage of the thunderstorm, but in this regard results are inconclusive: *Roberts et al.* (2017) and *Ursi et al.* (2019) found TGFs more likely to occur during the growth phase of the storm, while *Smith et al.* (2010) found they usually come after the peak of lightning activity and Paper III had examples of both cases. It is also worth pointing out that the samples in *Ursi et al.* (2019) and *Roberts et al.* (2017) may be biased because TGFs were selected on the basis of WWLLN association, while the sample of Paper III was selected by latitude, therefore avoiding this bias.

From the point of view of convective strength, the picture is less clear. The same studies, as well as Paper III, report a wide range of conditions, from extensive mesoscale convective systems to scattered, weak convection. *Roberts et al.* (2017) even report an event originating from the remains of a dissipating storm. It is also worth noting that mesoscale convective systems can have a higher chance of producing TGFs just because of their wide extension and long lifetime, without necessarily involving other characteristics.

Finally, TGFs follow the same seasonal pattern as thunderstorms (*Fabró et al.*, 2015; *Maiorana et al.*, 2020), implying that the conditions that lead to TGF production are not dependent on the season, beside the simple thunderstorm occurrence rate. The same is true for the diurnal cycle (*Splitt et al.*, 2010): TGFs follow the flash activity, which peaks in the late afternoon and has a minimum at the local midday.

4.3   Geographic Distribution of TGFs

Storm and lightning activity is not uniform around the globe, but tends to concentrate in certain spots, determined by atmospheric currents and terrain features. Three major lightning hotspots have been identified in Central America, Central Africa and the archipelagos of South-eastern Asia (*Christian et al.*, 2003); in the following, the name "lightning hotspots" will refer to these three regions. The Congo basin in particular has the absolute global maximum of flash activity. Other high-intensity regions are the central plains of the US and the southern Himalaya. In general, lightning is more frequent over coastal areas and mountain ranges, as well as convergence zones like the Intertropical Convergence Zone (ITCZ) and areas where synoptic scale cyclones occur. Conversely, there is very little lightning activity over open oceans, although aerosols over important maritime trade routes or adjacent to desert areas have been shown to enhance flash activity (*Thornton et al.*, 2017). Figure 4.2, taken from *Christian et al.* (2003), shows the annualized map of lighting activity around the globe.

TGFs, however, do not occur with the same frequency in all regions. On a global level, TGFs seem to prefer coastal regions (including the shores of big lakes) over mainland and open ocean, occurring in even higher rate than the (high nonetheless) flash activity would imply. This has been verified for all missions: see *Albrechtsen et al.* (2019); *Splitt et al.* (2010) for RHESSI, *Roberts et al.* (2017) for Fermi and Paper II (*Lindanger et al.*, 2020) for AGILE. *Smith et al.* (2010) and *Briggs et al.* (2013), as well as Paper III of this project, present TGF-to-lightning ratios for the three main hotspots and show that the value for Central Africa is significantly lower that the other two, which are both coastal areas with an abundance of islands, although it is not clear if this factor is sufficient to explain the discrepancy. *Fabró et al.*
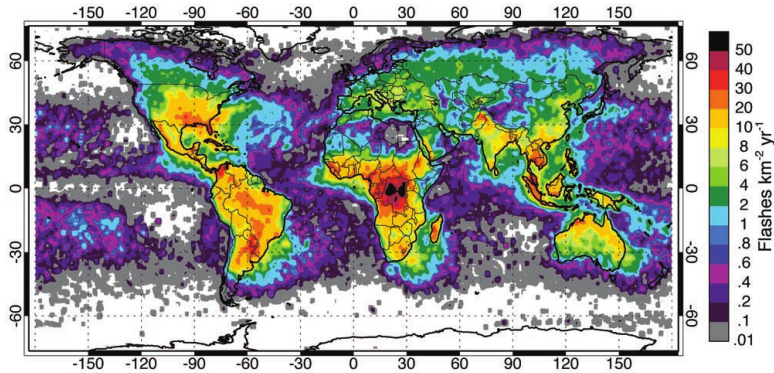
Figure 4.2: The annualized distribution of total lightning activity. From Christian et al. (2003).

(2019) proposed that the particular conditions in which African storms develop leads to intense but less structured electric fields, which in turn means a high rate of less energetic flashes, not fulfilling the conditions required for TGFs production. Paper III also shows the particularly interesting case of the Himalayan region, where the flash rate is one of the highest of the globe and still no TGFs were ever detected. Conversely, *Fabró et al.* (2015) identified a region of TGF production over the Pacific which, though less active, still shows a significant peak over the rest of the Ocean.

At temperate latitudes (35° to 52°), four more TGF-producing regions have been identified (Paper III): the Mediterranean Sea, the north-western Atlantic, the eastern South African Sea, and north-eastern China. The former two are also reported in *Smith et al.* (2010) and *Gjesteland et al.* (2015). They are most likely the result of local weather patterns and climatic conditions, but due to the very small number of events detected, they cannot be considered "TGF hotspots".

4.4 Meteorological data used in this study

4.4.1 Lightning Detection

Being TGFs associated with lightning, lightning data are the most relevant ones. They provide insight into the production process, constraints for theoretical models and also an accurate location for the event.

Lightning detection networks consist of an array of sensors operating in different bands of radio frequency, depending on what one needs to observe as different lightning processes emit in different wavelengths. The most commonly used bands are 60-200 MHz for stepping leaders, 1-400 kHz for return strokes and 4-1000 Hz for continuing currents (*Füllekrug* (2017) and references therein). Figure 4.3 illustrates the different types of detectors and their ranges. The detectors are often arranged into networks, so that they can triangulate the position of the lightning stroke, using either magnetic direction finding (MDF) or time-of-arrival (TOA) methods. MDF is based on the measurement of the magnetic field and the perturbations caused by the traveling electromagnetic wave. This method can have significant errors induced by local geology, so TOA or a combination on the two is nowadays preferred. TOA is applied to electric field measurement and is based on the time difference between recordings of the same signal
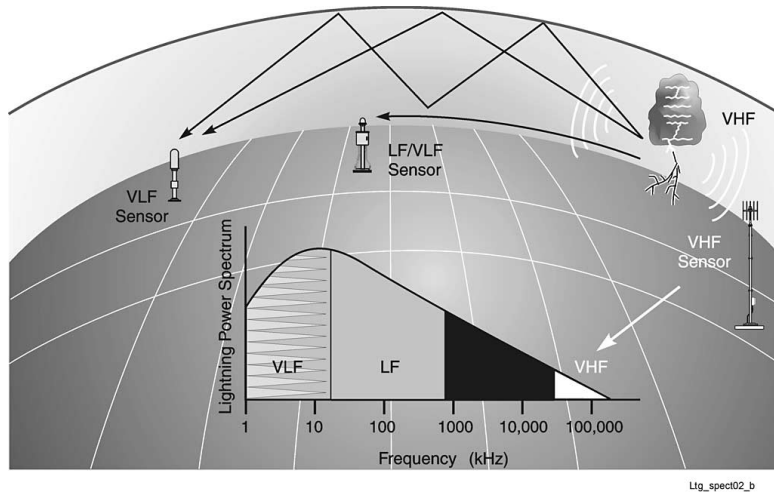
Ltg_spect02_b

Figure 4.3: Illustration of different receivers for lightning location, from Cummins and Murphy (2009).

by three or more receivers: a constant time difference between two detectors defines a hyperbola, and the intersection of at least three such curves is the location of the stroke (*Cummins and Murphy*, 2009). Occasionally, the location provided is ambiguous, but a fourth detector involved will solve the ambiguity. The detection efficiency of these systems, though greatly improved by modern GPS clocks, is then dependant on the number of sensors within range. *Hutchins et al.* (2012) estimates for WWLLN a corrected global absolute detection efficiency of around 13%, but finds wide areas over which it rises well above 80%. The single waveforms recorded by each detector can also be analysed, as each step of the lightning process has distinctive radio signatures and the overall waveform of CG and IC lightning are different.

Three networks provide global coverage: the World Wide Lightning Location Network (WWLLN), the Earth Networks Total Lightning Network (ENTLN) and the Global Lightning Dataset (GLD360). All three have been used for this project, WWLLN above all. WWLLN is based on over 70 VLF receivers placed around the world and is able to provide real time monitoring of lightning activity. Localization of the strokes is made with time-of-group-arrival (TOGA) methods, which uses the time of arrival of the wave packets, rather than the simple trigger time, to obtain more uniform arrival times across the network (*Hutchins et al.*, 2012). Like most networks, WWLLN preferentially detects lightnings with relatively high peak current, which often means CG. This is a downside of using VLF sensors, since leader activity mostly emits at shorter wavelengths and these shorter wavelengths also suffer more absorption and scattering in the atmosphere. However, since VLF can travel across the globe, it is the only way to provide global coverage with a ground-based system.

An additional way of detecting lightning is by use of space-borne instrumentation. At the time of writing, the only mission entirely dedicated to lightning detection from space is the Lightning Imaging Sensor on the International Space Station (ISS-LIS, *Blakeslee et al.* (2020)), which carries a spare version of the LIS instrument flown on the Tropical Rainfall Measuring Mission (TRMM) operative between 1997 and 2015. The Geostationary Operational Environmental Satellite-R (GOES-R) series of weather satellites carry the Geostationary Lightning Mapper (GLM) onboard among other instruments. The Optical Transient Detector (OTD, *Boccippio et al.* (2000)) and the TRMM-LIS were operating in the past and provided the first global climatology of lightning, and high quality observations for many decades. These instru-

ments detect the optical (an oxygen line with 777.4 nm wavelength) emission from lightning channel as they orbit above the storm; for this reason, they cannot monitor the evolution of a given storm over time, with the exception of instruments like the GLM onboard GOES-R, which is geostationary. They also cannot distinguish between IC and CG lightning, but their overall detection efficiency is very high. The MMIA instrument in ASIM is also an efficient lightning detector, particularly for the optical cameras and the 777.4 nm photometer. The main purpose of the build was to capture both a TGF or TLE and the parent stroke, but MMIA does detect flashes independently, and they can in principle be used for lightning mapping. Paper III of this project used the global lightning maps provided by LIS/OTD (*Albrecht et al.*, 2016) in order to calculate the TGF-to-lightning ratio (TLR) over various regions, a fundamental parameter in TGF science. MMIA data were used to help identify the parent stroke, when possible. Strokes detected by ground-based networks, on the other hand, have been used across all papers to match TGFs with a possible associated lightning and a location. Paper II in particular is entirely concerned with matching of TGFs to WWLLN strokes.

4.4.2   Meteorological Satellites Images

Information about the atmospheric conditions around the TGFs can be obtained by geostationary weather satellites. Infrared images in particular track the evolution of a storm and allow an estimate of the intensity of the convection and the overall severity of the storm. The Cloud Top Temperature (CTT) is measured in the thermal infrared (IR) band (e.g. ~$10 - 12\mu m$) and represents the effective blackbody temperature of the cloud. As the atmospheric temperature decreases with increasing altitude in the troposphere, it can be converted into an actual altitude by comparing it to a local atmospheric sounding (*Smith and Platt*, 1978). This has been shown to have intrinsic biases, albeit small (*Sherwood et al.*, 2004), and besides a local and recent atmospheric sounding is not always available. It is therefore common to use the CTT as a proxy for altitude, without explicit conversion. A thunderstorm's vertical development depends on both its stage of evolution and the intensity of the convection. A higher cloud top altitude (a lower CTT) indicates a more mature stage and a stronger convection. IR images also allow the identification of overshooting tops, dome-like structures that form when the updraft is so intense that it pushes into the stratosphere. Figure 4.4, taken from the supplementary materials to Paper III, is an example of a storm imaged in the IR. The image was obtained from the Himawari satellite. The white colour indicates the area with lowest temperature, which corresponds to the updraft and is likely to be an overshooting top. Lightning activity (the circles and pluses) is normally most intense around the border of the updraft.

Weather satellites produce an IR image every few minutes: 10 minutes for GOES, 15 minutes for Meteosat and 20 minutes for Himawari, the three satellites used for the study in Paper III. It is therefore possible to track the evolution of a storm in both vertical and horizontal extension and reconstruct the more general environment that lead to the production of a TGF.
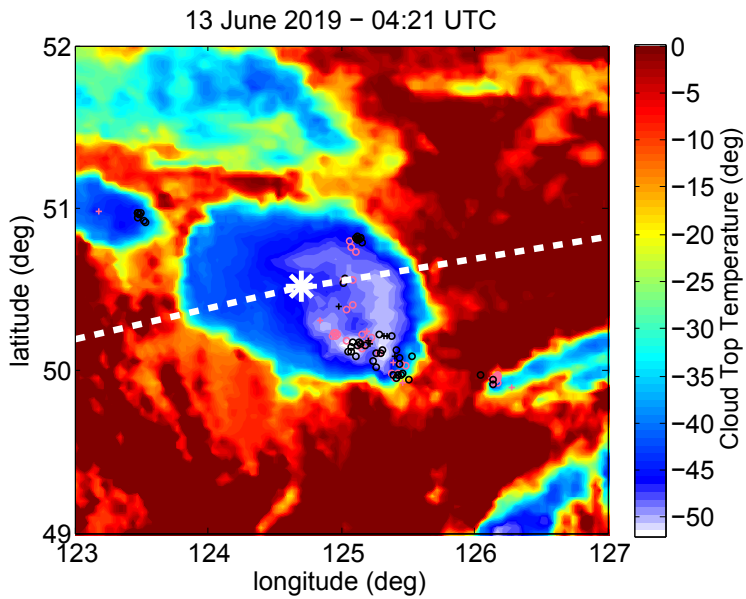
Figure 4.4: An example of convective storm seen in the IR band. The circles and the pluses are the -CG and +CG strokes, respectively, detected within 5 minutes around an ASIM TGF (the pink before and the black after). The white star and dotted line indicate ASIM's position and trajectory.

Chapter 5

Results

5.1 Summary of Papers

5.1.1 Paper I: The 3rd AGILE Terrestrial Gamma-ray Flashes Catalog. Part II: Optimized selection criteria and characteristics of the new sample

Paper I presents the third TGF catalogue for the AGILE mission. After the inhibition of the anti-coincidence shield for MCAL (see Section 3.1.1), *Marisaldi et al.* (2015) found out by comparison with WWLLN sferics that about a half of TGFs were not detected by MCAL, this time due to excessively strict selection criteria. The goal of Paper I was then to analyse a set of TGFs identified merely by WWLLN association and use them as a reference to develop new, more sensitive selection criteria.

The reference sample consists of clusters of at least 6 counts that were identified as TGFs only by their simultaneous association to WWLLN sferics, according to *Connaughton et al.* (2013). The purpose of the work was to explore different variations of the selection criteria in search for the combination that provided the highest number of hits while keeping the sample as clean as possible. Each set of criteria was tested on the reference sample. Two of the old requirements proved to be very effective despite their simplicity, and were therefore left unchanged: having at least 10 counts in total and having at least one count in each of the quadrants in which the detector was ideally divided (because at satellite altitude TGFs are wide enough to be approximated with a plane wave and are therefore expected to hit the detector rather uniformly). The requirement on hardness ratio (the ratio between particles of energy above and below 1.4 MeV) was turned into a minimum value of 0.5 MeV for the median energy, which was found to be less sensitive to statistic fluctuations. Finally, a requirement on maximum energy had been placed to reject cosmic rays, but its effectiveness was found to depend on the flux of the TGF and subsequently implemented as follows: for high flux events (count rate above 30 kHz), energies up to 120 MeV are allowed, otherwise the limit is at 30 MeV. The former options allows for the recovery of events distorted by the effect mentioned in Section 3.2, while the second options rejects cosmic particles. These criteria brought up the number of TGFs from the 279 of the second AGILE catalogue to 2780, while keeping the possible spurious events at a minimum. This catalogue is the largest to date over the equatorial region and is openly accessible at this link: http://www.ssdc.asi.it/mcal3tgfcat.

The sample was also analysed concerning the characteristics of the TGFs themselves and their geographical and seasonal variation. Concerning the season in particular, it was evidenced

how some regions, like Central Africa and Borneo, have constant year-round production of TGFs, while other have varying activity because of local weather patterns. A general drift with the ITCZ was also observed across the year. Our analysis of median energy, duration and intensity does not evidence any seasonal trends, so it does not support the possibility that the characteristics of TGFs depend on factors such as the type of storm or the surrounding atmospheric condition, at least over the equator. Since the reference sample was selected over one spring and one summer, this also excluded the presence of biases, at least concerning energy, intensity and flux. A possible bias comes from the duration, as short TGFs are more likely to have a sferics association (see Section 4.1); for this reason the duration does not explicitly appear in the selection criteria.

5.1.2   Paper II: The 3rd AGILE Terrestrial Gamma Ray Flash Catalog. Part I: Association to Lightning Sferics

Paper II is a companion for Paper I. It details the procedure followed to search for TGFs in the AGILE data by virtue of their association with a WWLLN lightning sferic, throughout two different periods of AGILE activity. The TGFs identified this way during the so-called reference period were the ones used as a starting point for Paper I; the others provided one of tools for validating and assessing the quality of the new selection criteria. For this reason, Paper II is actually the first paper of the set, even if it is presented here as second, merely for authorship reasons.

The TGFs in this paper's sample show on average shorter durations than the TGFs found by selection criteria in Paper I. This is most likely an effect of the association probability described in *Connaughton et al.* (2013), which also justifies the choice of not using the duration as a selection criterion. The geographical distribution of the sample follows the global lightning distribution and is consistent with the samples reported by RHESSI and Fermi. A preference for coastal regions is also visible, as was the case for the RHESSI sample. An estimate of the probability of producing TGFs over coast, land and ocean derived by the data show that TGFs-to-lightning rate is not constant for the three regions, but the production of TGFs must be enhanced over the coastline.

The association of TGFs with WWLLN sferics was also used to diagnose a failure in AGILE's internal GPS and correct the onboard clock accordingly. The correction method developed in this paper is routinely used every few months to check the temporal accuracy of AGILE. The WWLLN-identified events are also available online at the aforementioned url: `www.ssdc.asi.it/mcal3tgfcat`.

5.1.3   Paper III: Observation of TGFs at Mid Latitude

Paper III reports and analyses the first TGFs ever detected over temperate regions, expanding the observable limit from the 38°of RHESSI to 52° thanks to ASIM (57° if taking into account the extension of the field of view of MXGS). The sample consists of only 14 events, out of more than 700 total. The goal of the study is twofold: to analyse the thunderstorm that produced those TGFs, in search of any characteristics that may be different from what observed at lower latitudes and give insight into the meteorological conditions most favourable to TGF production; and to asses whether the atmospheric absorption due to a lower tropopause height is enough to justify the rarity of TGFs at mid latitudes, as suggested by *Williams et al.* (2006). Of all the characteristics of the mid-latitude sample, the duration was the only one showing

statistically significant differences from the general sample. Mid-latitude TGFs appear to be slightly shorter than tropical ones, but our analysis did not provide any possible explanation.

Concerning the thunderstorm environment, we found that our sample was produced over a wide variety of conditions ranging from relatively weak to intense convection, in accordance with other results. In almost all cases, however, and differently from the previous studies, the storms were isolated, compact and relatively small. There seemed to be no preference for the growing or the decaying phase of the storm, although the size of the sample (14 events) is not statistically significant.

The peak current and radio waveform of the candidate associated strokes were also analysed. All sferics except one were compatible with +IC strokes, in accordance with modeling and previous observations. Four events were associated with pulses of current high enough to be possibly classified as EIP; the remaining had currents of a few tens of kA, which is more than the estimated average for IC (a few kA).

Finally, we evaluated whether the atmospheric absorption rate at mid latitude was sufficient to explain the number of TGFs that we detected, taking into account the global lightning pattern and the amount of time ASIM spends in each latitude band (the exposure). We applied to the equatorial sample the same absorption that would be experienced at mid-latitude (as obtained from atmospheric reanalysis) and found out that the number of events that remain above trigger threshold is compatible with the number of detected events. The higher atmospheric absorption then seems to be the major factor contributing to the rarity of TGFs at mid latitude, but our results do not exclude the presence of others, such as the ratio between IC and CG lightning. On a more general level, the analysis of the TRL confirms the findings of the previous missions: while on average the TGF production rate scales with lightning activity, the TLR depends on local meteorological and geographic features. Coastal areas, for example, are very prone to lightning activity (see Section 4.3), but the amount of TGFs produced there is proportionally higher. The same does not apply to other high-activity regions, like mountain ranges. Considering the equatorial hotspots, the TLR of South-east Asia and Central America is higher than the one for Central Africa, even if the Congo Basin is the area with the absolute highest flash activity; it is also, though, a mainland region. The same behaviour is manifested in the mid-latitude sample: of four TGF-producing regions, one is coastal (Mediterranean Sea), one is oceanic (South African Sea) and one is mixed (North-eastern America, which includes a coastal area over the Great Lakes and an oceanic area over the Atlantic). Only one, North-east China and Siberia, is purely inland. Moreover, the fact itself that the fourteen TGFs of the sample all came from four, limited areas mean that the particular conditions of those areas allow for a high enough TGF production rate to overcome the effect of the greater atmospheric absorption.

These results extend to the mid-latitudes, a region previously unexplored, an already-known property of TGFs: that the intensity of the electric field matters the most, but since the production of the TGF happens in a limited area, only small parts of the field need to be over the RREA threshold. Which, in turn, mean that TGFs can in principle be produced by any thunderstorm.

Chapter 6

Conclusions and Future Prospects

6.1 Conclusions

The goal of this project has been to investigate the connection between TGFs and thunderstorms, which is a fundamental piece to understand the conditions that can lead to TGF production. Some phenomena, like sprites, have been seen to be more common during certain types of thunderstorm, since they are related to a relatively rare type of lightning discharge (the +CG). The research done so far indicates that TGFs instead are linked to +IC, which are the most common lightning type, occurring with convection of any severity. This, however, does not imply that TGFs occur uniformly around the globe, as it is clear from the results of all papers.

Papers I and II present the third catalogue of AGILE TGFs which, at the time of writing, is the most extensive one available for the equatorial latitude band. The catalogue is freely available at `www.ssdc.asi.it/mcal3tgfcat`. A first analysis of the sample shows that the TGFs fall in line with what already reported by other missions in terms of duration, association with lightning sferics, geographic distribution and seasonal and local time trends. A direct comparison with the Fermi sample also shows comparable detection rate for the areas covered by both spacecrafts. Moreover, the time correction derived from WWLLN association was crucial in the recovery of events during the period of the GPS failure, and a constant corrective offset derived from the correlation is still currently in use.

Paper III expands the work of *Smith et al.* (2010) and is the first ever reported sample of TGFs detected at mid-latitudes, including the first detections over $\pm 38°$ of latitude. The duration is the only characteristics that differs from the low-latitude population. All others are comparable and the same is true for the associated thunderstorms. We also presented the first estimate of TLR for the mid-latitude regions, showing that it is compatible with the equatorial value combined with the higher atmospheric absorption, while leaving room for other factors as well. Atmospheric absorption was in fact confirmed to be the main contributor to the rarity of TGFs at mid- and high- latitudes, as foreseen by *Williams et al.* (2006) and *Smith et al.* (2010).

6.2 Future Prospects

The research for this project followed two main directions, reflected in the papers: event identification (catalogue) and analysis of the associated meteorological characteristics. Both aspects are opening paths to future development: extensive catalogues are fundamental for statistical analysis and cross-correlation with other data, from both ground and space. The analysis

of meteorological conditions, on the other hand, gives a direct insight into the physics of the TGFs and is currently a very active research topic.

Papers I and II provide and extensive catalogue of events which is yet to be fully exploited. Being confined to a narrow latitude band, the sample allows a much better detail than other catalogs where events are spread over a large geographical area. This is particularly important for an exploration of geographical and seasonal characteristics, which have been only touched upon in our papers, as for example: local variation of the TLR with season (never explored before) and detailed investigation of the TLR over land, ocean and coastal regions. Moreover, the high number of events will allow for any study relying on statistics. The process we followed to fine tune the selection criteria can be adapted for other missions too, since having reliable selection of TGFs is fundamental when the instrument itself was designed for something else. Furthermore, a detailed catalog is also the basis for planning and designing new ground-based or airborne experiments, which can provide information from a different, and so far less explored, point of view. The same can be said for the algorithms for finding associations with WWLLN: an extension to a higher sensitivity network, such as GLD 360, could further improve the number of events with a reliable location.

Paper III is just the first analysis of non-tropical TGFs. RHESSI, the only other mission covering mid-latitude, was decommissioned in 2018, while ASIM is expected to continue activity at least until the end of 2021. The sample of mid-latitude events may therefore be expanded, and a more statistically significant sample may evidence trends that are not visible in ours. Already we had seen that mid-latitude TGFs seem to cluster at shorter durations compared to the general population, but only a bigger sample will confirm it. Similarly, the thunderstorms we analysed did not show any peculiar characteristics, in line with previous studies, but it is still possible that some distinctive features may emerge thanks to the different atmospheric conditions of the temperate regions. Finally, we did not rule out the possibility of factors other than absorption influencing the detection rate of TGFs, as for example the local IC/CG ratio. A forthcoming study should address this factor, especially in relation to mid-latitude regions with high lightning activity but no sign of TGFs, such as the Himalaya and the Great Plains. Finally, our method for calculating the average and peak TLR can be used on the general sample from ASIM and of other missions, and to study variations of the ratio not only in space but also in time.

Chapter 7

Scientific results

Paper I

The 3rd AGILE Terrestrial Gamma-ray Flashes Catalog. Part II: Optimized Selection Criteria and Characteristics of the New Sample

C. Maiorana, M. Marisaldi, A. Lindanger, N. Østgaard, A. Ursi, D. Sarria, M.Galli, C. Labanti, M. Tavani, C. Pittori and F. Verrecchia

Key Points:
- A new set of selection criteria for AGILE TGFs is designed based on a lightning-associated TGF sample
- A sample of 2,780 events detected by AGILE over a 3-year period is presented, the largest sample to date across the equator
- Geographical, local time, and seasonal variability of the sample is discussed

Correspondence to:
C. Maiorana,
Carolina.Maiorana@uib.no

The 3rd AGILE Terrestrial Gamma-ray Flashes Catalog. Part II: Optimized Selection Criteria and Characteristics of the New Sample

C. Maiorana[1], M. Marisaldi[1,2], A. Lindanger[1], N. Østgaard[1], A. Ursi[3], D. Sarria[1], M. Galli[4], C. Labanti[2], M. Tavani[3], C. Pittori[5,6], and F. Verrecchia[5,6]

[1]Birkeland Centre for Space Science, Department of Physics and Technology, University of Bergen, Bergen, Norway, [2]INAF-OAS Bologna, Via Gobetti 101, I-40129 Bologna, Italy, [3]INAF-IAPS Roma, Rome, Italy, [4]ENEA, via Martiri di Monte Sole 4, I-40129 Bologna, Italy, [5]Space Science Data Center - Agenzia Spaziale Italiana, Via del Politecnico, s.n.c., I-00133, Roma, Italy, [6]INAF - Osservatorio Astronomico di Roma, Monte Porzio Catone, Italy

Abstract We present in this work the third catalog of terrestrial gamma-ray flashes (TGFs) by the AGILE mission and the new search algorithm that was developed to produce it. We firstly introduce the new selection criteria, designed from the characteristics of WWLLN-identified TGFs, and then applied on all data from March 2015 to September 2018. Association with sferics was performed by an independent search, described in a companion paper by Lindanger et al. (2020, https://doi.org/10.1029/2019JD031985). This search showed that many TGFs were not recognized by the existing selection algorithm, hence the need for this work. Several new selection criteria were tested and compared in this paper. We then present the chosen selection criteria and the obtained sample, which includes 2,780 events and represents the most extensive TGF catalog available for the equatorial regions. Finally, we discuss the characteristics of this sample, including geographic distribution, intensity and duration, and seasonal variations.

1. Introduction

Terrestrial gamma-ray flashes (TGFs) are bursts of gamma photons produced inside thunderstorms and associated to lightning. They typically last for less than 1 ms, have energies up to a few tens of megaelectron volt, and are bright enough to be detected by particle detectors on spacecrafts. They were first recorded by the Burst and Transient Source Experiment (BATSE) instrument onboard the Compton Gamma Ray Observatory (CGRO) mission (Fishman et al., 1994), then by the Reuven Ramaty High Energy Solar Spectroscopic Imager (RHESSI) (Smith et al., 2005). They are now regularly observed by Fermi (Briggs et al., 2013), the Astro-rivelatore Gamma a Immagini Leggero (AGILE) (Marisaldi et al., 2010), and the Atmosphere-Space Interactions Monitor (ASIM) (Neubert et al., 2019), which MXGS instrument is specifically designed for the detection of TGFs. Many thousands of TGFs have been detected over the course of the years and catalogs have become an important tool available to the scientific community for general purposes: for population studies and to correlate TGF observations with other data, mainly ground-based lightning detection networks. Several TGF catalogs have been published so far: by RHESSI (Grefenstette et al., 2009), further improved in the work by Gjesteland et al. (2012); by Fermi (Roberts et al., 2018); and by AGILE (Marisaldi et al., 2014, 2015). Each of these missions are observing a slightly different population, due to the intrinsic differences in the detectors and orbits.

The AGILE mission is run by the Italian Space Agency (ASI) and is devoted to high-energy astrophysics (Tavani et al., 2009); it combines gamma- and hard X-ray imaging, for the simultaneous detection of photons in several energy bands. The primary goal of the mission is the study of the gamma-ray sky, but it was soon clear that also TGFs were detected by the Minicalorimeter (MCAL) instrument (Marisaldi et al., 2010). However, the dead time introduced by the anti-coincidence shield prevented the detection of events shorter than about 100μs, thus biasing the sample towards longer duration. Moreover, since the probability of association with the lightning sferic is inversely proportional to the duration of the TGF (Connaughton et al., 2013; Dwyer & Cummer, 2013) and is low for TGFs lasting more than about 150μs, no simultaneous association with lightning sferics were obtained. In March 2015, the anticoincidence shield was switched off for MCAL and the detection rate increased by almost one order of magnitude (Marisaldi et al., 2015).

The subsequent comparison with data from the World Wide Lightning Location Network (WWLLN) allowed the selection of a sample of TGFs simultaneously associated to lightning sferics, of which about half were not recognized by the offline selection, performed on ground. It was then clear that AGILE could benefit from a redesign of the TGF selection criteria and that this would lead to a substantial increase in the TGF detection rate. Here, we consider the AGILE 1st TGF catalog as the sample of 308 TGFs detected by MCAL between March 2009 and July 2012, prior to the inhibition of the anticoincidence shield, and published in Marisaldi et al. (2014) (available at https://www.ssdc.asi.it/mcaltgfcat/). We consider the AGILE 2nd catalog as the sample of 279 TGFs detected by MCAL between March and June 2015, following the inhibition of the anticoincidence shield, and published in Marisaldi et al. (2015) (available at https://www.ssdc.asi.it/mcaletgfcat/). The data set presented here include 2,780 events detected during the period between March 2015 and September 2018 and will be hereafter considered the 3rd AGILE TGF catalog.

We describe the data sets from AGILE in section 2. We then explain the method we have followed to design the new criteria in sections 3 and 4, a description of the old and new selection criteria and a description of the validation methods. In section 5, we present the obtained, new sample and we discuss the characteristics of said sample in terms of geographic and seasonal properties, compliance with theory and with other missions, limitations and improvements with respect to the older catalogs. An independent analysis of TGFs associated to lightning sferics detected by WWLLN is presented in the companion paper by Lindanger et al. (2020), hereafter referred to as L20.

2. Instruments and Data Sets

The AGILE payload includes several instruments, of which the MCAL is the main detector for TGFs. It is made of 30 scintillator bars arranged in two superimposed planes, with orthogonal orientation of the bars; see Labanti et al. (2009) for a detailed instrument description and (Tavani et al., 2009) for a complete description of the AGILE payload. Data collection takes place when a trigger is issued by the onboard trigger logic. The onboard trigger logic works on several timescales, from 293μs to 8 s. The most relevant timescale for TGF science is the shortest one, 293μs, for which a constant threshold of eight counts is set. Following each trigger, between about 6 and 10 s of data (depending on configuration setting) around the trigger time are then saved and downlinked. Since the trigger will include cosmic rays, statistical fluctuations and legitimate events (TGFs or cosmic Gamma-Ray Burst, GRB), those files are analyzed on ground to distinguish between the cases and identify TGF candidates.

One of the most relevant parameters to describe the sensitivity of an instrument is its effective area. This parameter depends both on photon energy and incoming direction; therefore, the total effective area depends on the spectrum of the source and the viewing angle. TGFs are known to exhibit spectral diversity (Mailyan et al., 2016). Moreover, the same source spectrum will result in different observed spectra at satellite altitude, depending on production altitude and distance between the source and the subsatellite point, because of photon propagation through the atmosphere. To assess the MCAL average total effective area for TGFs, we proceeded as follows. A TGF source spectrum consistent with a fully developed relativistic runaway electron avalanche (RREA) process is simulated. Photons are produced at 15-km altitude with angular distribution uniform on a cone with vertical axis and a half-cone angle of 40°. We chose a 15-km altitude because it is an adequate value for cloud top altitude in equatorial thunderstorms, as well as a value compatible with the analysis reported in Dwyer and Smith (2005) and Hazelton et al. (2009), although lower altitudes have been reported for the lightning leaders involved in TGF production (Cummer et al., 2015) and from radar observations associated to TGFs (Chronis et al., 2016). A 40° half opening angle at source is a value compatible with a large set of independent analysis (Carlson et al., 2007; Gjesteland et al., 2012; Hazelton et al., 2009). Photons are then propagated through the atmosphere, parameterized by the NRLMSISE model (Picone et al., 2002), up to satellite altitude by means of the GEANT4 toolkit (Agostinelli, 2003). Spectra for different distances between source and subsatellite point in the range between zero and 800 km have been simulated. These spectra were then used as input for the MCAL mass-model for different angles between the incoming photons direction and the normal to the detector plane. We call this angle θ. A large number of photons randomly extracted from the source spectrum was simulated. The total number of counts detected in MCAL was then divided by the number of incoming photons passing through the detector, and then multiplied by the detector geometrical area for the corresponding viewing angle. The obtained results are summarized in Figure 1, which shows the MCAL total effective area for a typical TGF as a function of the distance
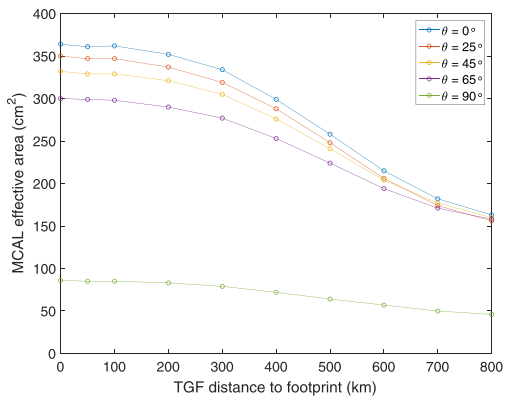
Figure 1. Total MCAL effective area for a typical TGF spectrum produced at 15-km altitude, as a function of the offset distance to the subsatellite point and the angle between the satellite pointing and the source location.

to the subsatellite point and the θ angle. This is equivalent to the convolution of a spectral model with a fluence of 1 ph/cm^2 with the appropriate detector response matrix, as done in the First Fermi TGF catalog (Roberts et al., 2018); see figure 4 therein. For practical purposes, Figure 1 allows to estimate the TGF fluence at satellite altitude, given the observed number of counts and the source distance to satellite footprint provided by an associated lightning sferics. A plot of the monoenergetic effective area can be found in Labanti et al. (2009) and Marisaldi et al. (2010). We only considered the θ angle because the MCAL response is only weakly dependent on the azimuth angle orthogonal to θ. We do not consider θ angles larger than 90° because then the photon flux interacts with the satellite structure, which is not accurately modeled, before entering the detector; therefore, the results are less reliable. We note also that in these computations, we did not consider the TGF flux, which may significantly deplete the effective area for very short and bright events, due to instrumental effects described in Marisaldi et al. (2019).

The general data set is divided into four data sets, summarized in Table 1, based on absolute timing accuracy and effectiveness of the anticoincidence shield (AC). More detailed information on those periods is in Lindanger et al. (2020). AC-ON refers to the first years of AGILE operations, with the onboard software configuration optimized for the detection of GRBs. We did not consider it for this work, as the presence of the anticoincidence shield poses some biases in the characteristics of the detected TGFs, which disrupt the homogeneity of the sample. Moreover, in this period, the TGF detection rate was about one tenth of that of the following periods and there are no WWLLN-associated events. The properties of the TGF sample collected in this period are described in (Marisaldi et al., 2014). A search for WWLLN associations in this period was carried out and discussed in L20. The reference (REF) period covers three months with optimal absolute timing accuracy after the inhibition of the AC for MCAL. The REF period presented here includes more data than the same period in Marisaldi et al. (2015), because we extended the REF period by two additional weeks for this study. The DRIFT period covers the span between July 2015 and December 2018. It is characterized by a failure in AGILE's internal clock, which caused a total loss of data for a few weeks at the beginning of the period, and a timing uncertainty on subsequent data of up to several tens of ms. A change in the onboard software configuration was implemented at the end of July 2016, motivated by the need for improved sensitivity to short electromagnetic counterparts associated with gravitational waves detected by LIGO-VIRGO (Ursi et al., 2019). Data from the first part of the period were taken with the same onboard configuration that was active during REF, and so they are safely comparable to data from the latter; in the following period AGILE can switch between two different configurations to accommodate telemetry necessities, at a single orbit level. The second configuration is more permissive, therefore allowing more triggers, which in turn increases the probability of recording a TGF. Finally, the 3D-FIX period starts in January 2018 and is characterized by a recovery of the internal clock precision. The software configuration flexibility is still ongoing as in the second half of the DRIFT period. Absolute timing accuracy at the microsecond level is a key requirement for the association of TGFs to lightning sferics, as discussed in details in L20.

Throughout the rest of this paper we call *WWLLN-identified* TGFs (WI) all those TGFs that are found by virtue of their association with a lightning sferic only; between the REF and 3D-FIX periods they form a

Table 1
Summary of the Data Sets

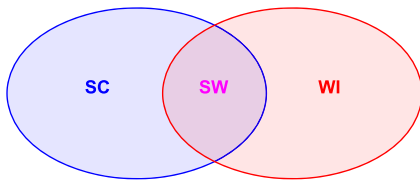| Name	Span	AC shield	Timing accuracy
AC-ON	28 February 2009 to 23 March 2015	On	$\sim 2\mu s$
REF	23 March 2015 to 30 June 2015	Off	$\sim 2\mu s$
DRIFT	01 July 2015 to 31 December 2017	Off	Several tens of ms
3D-Fix	17 January 2018 to 30 September 2018	Off	$\sim 2\mu s$

Figure 2. Venn diagram of the data sets used in this paper. SC: data set obtained with selection criteria. WI: WWLLN-identified data set. SW: SC subset with WWLLN identification.

sample of 278 events. We used the WI events as a starting point of our work: we analyzed their characteristics in order to model our selection criteria on them, with the purpose of refining those criteria and maximize the number of TGFs recognized, while at the same time rejecting as many false events as possible. Those events, and the method used to select them, are described in L20. L20 reports 282 WI events, as four additional TGFs were found after a refinement in their search algorithm; however, this happened when our analysis was already concluded; therefore, we decided against redoing it. We call *selection criteria identified* TGFs (SC) all those TGFs found based on the newly designed selection criteria, regardless of their association to lightning sferics. SC TGFs are the target of this paper, while WI TGFs are the target of the companion paper. A fraction of the SC data set is associated to sferics and therefore included also in the WI data set. We refer to this intersection between the two data sets as *selection criteria and WWLLN identified* TGFs (SW). Figure 2 shows a schematic representation of the TGF data sets used in this paper.

3. Observables and Original Selection Criteria

As mentioned in section 2, triggered data still need to be processed in order to distinguish TGFs from other types of events. We start our search by scanning all the available data streams in search for clusters of counts, irrespective of the onboard trigger. We call a "cluster" a streak of at least 6 counts in the detector occurring within 300μs. We then consider related counts all those that come no later than 300μs from the previous one. This may cause the cluster to continue outside of the original trigger window, which is not a problem since we have at least six seconds of data around each trigger. All count groups that originate from an onboard trigger in the 293μs time window must be selected as clusters by the onground analysis (threshold is either 8 or 7 counts for the onboard logic); however, the ground search can identify many more clusters in the data stream that did not give rise to an onboard trigger. It is possible to calculate several parameters for each cluster, which are then used to determine whether the cluster is classified as a TGF or not. The parameters that we chose to evaluate are the following:

1. Maximum energy (E_{max})
2. Mean energy (E_{avg})
3. Median energy (E_{med})
4. Hardness ratio (HR)
5. Number of counts (N)
6. Uniformity (number of detector segments hit)
7. Duration (Δt)
8. Count rate ($F = N/\Delta t$)

Given the intrinsic spectral hardness of TGFs, energy-related observables are key parameters to disentangle TGF candidates from other, softer events. Maximum energy (E_{max}) is the largest energy measured among the single counts in the cluster. Mean and median energy are cluster-wide quantities; median energy is favored over mean because it is less sensitive to statistic fluctuations. HR is the ratio between counts of energy above 1.4 MeV and the ones below. The threshold value of 1.4 MeV was chosen for historical, hardware-related reasons and could in principle be adjusted.

We define the duration of the cluster (Δt) as the time difference between the first and last event. This is a very coarse measure of duration and will be refined for those clusters subsequently labeled as TGFs. Uniformity, or detector occupation, is a measure of the spreading of the events belonging to a single cluster across the detector planes: Since TGFs at satellite altitude can be approximated to a plane wave, we expect them to involve the whole detector, thus having counts in all of its sectors. Uniformity is related to the spatial symmetry of the cluster counts over the detection planes and is a very efficient way to discard electronic noise and cosmic rays, which both tend to show counts clustered in localized parts of the detector. Uniformity can be measured in several ways. Here, we divide the two MCAL planes in four parts each, for a total of eight segments, and count how many segments are hit by at least one count.

Table 2
The Number of WI TGFs Failing on Any of the Selection Criteria

Criterion	TGFs failing
Any	146
Max E	70
HR	21
n counts	64
Uniformity	14

The original selection criteria (CO, Marisaldi et al., 2014, 2015) were defined by setting thresholds and cuts on four of these parameters, as follows:

1. $E_{max} \leq 30$ MeV
2. $HR \geq 0.5$
3. $N \geq 10$
4. Uniformity criterion: at least one count in each of the four quadrants of MCAL, where a quadrant is defined as half a detection plane, that is, two adjacent segments

4. Methods

In order to improve the original criteria, we developed and tested several, new sets of selection criteria (each labeled CN_x in the following) considering more observables and adjusting the threshold according to the characteristics of the WI data set, following the subsequent steps:

1. Identify which of the original criteria failed most often on the WI data set.
2. Definition of a set of new selection criteria based on the previous diagnostics and application to the full data sets.
3. Validation of the TGF candidates obtained with each selection set.
4. Refinement of the new selection criteria based on validation results.

These steps are detailed in the following paragraphs.

4.1. Original Criteria Diagnostic on WI Data Set

TGFs are considered to have a WWLLN association when there is a sferic no more than 0.5 ms apart; we found 111 events in the REF period and 167 in the 3D-FIX, for a total of 278 (L20). The characteristics of those events are independent from any selection criteria, except for the fact that short TGFs are more likely to have an association (Connaughton et al., 2013) (more on this in paragraph 5.3). We then applied the CO to WI events to see where they failed. The results are shown in Table 2. Criteria on HR and uniformity are the ones working best. We manually examined the events rejected by these criteria and they all were very weak events that would not be recognized as TGFs if not for the WWLLN association. The most problematic criterion appeared to be the cut in maximum energy. The limit value of 30 MeV was set to reject not only cosmic rays but also high-energy candidates of uncertain origin, as described in Marisaldi et al. (2014); however, results shown in Table 2 indicate that many real TGFs exhibit counts with reconstructed energy above 30 MeV, although this energy estimate is most likely due to pileup effects. (Marisaldi et al., 2019) reports a model of the electronic front-end responsible of pileup and deadtime. The problem is complex, as it originates from the behavior of both analog and digital electronics, and cannot be determined by one parameter only. Therefore, we decided to set a higher upper limit to maximum energy and explore other possible ways of rejecting cosmic rays. The criterion on number of counts is also too strict, but allowing for a too low number of counts means increasing the number of false events greatly.

4.2. Definition of a Set of New Selection Criteria

Starting from the CO and according to the value ranges of the WI, we designed several new variations of the selection criteria, shown in Table 3. All these criteria were applied to the full data set, each resulting in a set of candidate TGFs, which need to be assessed for reliability.

Table 3
The Different Sets of Selection Criteria

Name	Uniformity	HR	E_{med}	E_{max}	n counts
CO	Yes	≥ 0.5	–	≤ 30	≥ 10
CN_1	Yes	≥ 0.5	–	≤ 120	≥ 10
CN_2	Yes	≥ 0.5	–	≤ 30	≥ 9
CN_3	Yes	≥ 0.5	–	≤ 120	≥ 9
CN_4	Yes	–	≥ 0.5	≤ 30	≥ 10
CN_5	Yes	–	≥ 0.5	≤ 120	≥ 10
CN_6	Yes	–	≥ 0.5	≤ 30	≥ 9
CN_7	Yes	–	≥ 0.5	≤ 120	≥ 9

4.3. Validation

After applying a set of selection criteria to the whole data set, we need a way of evaluating the true-versus-false events ratio and, more generally, the goodness (reliability) of the obtained TGF candidate set. We applied three methods, of which two qualitative and one quantitative:

1. Longitude distribution of the sample
2. Local time distribution of the sample
3. Quality factor

The two qualitative and most straightforward ways take advantage of the fact that we know where and when to expect TGFs. Being produced by thunderstorms, they are more frequent above equatorial mainland and during early morning or late afternoon. We then expect our candidates to be clustered at longitude values corresponding to land and to follow a modulation with local time. Background cosmic particles events, i.e. events uncorrelated to thunderstorm activity, on the other hand, would appear as a constant baseline, at best slightly modulated by magnetic latitude in the case of the geographic distribution. As a quantitative measure, we compared the average detection rate with the one in a region with scarcity of storms. This method was first used by Briggs et al. (2013) and then in Marisaldi et al. (2015). The control regions extends from -110 to -140 degrees of longitude. The high-density region is the sum of the three "lightning chimneys": the African one from $-10°$ to $30°$, the South-East Asian one from $100°$ to $150°$, and the Central American one from $-90°$ to $-60°$. Hereafter, we call Quality Factor (QF) the ratio between the number of events in the control region and the high-density region. The QF is not normalized for the different span of those two regions, as there is no objective way to estimate how many of the control region events are actually noise: being AGILE on an equatorial orbit, we still expect a small number of thunderstorms even above the open ocean. As another quality flag we consider also the fraction of the WI data set identified by the new selection criteria. The results of the validation will be presented in section 5.

4.4. Criteria Refinement

None of the CN gave satisfactory results in the control region; we then proceeded to analyze those events more closely to understand their origin.

We considered the ratio between the number of counts and the duration, which represents a rough estimate of the count rate of the event. In Figure 3, we show this for events from the control region and events from the three chimneys, and we assume for this purpose that all events in the control region are false events, while all the others are TGFs. The figure shows that false events tend to cluster at low count rate and high energy. TGFs, on the other hand, are mostly low count rate and lower energy. We can verify this by plotting the geographic distribution of events according to count rate and energy: low-count rate, lower-energy events follow the expected longitude distribution for TGFs, peaking above equatorial mainland, while low-count rate, high-energy events are uniformly distributed. High-count rate events also follow the three-chimney structure,
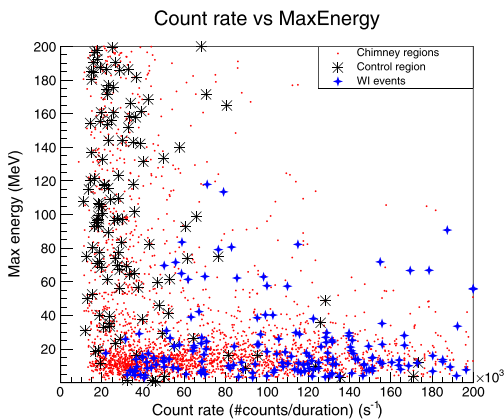
Figure 3. The count rate versus max energy for events occurring in the chimney regions and in the control region.

Table 4
Efficiency of Each Set of Selection Criteria

Name	Number WI selected	Total events selected	Quality factor
CO	121	2,354	18/1966
CN_1	166	2,686	0.011 (26/2,221)
CN_2	158	2,930	0.023 (52/2,276)
CN_3	199	3,531	0.029 (78/2,659)
CN_4	146	2,505	0.009 (20/2,082)
CN_5	177	2,834	0.012 (28/2,335)
CN_6	172	2,962	0.016 (37/2,369)
CN_7	213	3,439	0.019 (52/2,703)

although the pattern is slightly less clean, possibly because of the lower statistics. Remarkably, WI TGFs tend to have higher values of count rate: This is explained by the shorter duration of WI events, as explained in Connaughton et al. (2013) and L20. Energies greater than 30 MeV can be either due to real photons, pileup (Marisaldi et al., 2019) or the presence of counts from cosmic rays, and confirm the need of relaxing the criteria on maximum energy. This led to the introduction of an additional, empirical criterion, as a way to remove even more false events: for count rate below 50 kHz, we only allow events with maximum energy up to 30 MeV. For higher values of count rate, we allow energies up to 120 MeV. We justify this by considering that the probability of pile-up increases for higher values of count rate. All of those thresholds were found empirically, from the values of the studied events, in order to optimize the ratio of events in the active and control regions. The 30-MeV cut on energy also happens to be consistent with the energy cut in the CO. We then reapplied the set of refined criteria to the full data set. This added criterion affects only the CN where the cut on maximum energy was previously set to 120 MeV.

5. Results and Discussion

5.1. Choice of Selection Criteria

Table 4 shows an overview of all the different selections we tested concerning number of WI events selected, total number of TGF events, and the quality factor discussed in section 4.3. Here, we count each cluster as a single event, regardless of its possible association with a multipulse event, as we are considering the efficiency of the criteria in selecting clusters. The multipulse events are discussed in section 5.5. None of the chosen set of criteria optimizes all three parameters reported in Table 4; therefore, a trade-off is necessary. We decided to give more weight to the cleanliness of the sample (a low quality factor), first, and the total number of WI events selected as a second requirement. In this regard, the selection set that proved to offer the best balance is CN_5:

1. Number of counts ≥ 10
2. $E_{med} \geq 0.5$ MeV
3. At least one count in each quadrant
4. If count rate < 50 kHz, $E_{max} \leq 30$ MeV
5. If count rate ≥ 50 kHz, $E_{max} \leq 120$ MeV

This is the set of selection criteria adopted for the 3rd AGILE TGF catalog. All results shown in the rest of this paper correspond to the TGF sample obtained with these criteria. The actual number of events selected is 2,780, as some of the 2,834 turned out to be part of a multipeak event. The sample obtained from this selection represents the largest TGF data set over equator currently available.

5.2. Improvement of the New Sample

As stated in section 1, one goal of this study was to include in the sample those events that were recognized as TGFs by their association with WWLLN, but not from the offline selection algorithm. The old catalog included 279 TGFs in the REF period; in contrast, the new one has 457 TGFs in the REF period and 2,780 in total. Of these 2,780, 177 are associated with a WWLLN sferic. The new criteria have improved the inclusion of high-energy events in particular, thus allowing for a maximum energy of up to 120 MeV. Those high energy counts are however a product of pileup, which affects short and high-fluence events. The analysis reported in Marisaldi et al. (2019) shows that these events are still compatible with a standard RREA
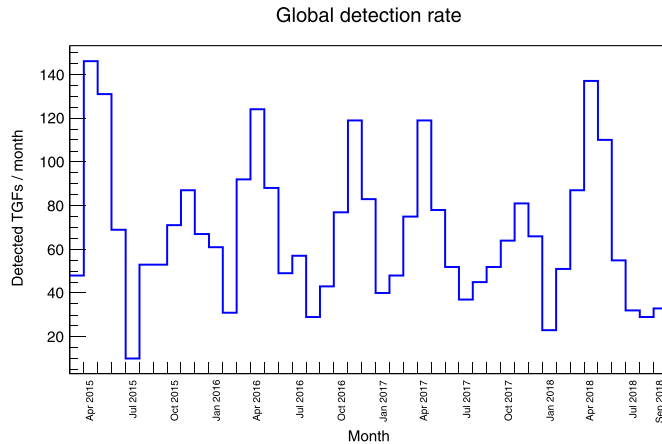
Figure 4. The detection rate of AGILE over the course of the 3 years covered by the catalog. The dip around July 2015 is due to the clock failure, the one at January 2018 corresponds to another period of noisy data.

spectrum, with maximum energy of few tens of MeV, provided that the instrumental effects are carefully accounted for. However, the events affected by pileup are real TGFs and reliable in all other aspects; they should just be considered carefully when calculating the energy spectra. We also found one Terrestrial Electron Beam event, which is described in details in L20. We decided to keep the threshold on the total number of counts relatively high. Lowering the threshold on number of counts, while greatly increasing the number of selected TGFs (see Table 4), was also introducing a large number of false events, as evidenced by the worsening of the quality factor. Those noise events appeared unrelated to the thunderstorm peaks in the longitude plot and had different distributions of their parameters, namely, the energy (i.e., homogeneous instead of Gaussian-like). The additional criterion on count rate alone was not sufficient to completely eliminate them in CN_3 and CN_7, but we would have needed more complex, probability-based algorithms; we preferred discarding those sets. Figure 4 shows the global detection rate for the period covered by the catalog: March 2015 to September 2018. The average detection rate does not change over the years, showing that the behavior of the selection criteria remains consistent along the seasons. The empty period around July 2015 corresponds to the clock failure between the REF and the DRIFT periods. The periodic variation is mostly due to the seasonal variability. The seasonal behavior of the TGF rate is further discussed in section 5.6

5.3. Limitations of the New Sample

While our aim was to be as inclusive as possible with the TGF selection, the new sample is likely affected by limitations and bias. The most obvious one is that we based our criteria on the characteristics of relatively few WWLLN-identified TGFs, detected over a period of twelve months (three in the REF period and nine in the 3D-FIX). It has already been proved that the probability of association with sferics decreases as the duration of the TGF increases, which means that our sample may be biased towards shorter TGFs. We avoided using the duration as a selection criteria for this reason, and also for the difficulty in defining it in an objective way, but shorter TGFs may be different from longer ones also in other ways. Moreover, all reference TGFs were detected during the spring and summer months (REF and 3D-FIX periods; see Table 1) and may, in principle, have specific characteristics different from the ones of TGFs produced by thunderstorm systems developing in other seasons, that is, in different atmospheric conditions. Seasonal behavior is discussed in more detail in section 5.6. Finally, as mentioned in section 5.2, we refrained from including the faintest TGFs, to avoid introducing more false events in our sample; however, this led to the loss of some valid TGFs. It is still possible to recover those events, but it will require a much more sophisticated approach, which was outside the scope of this work. Very faint TGFs, due to the very low number of counts, do not allow robust estimate of the global parameters and a reliable spectral analysis.
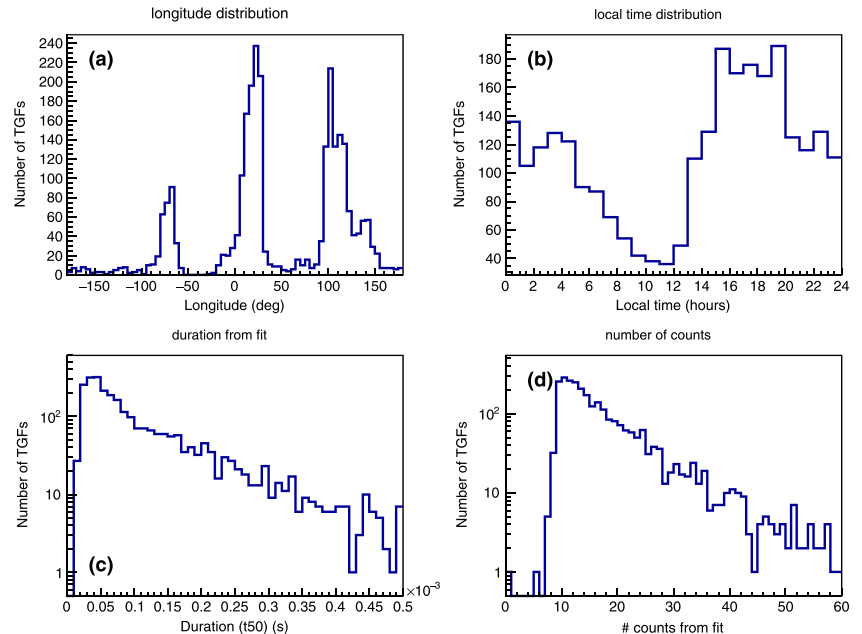
Figure 5. (a) Longitude and (b) local time distribution of the whole data set obtained with the CN_5 criteria set. (c) Duration (t_{50}) distribution of the sample. (d) Intensity (from maximum likelihood fit) distribution of the sample.

5.4. Impact of the Onboard Trigger Logic Configuration

As already stated, the TGF search was applied to the full data stream collected which includes, for every onboard trigger, a span of about 6 to 10 s of data (depending on the configuration of the onboard trigger logic) around the trigger time. Therefore, although the search was not based on the triggers, it was unavoidably affected by the trigger logic configuration, just because the data availability relies on the issuing of an onboard trigger. This, together with the fact that the onboard trigger configuration has changed significantly during the time period considered in this work, made us consider whether the trigger logic configuration is somehow biasing our sample and the associated results. We therefore carried out a retrospective analysis to understand, given the selected TGF sample, which of the trigger time windows was responsible for the data span in which the TGF was found, and the time separation between the TGF and the trigger. The results show that in 96% of the cases the trigger has fired on the 293μs time scale, the sub-millisecond trigger; moreover, in 94% of the cases, the time separation between the TGF time and the trigger time is < 16 ms, indicating that the TGF itself was the cause of the trigger. This is an important result because the sub-millisecond trigger logic configuration has been kept constant during the full time span considered in this work. The static threshold was lowered from 8 to 7 counts from September 2016, but this is not significantly affecting the results since only events with at least ten counts are considered by the chosen selection criteria. These considerations indicate that the AGILE sensitivity for TGFs is uniform along the orbit and during the full time span considered in this work. This is a relevant information to consider when attempting quantitative comparisons with other data sets or when addressing the seasonal variability of the sample.

The 16-ms time window, the one most heavily affected by the introduced configuration changes, is responsible alone for only 2% of the TGFs. Of these, 95% is detected far from the trigger time, meaning that the TGF did not cause the trigger on such a long time scale, but was indeed detected by chance within the available data span.
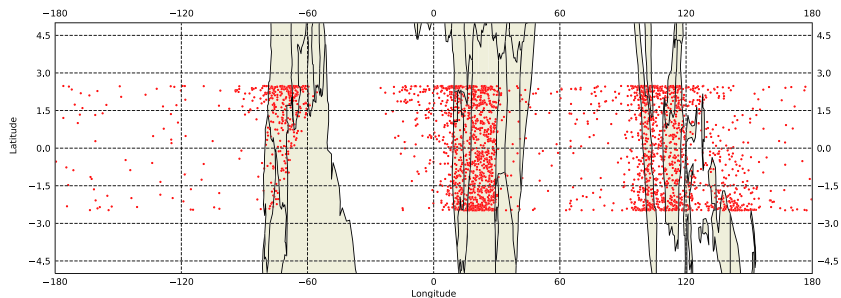
Figure 6. A global map of the catalog sample. The empty area over South America corresponds to the SAA.

5.5. Global Characteristics of the Sample

Figure 5 shows the global distributions of longitude (a), local time (b), duration (t_{50}) (c), and number of counts (d) for the full data set. The duration and intensity shown in panels (c) and (d) are the ones obtained from the maximum likelihood procedure described in L20, not the ones used in the criteria development phase and listed in section 3. The quantities from fit are consistent with the previous catalogs (Marisaldi et al., 2015), but were only calculated on the final sample, to avoid influencing the selection criteria. The initial, operational definition of duration was only used during the development of the criteria and is not included in the publicly available database. We note that in some cases the number of counts shown in panel (d) is lower than 10, which is apparently in contrast with the threshold for TGF identification. This is because the plotted parameter is the TGF intensity resulting from the integral of the maximum likelihood Gaussian fit; therefore, it accounts for both the model and background subtraction. The catalog also includes 95 multipulse events (3.4% of the sample), but only the first peak of each event was considered for this plot. Each multipulse event was analyzed manually, as some peaks were not recognized as independent clusters by the automatic selection and had to be retrieved from the raw data. As a consequence, many of such trailing peaks have properties that do not satisfy the selection criteria (specifically, many of them had fewer than 10 counts) and were therefore excluded from the plots, to avoid confusion. The catalog includes all pulses as single entries, appropriately flagged to distinguish between first and trailing pulses, bringing the total number of entries to 2,903. The fraction of multipulse events is in accordance with Mezentsev et al. (2016), for RHESSI, and also with the previous results for AGILE (Marisaldi et al., 2014), although less strictly. It is not, however, compatible with Foley et al. (2014), which reports for Fermi a much higher occurrence rate; an explanation for this discrepancy is yet to be found. The multipulse TGFs have different shapes and a number of peaks which ranges from two to five. The catalog also includes 128 potential multipulse, that is, events with an irregular light curve that was nonetheless not univocally classifiable as multiple. Those events are also labeled in the catalog, but were treated as normal events.

Finally, Figure 5a also shows a fourth lightning enhancement between -180 and -150 degrees of longitude. This feature is visible in the LIS/OTD lightning maps (Albrecht et al., 2016) and was already reported by Fabró et al. (2015) but the characteristics of TGFs occurring in this area are yet to be studied.

5.6. Geographic and Seasonal Variability

The high number of events detected in a small latitude span result in a high density of events, which in turn allows a fine binning for a study of seasonal and geographical variability. In order to perform this study, we selected the events occurring in the high-density regions (Central Africa, Oceania and Central America, as defined in section 4.3). All the following plots include the complete data set, without distinction of the periods and excluding the trailing peaks of multipulse events.

Figure 6 is a world map with all the events in the catalog. TGFs clearly prefer coastal and inland areas, but there are also several events over the ocean: lightnings over ocean are in fact more frequent at equatorial latitudes than they are elsewhere. The completely empty area over South America corresponds to the South Atlantic Anomaly (SAA), where the MCAL trigger logic is not active. This also explains the smaller number of events observed over South America, as it is noticeable in all following plots. Figure 7 (right panels) shows the local time distribution of the events in the three regions. Africa shows a higher rate of events occurring
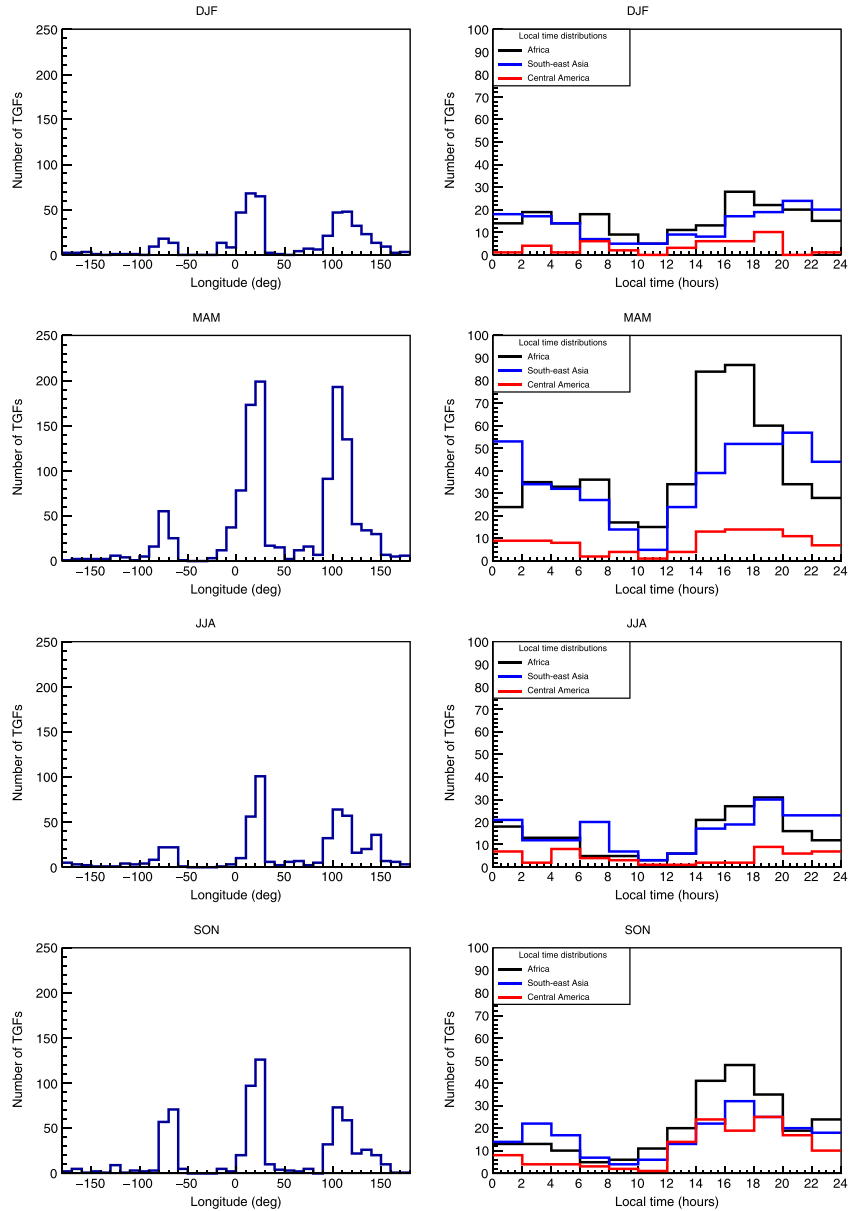
Figure 7. The geographic and local time distributions of all events in the catalog divided by season; the local time plot also divides the events by geographical region. The differences in both distributions follow local and seasonal weather patterns. Seasons are defined as three winter months (DJF), three spring months (MAM), there summer months (JJA) and three fall months (SON).
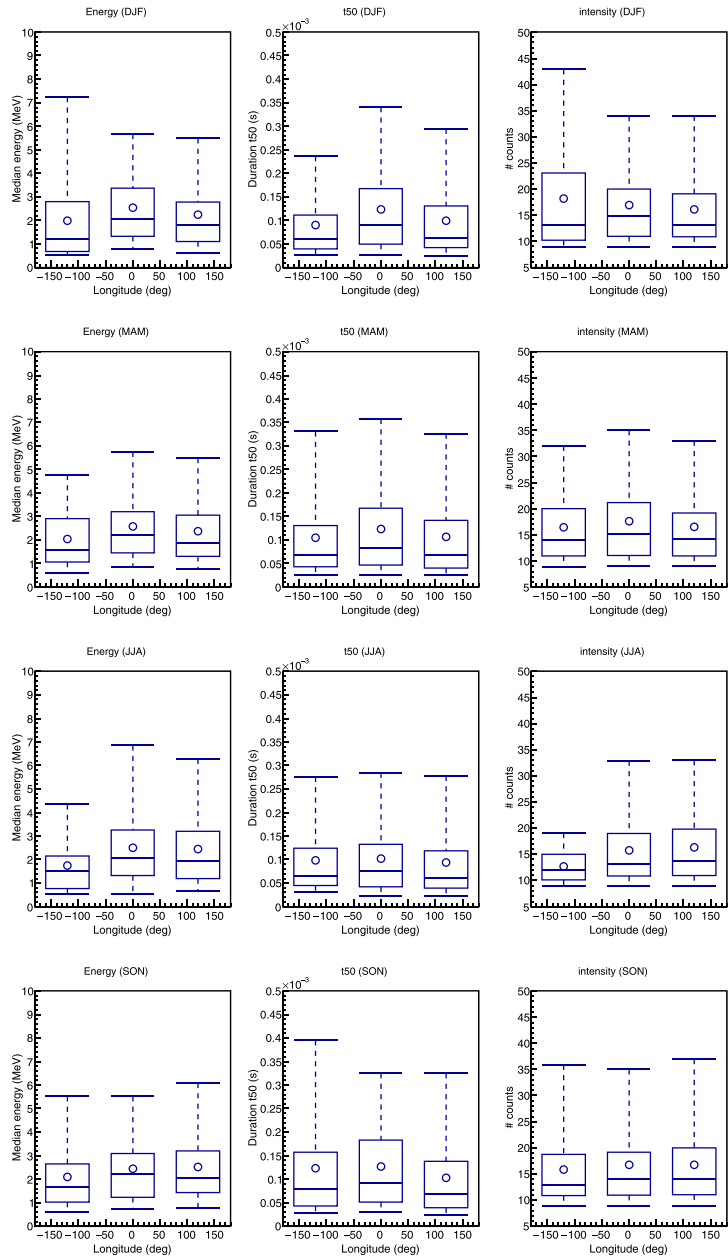
Figure 8. The trend of three characteristic parameters of TGFs: median energy (left panels), duration (center) and number of counts (right), for the three high-density regions and the four seasons. The top and bottom of the boxes represent the upper and lower quartiles of the distribution (75% and 25% of the data points). The end of the lower bar marks 5% of the data points and the end of the upper one marks 95%. The circle is the mean and the line in the box is the median of the distribution.

in the late afternoon compared to the other regions; this is consistent with the observed climatology of the area. Figure 7 presents an overview of all the events divided by the season in which they occur. As can be seen, a clear influence of seasons emerged with maximum at equinox and minimum in solstice. In terms of geographic distribution (panels on the left), we see that the peak over Africa is consistently the highest; this effect is explained by the equatorial orbit of AGILE (see also section 5.7), which covers the Congo basin, a very prolific area for thunderstorms. The number of events is particularly high in spring (March–May) and lowest in winter (December–February). However, during spring the Asian peak grows to almost the same level. The peak over Borneo is very visible in summer and fall (June-August and September-November), however, it is not a seasonal phenomenon: in the spring and fall months a small "bump" on the right of the Indonesian peak is visible. This bump has the same value as the Borneo peak in summer and winter, suggesting that the rate over Borneo is constant and is overpowered by the activity over Java and Sumatra in winter and spring. The fact that the local-time curve for Oceania has the same shape of the one for the other regions indicates that this peak over Borneo is not related to a specific kind of events. Another seasonal small peak is visible over the pacific in winter. This fourth lightning region was already reported in Fabró et al. (2015), but the scarcity of events in that region makes it difficult to draw any conclusions. Our findings are in accordance with the observations of the Optical Transient Detector, as reported in Christian et al. (2003) (see figure 6). The reported maximum of lightning activity in the period September–November over the Amazon basin is visible in our data also, even considering the low number of detected events. Christian et al. (2003) also report that the maximum of activity in Africa shifts from −20° latitude in December–February to +20° in June–August, following the Inter-Tropical Convergence Zone. However, such latitudes are outside the field of view of AGILE, and as a result we see our maximum of activity in March–May and September–November instead. Finally, in their figure 7, panel c, they also report a bimodal structure for the yearly activity rate, with maxima over April and October for the latitude band covered by AGILE; this is very well visible in Figure 4. The local time distributions (Figure 7, panels on the right) also show variations according to the time of the year. In particular, the imbalance between the rate in mornings and in evenings over Africa occurs in spring and fall, and a similar behavior is observed over Central America during fall; this trend seems to be reversed in summer over America. On the other hand, the detection rate in the mornings as opposed to the evenings seems to be comparable all year round in Oceania. Figure 8 shows a set of summary box plots for median energy (left), duration (center) and number of counts (right), divided for the four seasons and for the three lightning chimneys. There is no trend of such parameters with longitude or season; the small differences for the American peak are most likely due to the small number of events recorded there. Therefore, from this analysis, we conclude that there is no statistical evidence for variability of TGF properties such as median energy, duration and intensity with season and longitude, at least in the equatorial band. Therefore, we consider unlikely that our WI events, selected over spring and summer, are introducing a bias related to season in our sample.

5.7. Comparison With the Fermi Catalog

One of the distinct features of the AGILE sample is the dominance of the African peak, which is not observed by other missions; however, we interpret this feature as a product of the very narrow inclination of AGILE (2.5°). As a result, AGILE covers all the equatorial regions, particularly the Congo basin, while at the same time misses out other active regions, such as the Caribbean sea.

To show this, we plot the events from the Fermi catalog (Roberts et al., 2018) which occurred within ±2.5° of latitude and we see that their geographic and local time distributions are compatible with the ones obtained for the AGILE data set (Figure 9). Fermi data are available at https://fermi.gsfc.nasa.gov/ssc/data/access/gbm/tgf/; we used the Offline Search Table for this comparison. The latitude-based selection includes 454 out of 4,135 events detected within the period July 2008 to July 2016. There is thus only partial time overlap between AGILE and Fermi data sets. The African and Asian peaks are comparable between the two sets; so is the American one, but the data from AGILE show a little peak over the Pacific that is not present in the sample from Fermi, possibly due to the lower number of events in the sample. The differences in the local-time distributions are not significant.
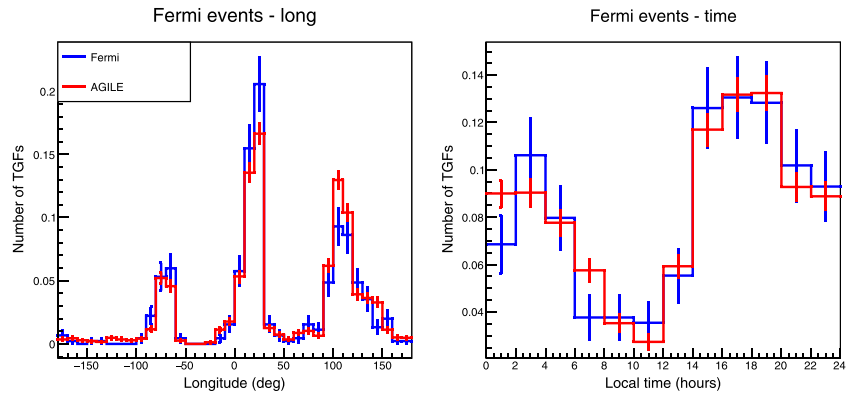
Figure 9. The geographic and local time distributions of AGILE ad Fermi data sets, superimposed and normalized for the total number of events.

6. Conclusions

The new catalog presented here contains 2,780 TGFs detected by AGILE over a 3-years span, and represents the largest data set of TGFs detected over the equatorial region (±2.5° of latitude) so far. The association with WWLLN showed that the selection criteria used for the previous catalogs were inadequate and the characteristics of WI TGFs were the base for the design of new criteria. After testing several sets of new criteria we selected the one that included the highest number of WI TGFs while at the same time maintaining the sample as clean as possible of false events. The reliability of the new sample was tested with the geographic and local-time distributions of the events and with the ratio between events occurring in stormy regions and events occurring in a selected control region. The characteristics of the new sample are consistent with previous observations, namely the Fermi catalog. The seasonal behavior for the various regions is consistent with the global annual lightning activity, reported by Christian et al. (2003); the TGF rate peaks at different times of the year in the different regions, according to local climate. Local weather patterns also influence the shape of the longitude distribution; in particular, the peak over Borneo was not visible in the previous catalogs, and it thus represents an additional improvement. Another active region that was previously undetected is the Pacific chimney. However, no trend related to location or season was found in energy, intensity or duration of the TGFs.

This catalog is openly accessible at this link: https://www.ssdc.asi.it/mcal3tgfcat, and it includes also the lightcurves of all events. The association of TGFs to lightning sferics detected by WWLLN is addressed in L20.

References

Agostinelli, S. (2003). Geant4—A simulation toolkit. *Nuclear Instruments and Methods A*, *506*(3), 250–303.

Albrecht, R., Goodman, S., Buechler, D., Blakeslee, R., & Christian, H. (2016). LIS 0.1 Degree Very High Resolution Gridded Lightning Climatology Data Collection.

Briggs, M. S., Xiong, S., Connaughton, V., Tierney, D., Fitzpatrick, G., Foley, S., & Hutchins, M. L. (2013). Terrestrial gamma-ray flashes in the Fermi era: Improved observations and analysis methods. *Journal of Geophysical Research: Space Physics*, *118*, 3805–3830. https://doi.org/10.1002/jgra.50205

Carlson, B. E., Lehtinen, N. G., & Inan, U. S. (2007). Constraints on terrestrial gamma ray flash production from satellite observation. *Geophysical Research Letters*, *34*, 8. https://doi.org/10.1029/2006GL029229

Christian, H. J., Blakeslee, R. J., Boccippio, D. J., Boeck, W. L., Buechler, D. E., Driscoll, K. T., & Stewart, M. F. (2003). Global frequency and distribution of lightning as observed from space by the Optical Transient Detector. *Journal of Geophysical Research*, *108*(D1), 4005. https://doi.org/10.1029/2002JD002347

Chronis, T., Briggs, M. S., Priftis, G., Connaughton, V., Brundell, J., Holzworth, R., & Stanbro, M. (2016). Characteristics of thunderstorms that produce terrestrial gamma ray flashes. *Bulletin of the American Meteorological Society*, *97*(4), 639–653. https://doi.org/10.1175/BAMS-D-14-00239.1

Connaughton, V., Briggs, M. S., Xiong, S., Dwyer, J. R., Hutchins, M. L., Grove, J. E., & Wilson-Hodge, C. (2013). Radio signals from electron beams in terrestrial gamma ray flashes. *Journal of Geophysical Research: Space Physics*, *118*, 2313–2320. https://doi.org/10.1029/2012JA018288

Cummer, S. A., Lyu, F., Briggs, M. S., Fitzpatrick, G., Roberts, O. J., & Dwyer, J. R. (2015). Lightning leader altitude progression in terrestrial gamma-ray flashes. *Geophysical Research Letters*, *42*, 7792–7798. https://doi.org/10.1002/2015GL065228

Dwyer, J. R., & Cummer, S. A. (2013). Radio emissions from terrestrial gamma-ray flashes. *Journal of Geophysical Research: Space Physics*, *118*, 3769–3790. https://doi.org/10.1002/jgra.50188

Dwyer, J. R., & Smith, D. M. (2005). A comparison between Monte Carlo simulations of runaway breakdown and terrestrial gamma-ray flash observations. *Geophysical Research Letters*, *32*, L22804. https://doi.org/10.1029/2005GL023848

Fabró, F., Marisaldi, M., van der Velde, O. A., & Fuschino, F. (2015). Analysis of global terrestrial gamma ray flashes distribution and special focus on AGILE detections over South America. *Journal of Atmospheric and Solar-Terrestrial Physics*, *124*, 10–20. https://doi.org/10.1016/j.jastp.2015.01.009

Fishman, G. J., Bhat, P. N., Mallozzi, R., Horack, J. M., Koshut, T., Kouveliotou, C., & Christian, H. J. (1994). Discovery of intense gamma-ray flashes of atmospheric origin. *Science*, *264*(5163), 1313–1316.

Foley, S., Fitzpatrick, G., Briggs, M. S., Connaughton, V., Tierney, D., McBreen, S., & Wilson-Hodge, C. (2014). Pulse properties of terrestrial gamma-ray flashes detected by the Fermi Gamma-Ray Burst Monitor. *Journal of Geophysical Research: Space Physics*, *119*, 5931–5942. https://doi.org/10.1002/2014JA019805

Gjesteland, T., Østgaard, N., Collier, A. B., Carlson, B. E., Eyles, C., & Smith, D. M. (2012). A new method reveals more TGFs in the RHESSI data. *Geophysical Research Letters*, *39*, L05102. https://doi.org/10.1029/2012GL050899

Grefenstette, B. W., Smith, D. M., Hazelton, B. J., & Lopez, L. I. (2009). First RHESSI terrestrial gamma ray flash catalog. *Journal of Geophysical Research*, *114*, A02314. https://doi.org/10.1029/2008JA013721

Hazelton, B. J., Grefenstette, B. W., Smith, D. M., Dwyer, J. R., Shao, X. M., Cummer, S. A., & Holzworth, R. H. (2009). Spectral dependence of terrestrial gamma-ray flashes on source distance. *Geophysical Research Letters*, *36*, L01108. https://doi.org/10.1029/2008GL035906

Labanti, C., Marisaldi, M., Fuschino, F., Galli, M., Argan, A., Bulgarelli, A., & Trifoglio, M. (2009). Design and construction of the mini-calorimeter of the AGILE satellite. *Nuclear Instruments and Methods in Physics Research A*, *598*, 470–479. https://doi.org/10.1016/j.nima.2008.09.021

Lindanger, A., Marisaldi, M., Maiorana, C., Sarria, D., Albrechtsen, K., stgaard, N., Galli, M., Ursi, A., Labanti, C., Tavani, M., Pittori, C., & Verrecchia, F. (2020). The 3rd AGILE Terrestrial Gamma Ray Flash catalog. Part I: Association to lightning sferics. *Journal of Geophysical Research: Atmospheres*, *125*, e2019JD031985. https://doi.org/10.1029/2019JD031985

Mailyan, B. G., Briggs, M. S., Cramer, E. S., Fitzpatrick, G., Roberts, O. J., Stanbro, M., & Dwyer, J. R. (2016). The spectroscopy of individual terrestrial gamma-ray flashes: Constraining the source properties. *Journal of Geophysical Research: Space Physics*, *121*, 11,346–11,363. https://doi.org/10.1002/2016JA022702

Marisaldi, M., Argan, A., Ursi, A., Gjesteland, T., Fuschino, F., Labanti, C., & Gianotti, F. (2015). Enhanced detection of terrestrial gamma-ray flashes by AGILE. *Geophysical research letters*, *42*, 9481–9487. https://doi.org/10.1002/2015GL066100

Marisaldi, M., Fuschino, F., Labanti, C., Galli, M., Longo, F., Del Monte, E., et al. (2010). Detection of terrestrial gamma ray flashes up to 40 MeV by the AGILE satellite. *Journal of Geophysical Research*, *115*, A00E13. https://doi.org/10.1029/2009JA014502

Marisaldi, M., Fuschino, F., Tavani, M., Dietrich, S., Price, C., Galli, M., & Chen, A. (2014). Properties of terrestrial gamma ray flashes detected by AGILE MCAL below 30 MeV. *Journal of Geophysical Research: Space Physics*, *119*, 1337–1355. https://doi.org/10.1002/2013JA019301

Marisaldi, M., Galli, M., Labanti, C., Østgaard, N., Sarria, D., Cummer, S. A., & Verrecchia, F. (2019). On the high-energy spectral component and fine time structure of terrestrial gamma-ray flashes. *Journal of Geophysical Research: Atmospheres*, *124*, 7484–7497. https://doi.org/10.1029/2019JD030554

Mezentsev, A., Østgaard, N., Gjesteland, T., Albrechtsen, K., Lehtinen, N., Marisaldi, M., & Cummer, S. (2016). Radio emissions from double RHESSI TGFs. *Journal of Geophysical Research: Atmospheres*, *121*, 8006–8022. https://doi.org/10.1002/2016JD025111

Neubert, T., Østgaard, N., Reglero, V., Blanc, E., Chanrion, O., Oxborrow, C. A., & Bhanderi, D. D. V. (2019). The ASIM mission on the International Space Station. *Space Science Reviews*, *215*(2), 26. https://doi.org/10.1007/s11214-019-0592-z

Picone, J. M., Hedin, A. E., Drob, D. P., & Aikin, A. C. (2002). NRLMSISE-00 empirical model of the atmosphere: Statistical comparisons and scientific issues. *Journal of Geophysical Research*, *107*, 1468. https://doi.org/10.1029/2002JA009430

Roberts, O. J., Fitzpatrick, G., Stanbro, M., McBreen, S., Briggs, M. S., Holzworth, R. H., & Mailyan, B. G. (2018). The First Fermi-GBM Terrestrial Gamma Ray Flash Catalog. *Journal of Geophysical Research: Space Physics*, *123*, 4381–4401. https://doi.org/10.1029/2017JA024837

Smith, D. M., Lopez, L. I., Lin, R. P., & Barrington-Leigh, C. (2005). Terrestrial gamma-ray flashes observed up to 20 MeV. *Science (New York, N.Y.)*, *307*, 1085–1088. https://doi.org/10.1126/science.1107466

Tavani, M., Barbiellini, G., Argan, A., Boffelli, F., Bulgarelli, A., Caraveo, P., & Giacomazzo, M. (2009). The AGILE mission. *Astronomy and Astrophysics*, *502*(3), 995–1013. https://doi.org/10.1051/0004-6361/200810527

Ursi, A., Tavani, M., Verrecchia, F., Marisaldi, M., Argan, A., Trois, A., & Tempesta, P. (2019). A new AGILE MCAL configuration to detect gamma-ray bursts and sub-threshold events in the multimessenger era. *The Astrophysical Journal*, *871*(1), 27. https://doi.org/10.3847/1538-4357/aaf28f

Paper II

The 3rd AGILE Terrestrial Gamma-ray Flashes Catalog. Part I: Association to Lightning Sferics

Lindanger, A. and Marisaldi, M. and Maiorana, C. and Sarria, D. and Albrechtsen, K. and Østgaard, N. and Galli, M. and Ursi, A. and Labanti, C. and Tavani, M. and Pittori, C. and Verrecchia, F.

The 3rd AGILE Terrestrial Gamma Ray Flash Catalog. Part I: Association to Lightning Sferics

A. Lindanger[1] [iD], M. Marisaldi[1,2] [iD], C. Maiorana[1] [iD], D. Sarria[1] [iD], K. Albrechtsen[1] [iD], N. Østgaard[1] [iD], M. Galli[3] [iD], A. Ursi[4], C. Labanti[2], M. Tavani[4], C. Pittori[5,6] [iD], and F. Verrecchia[5,6] [iD]

[1]Birkeland Centre for Space Science, Department of Physics and Technology, University of Bergen, Bergen, Norway, [2]INAF-OAS Bologna, Bologna, Italy, [3]ENEA, via Martiri di Monte Sole 4, Bologna, Italy, [4]INAF-IAPS Roma, Rome, Italy, [5]Space Science Data Center - Agenzia Spaziale Italiana, Roma, Italy, [6]INAF - Osservatorio Astronomico di Roma, Monte Porzio Catone, Italy

Abstract We present a complete and systematic search for terrestrial gamma-ray flashes (TGFs), detected by AGILE, that are associated with radio sferics detected by the World Wide Lightning Location Network (WWLLN) in the period February 2009 to September 2018. The search algorithms and characteristics of these new TGFs will be presented and discussed. The number of WWLLN identified (WI) TGFs shows that previous TGF selection criteria needs to be reviewed as they do not identify all the WI TGFs in the data set. In this analysis we confirm with an independent data set that WI TGFs tend to have shorter time duration than TGFs without a WWLLN match. TGFs occurs more often on coastal and ocean regions compared to the distribution of lightning activity. Several multipulse TGFs were identified and their WWLLN match are always associated with the last gamma-ray pulse. We also present the first Terrestrial Electron Beam detected by AGILE. This data set together with the TGF sample identified by selection criteria (companion paper Maiorana et al., 2020) constitute the 3rd AGILE TGF catalog.

1. Introduction

Terrestrial gamma-ray flashes (TGFs) are sub-millisecond bursts of energetic photons produced in the Earth's atmosphere and are associated with lightning flashes (Dwyer, 2012). They were first observed by the BATSE instrument onboard the Compton Gamma-ray Observatory in 1991 and were reported by Fishman et al. (1994). Since then, TGFs have been detected by RHESSI (Albrechtsen et al., 2019; Grefenstette et al., 2009; Gjesteland et al., 2012; Østgaard et al., 2015; Smith et al., 2005), Fermi (Briggs et al., 2013; Roberts et al., 2018), AGILE (Marisaldi et al., 2010, 2014, 2015), and BeppoSAX (Ursi et al., 2017). The newest addition to space missions capable of detecting TGFs is the Atmospheric-Space Interactions Monitor (ASIM) mission, which became operational in June 2018 (Neubert et al., 2019).

In the first era of TGF detection, gamma-ray data from satellites provided the main insight into the physics of TGFs. However, to expand our knowledge supporting data from ground-based stations are necessary. As TGFs are associated with lightning flashes, the geolocation of the lightning associated to the TGF provides the source location of the TGF. To perform spectral analysis of a TGF, the production location is vital to correctly model the propagation of photons through the atmosphere reaching the satellite.

There are two main methods to identify TGFs in gamma-ray data. The gamma-ray data can be filtered by search algorithms, using some selection criteria (SC) to find the TGFs. These SC are not trivial to decide and are a trade-off between a clean sample of fewer but bright TGFs with low contamination of false TGFs, and a large sample containing more faint TGFs with risk for contamination from false TGFs. After the TGFs are identified with SC, they can be correlated with lightning flashes detected by ground stations. The other method is to start with lightning measurements and look at gamma-ray data detected by the satellite at the time of lightning. This method is able to identify weaker TGFs but is limited by the efficiency of the lightning network. The last method has previously been performed on RHESSI (Albrechtsen et al., 2019; Østgaard et al., 2015; Smith et al., 2016) and Fermi data (McTague et al., 2015), using ground-based lightning data.

In 2015, the AGILE TGF detection rate increased with one order of magnitude after the anticoincidence (AC) shield acting on the onboard mini-calorimeter (MCAL) was disabled (Marisaldi et al., 2015).

Table 1
Main Characteristics of the Different Data Sets

Name	Date	AC shield	Timing accuracy
AC-ON	28 February 2009 to 23 March 2015	On	~2 µs
REF	23 March 2015 to 30 June 2015	Off	~2 µs
DRIFT	01 July 2015 to 31 December 2017	Off	Several tens of ms
3D-FIX	17 January 2018 to 30 September 2018	Off	~2 µs

This has led to an intensive search for TGFs in the AGILE data, to further populate the AGILE TGF catalog.

For the first time, a complete and systematic search for TGFs based on time correlation with the World Wide Lightning Location Network (WWLLN) has been applied to all available MCAL data up to September 2018. The search for TGFs based only on WWLLN data has no bias from SC, other than the WWLLN efficiency itself. As the WWLLN detection efficiency is limited (Abarca et al., 2010; Bürgesser, 2017; Rudlosky & Shea, 2013), not all TGFs can be identified in the satellite data using time correlation with WWLLN data. Therefore, a WWLLN identified (WI) TGF sample can make the basis for deciding appropriate new SC to identify TGFs without associated WWLLN detections. These new SC are discussed in the companion paper by Maiorana et al. (2020), hereafter referred to as M20.

In the following sections, we present the data sets and the methods used in this analysis, the results from the different data periods of AGILE, a discussion of the findings, and a summary and conclusions section at the end.

2. Data Sets

The MCAL onboard AGILE includes 30 independent self-triggering CsI(TI) scintillator bars with an energy range ~0.35–100 MeV (Labanti et al., 2009). One should note that MCAL is triggered; for example, data are stored in the internal memory and sent to ground only if a significant excess of counts is detected in the specific time window and does not run in continuous data acquisition mode. Therefore, only a fraction of the measured data is downloaded to telemetry. Additional information on the instrument performance is included in M20.

We divide the MCAL data into four different subsets characterized by the absolute timing accuracy and if the AC shield is active on the instrument or not. A summary of the data sets is shown in Table 1.

The AC-ON data set spans from 28 February 2009 to 23 March 2015 . In this period, the AC shield is active on MCAL and strongly limit the detection of brief duration events (Marisaldi et al., 2014) such as TGFs. The onboard absolute timing accuracy is on ~2 µs level.

The reference (REF) data set spans from 23 March 2015 to 30 June 2015. The AC shield is disabled for MCAL from the onset of this period, resulting in an enhanced TGF detection rate (Marisaldi et al., 2015).

The DRIFT data set spans from 1 July 2015 to 31 December 2017. An issue with the onboard GPS caused a degradation of the AGILE µs timing performance and the absolute time accuracy started "drifting". This drift is a systematic offset in time that remains constant for periods between days and weeks, and then suddenly "jumps" to a different value. The AGILE team performed a time correction of the offset using housekeeping data, resulting in an absolute timing accuracy of several tens of milliseconds.

The 3D-FIX data set spans from 17 January 2018 to 30 September 2018 . After the DRIFT period, the GPS partly recovered and the AGILE team is able to perform a time correction down to ~2 µs level, thus restoring the original timing accuracy of the instrument.

Lightning data are obtained from the WWLLN (Rodger et al., 2009) and provide time and geolocation by detecting very low frequency sferics produced by lightning flashes. Although many different sensors and lightning detection networks have been used in TGF studies (Marshall et al., 2013), WWLLN has become a standard choice and a benchmark following the work by Connaughton et al., (2010, 2013).

The timing uncertainty of WWLLN depends on the location uncertainty. Abarca et al. (2010) found an average location error of 4.03 km in the northward direction and an error of 4.98 km in the westward direction.

Hutchins et al. (2012) report that in 2011, WWLLN located 61% of the strokes within 5 km. Østgaard et al. (2013) assumed a time and location accuracy of 45 μs and 15 km, respectively. In this work, we assume a location uncertainty of 15 km as well.

3. Method

In this paper, two methods are used to search for TGFs. Stacking analysis, and the so-called "search for clusters analysis." Both methods are based on time correlation with WWLLN detections.

3.1. Stacking Analysis

For every WWLLN detection within 1,000 km from the subsatellite point, a MCAL photon list is built according to equation (1), which is the time difference between the WWLLN detection and the list of counts detected by MCAL, corrected for propagation time. These photon lists are then superposed and binned. The motivation for this is to identify the few photons associated to lightning that would be indistinguishable from background without WWLLN association.

$$\delta t = \text{time}_{\text{MCAL}} - \text{time}_{\text{propagation}} - \text{time}_{\text{WWLLN}}. \tag{1}$$

The 1,000-km limit, which we will call the TGF field of view (FOV), is selected because most TGFs are detected within ~500 km from the subsatellite point, and very few farther away than 800 km, as it will be shown in section 4, consistent with earlier results (Collier et al., 2011; Cummer et al., 2005; Marisaldi et al., 2019). The propagation time of the photons is calculated assuming a production altitude of 15 km, which is a fair assumption based on modeling results from Dwyer and Smith (2005) and the expectation that TGFs detected from space are preferentially produced close to thunderstorm cloud tops.

3.2. Search for Clusters Analysis

As stacking analysis relies on timing accuracy on few hundred of microseconds or better to be effective, a new "search for clusters analysis" (SFC) was developed and implemented due to the decreased timing accuracy in the DRIFT period. The method was then also applied to the REF and 3D-FIX periods. The idea is to look at light curves and only keep histogram bars with large counts per 100 μs, assuming that a TGF is seen as an increased flux of counts, or a "cluster of photons" in a light curve. This is possible as the relative timing accuracy of MCAL count timestamps is still at microseconds level and the absolute timing offset is on tens of milliseconds level. The signal is defined to be a time window close to the WWLLN detection, and the background signal is defined to be some seconds before the WWLLN detection, well separated from the signal. The algorithm is described below and in Figure 1.

1. Build a light curve of MCAL photon data for each WWLLN detection for both signal and background time intervals.
2. Build the distribution of number of counts per 100 μs bin for each light curve.
3. Superpose the distributions of counts per 100 μs bin found in Point 2.
4. Set a threshold based on signal vs. background.
5. Define events with counts per 100 μs bin higher than the selected threshold as TGF candidates.

Based on the distribution of counts per 100 μs in Figure 1c, we select a threshold of x counts per 100 μs. The fraction of false positive TGFs is estimated by taking the integral from the selected threshold to 20 for background and signal and divide the background integral by the signal integral. The threshold is a trade-off between the number of TGF candidates and the fraction of false positive TGFs. Note that a plot equivalent to Figure 1c is shown with real data in Figures 3c and 5c, while a plot equivalent to Figure 1d is shown with real data in Figure 4c.

3.3. TGF Candidates Processing

After the TGF candidates are identified, each TGF is fitted by a Gaussian function on top of a constant background by means of an unbinned maximum likelihood technique. The intensity, peak time, and duration of each TGF are extracted from the parameters of the fit. The TGF duration is calculated as $t_{50} = 1.349\sigma$, where σ is the standard deviation from the Gaussian fit, and t_{50} is the central time interval including 50% of the counts. This method is described in Marisaldi et al. (2015).
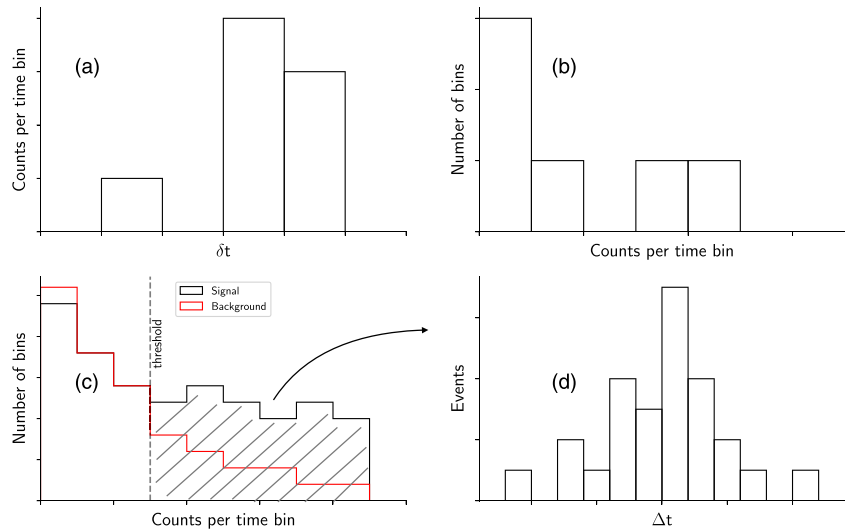
Figure 1. Illustration of the search for clusters analysis. (a) A single light curve associated with a WWLLN detection. (b) Distribution of number of counts per time bin for the single light curve. (c) Superposed distributions of number of counts per time bin associated to WWLLN detections in black and superposed distribution of background in red. A threshold is indicated by a dotted line. (d) The time difference between events with counts per time bin over the selected threshold, and WWLLN detections, corrected for propagation time.

If a TGF is associated with several WWLLN detections within the δt range of the light curve, the algorithm will report the same TGF several times, depending on the number of associated WWLLN detections. We remove the duplicates by keeping the entry corresponding to the closest WWLLN detection in time.

We also determine if the TGFs occurs over land, coast, or ocean. Like the First Fermi-GBM TGF catalog (Roberts et al., 2018), we use the pre-calculated distance to shore file (https://www.soest.hawaii.edu/wessel/gshhg/) that is provided from the Global Self-consistent, Hierarchical, High-resolution Geography Database (Wessel & Smith, 1996). We define the coast as ± 150 km from the shoreline.

4. Results

In this section, the results of the analysis for the different data sets are presented. The number of TGF candidates and the expected fraction of spurious signal, incorrectly identified as TGFs, are shown in Table 2. The fraction of incorrectly identified TGFs is estimated by taking the integral from the selected threshold to 20 for background and signal and divide the background integral by the signal integral. The threshold is 4 for REF and 5 for 3D-FIX.

Table 2
Number of TGFs Associated to WWLLN and Expected Background Contamination

Name	#TGFs	Fraction of incorrectly identified TGFs
AC-ON	0	n/a
REF	111	0.03
DRIFT	310–1,294	n/a
3D-FIX	171	0.01

Abbreviations: TGFs, terrestrial gamma-ray ashes; WWLLN, World Wide Lightning Location Network.
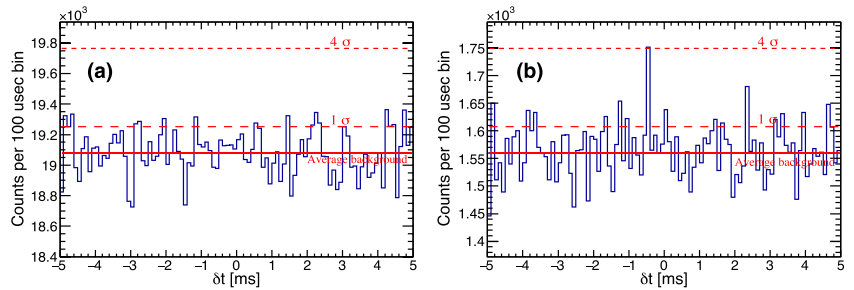
Figure 2. AC-ON period. (a) Stackplot of counts detected by MCAL for 440,234 WWLLN detections within 1,000 km from subsatellite point. (b) Stackplot of counts detected by MCAL for WWLLN detections within 300 km from the subsatellite point, and energies below 100 MeV.

4.1. AC-ON Period

A stack plot of the MCAL data for 440,234 WWLLN detections is shown in Figure 2a. There is no significant peak visible at $\delta t \approx 0$ confirming that the AC shield is suppressing the TGF signal as suggested in Marisaldi et al. (2014).

As most TGF-WWLLN matches occur within few hundred kilometer from the subsatellite point, a new stack plot, shown in Figure 2b, was calculated considering only WWLLN detections within 300 km from the subsatellite point and MCAL counts below 100 MeV. The distance and energy limit enhances the signal-to-noise

Figure 3. REF period. (a) Stack plot of MCAL counts for 9,754 WWLLN detections within 1,000 km from subsatellite point. (b) Energy of the counts in (a) detected by MCAL in the full energy band 0.35–100 MeV. The unit of the color scale is counts per 100 μs per energy bin. (c) Distribution of counts per 100 μs time bin for the REF period. The signal includes counts with $|\delta t| \leq 500$ μs and is normalized per 1 ms per 9,754 WWLLN detection. The background includes counts with δt between -3.5 and -2 s and is normalized per 1.5 s per 10,453 WWLLN detection. (d) WI TGFs in black, and all WWLLN detections in the TGF FOV in red, as a function of distance from the subsatellite point to WWLLN detection. Each distribution is normalized to 1.

Figure 4. DRIFT period. Plots (b), (c), and (d) have the same color legend. (a) Stackplot of MCAL counts for 265,165 WWLLN detections within 1,000 km from subsatellite point. (b) WI TGFs in black, WI TGFs that are also identified with SC in green (SW), and all WWLLN detections in the TGF FOV in red, as a function of distance from the subsatellite point to WWLLN detection. Each distribution is normalized to 1. (c) The time difference between TGFs and WWLLN detections, corrected for propagation time, for the TGF candidates. (d) The time difference between TGFs and WWLLN detections, corrected for propagation time, as a function of contacts, which is a proxy for time as one contact is the orbit number counting from the first AGILE orbit.

ratio as TGFs far from the subsatellite point are weaker due to atmospheric attenuation, and counts above 100 MeV are expected mostly to be cosmic rays. Note that a peak of four standard deviations is obtained at $\delta t \approx -0.5$ ms. This could be due to the detection of the first counts associated to TGFs before the AC shield suppresses the counts. However, this peak is farther from $\delta t = 0$ than expected; therefore, we cannot draw firm conclusions on it.

The SFC analysis is not applied to the AC-ON data set, as the AC-shield suppresses any clusters associated to WWLLN detections.

4.2. REF Period

Figure 3a shows the stack plot for 9754 WWLLN detections in the REF period. The significance of the peak is ~27 standard deviations and shows a clear time correlation between counts in MCAL and WWLLN detections. If we remove known TGFs identified by Marisaldi et al. (2015), we obtain a 16 sigma peak showing that not all TGFs-WWLLN matches are found by the SC described in Marisaldi et al. (2015).

The energy of the counts in Figure 3a is shown in Figure 3b. The peak at $\delta t \approx 0$ indicates the energy range of the photons associated with the TGFs. Note that the energy spectrum is not corrected for background and instrumental effects.

The SFC analysis is applied to the data to identify the TGFs. Based on the distribution of counts per 100 μs bin shown in Figure 3c, we select a threshold of 4 counts per 100 μs. This identifies a total of 111 WI TGFs. The expected contamination of false positive TGFs is 3%. If we exclude the 111 WI TGFs from the stack plot in Figure 3a, we obtain no peak at $\delta t \approx 0$. Thus, the SFC analysis identifies all significant TGF-WWLLN matches in the REF period data set.

Figure 3d shows the distance between the subsatellite point and the associated WWLLN detection for the WI TGFs in black, and all WWLLN detections in the TGF FOV in red. The distance bin size is chosen so that the
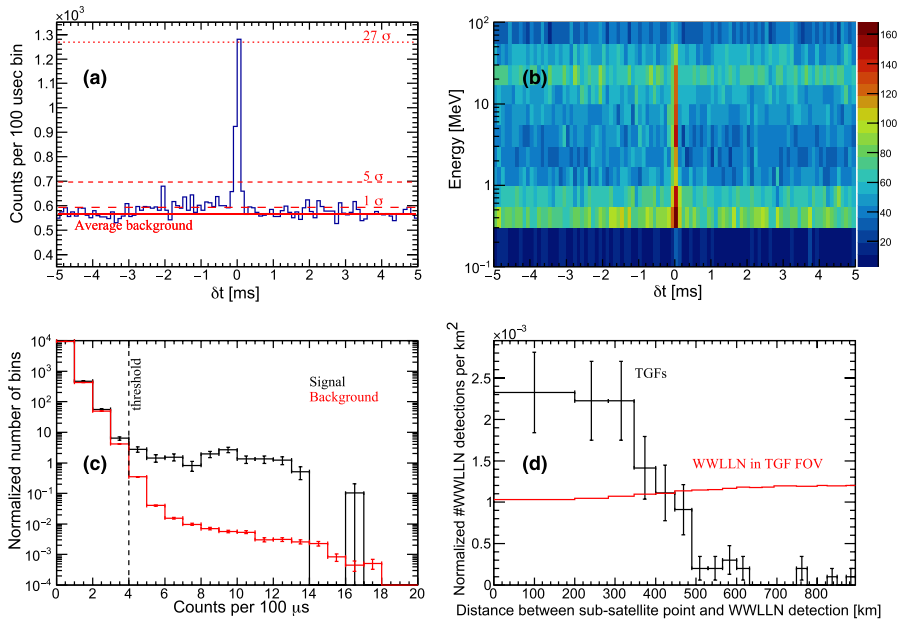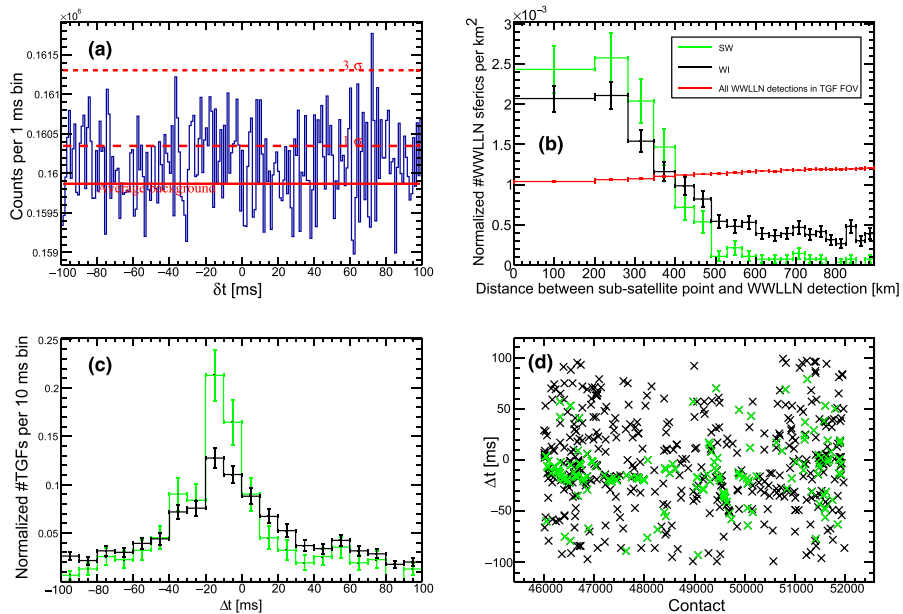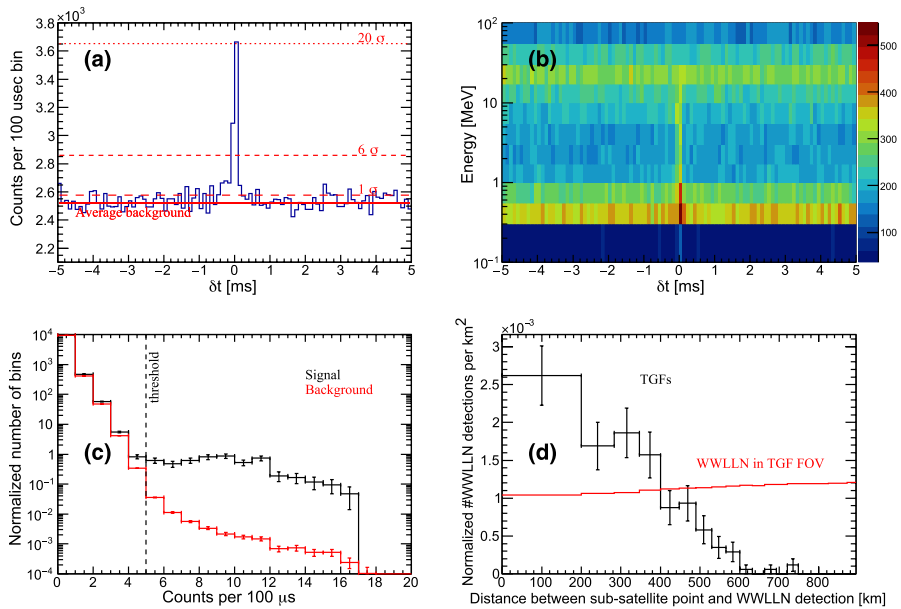
Figure 5. 3D-FIX period. (a) Stackplot of MCAL counts for 42,243 WWLLN detections within 1,000 km from subsatellite point. (b) Energy of the counts in (a) detected by MCAL in the full energy band 0.35–100 MeV. The unit of the color scale is counts per 100 µs per energy bin. (c) Distribution of counts per 100 µs time bin for the 3D-FIX period. The signal includes counts with $|\delta t| \leq 500$ µs and is normalized per 1 ms per 42,243 WWLLN detection. The background includes counts with δt between -2.7 and -2.1 s and is normalized per 0.6 s per 47,966 WWLLN detection. (d) Number of TGFs, as a function of distance from the subsatellite point to WWLLN detection, and all the WWLLN detections in the TGF FOV. Each distribution is normalized to 1.

circular area, corresponding to each bin, is constant and equal to 125, 664 km². In agreement with Cummer et al. (2005), Collier et al. (2011), and Marisaldi et al. (2019), most TGFs are detected within ~500 km from the subsatellite point, and very few TGF are detected farther away than 800 km. The red WWLLN distribution is not flat due to the nonconstant latitude distribution of the WWLLN detections and AGILE's orbital inclination angle.

4.3. DRIFT Period

Figure 4a shows the stack plot for the DRIFT period with δt range of ± 100 ms and bin size of 1 ms. As the absolute time accuracy is not on microsecond level, data do not show a peak at $\delta t \approx 0$. The SFC analysis is applied in order to improve the signal-to-noise ratio, and all events with δt within ± 100 ms and a threshold of 7 counts per 100 µs is defined as TGF candidates. We choose 7 counts following the same approach as REF and 3D-FIX but the threshold needed to be higher due to the decreased absolute timing accuracy. This identifies 1,294 WI TGF candidates shown in Figures 4b, 4c, and 4d in black color. However, there is evidence of a flat component in Figure 4b in the WI TGFs. TGFs with distance longer than ~500 km from the subsatellite point can be real TGFs, but we do not expect many of them. The flat component indicates the contamination of false events and suggests that at least 33% of the WI TGF candidates are false TGFs.

To further enhance the signal-to-noise ratio, we compared the WI TGF candidates from the SFC analysis with the TGFs identified with SC in M20. There are 310 joint TGFs (selection criteria satisfied and WWLLN identified, SW hereafter) and these are shown in green color in Figures 4b, 4c, and 4d. (See figure 2 in the companion paper M20 for a graphical overview of SC, SW, and WI TGFs.) The SW TGFs further enhance the signal-to-noise ratio as seen in Figure 4b, where the number of TGF-WWLLN matches close to the subsatellite point are relatively higher for the SW TGFs, and lower for distances far from the subsatellite point, compared to the WI TGF candidates. Also in Figure 4c, we see a higher peak and lower background component for the SW TGFs, compared to the WI TGF candidates.
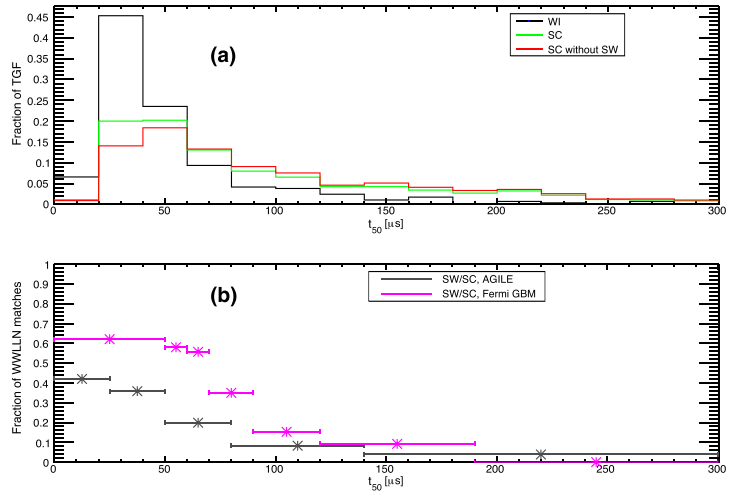
Figure 6. (a) Normalized t_{50} distributions for WI, SC, and SC without SW. (b) Comparison of fraction of WWLLN matches from AGILE and Fermi TGFs.

From Figure 4c, we see that the absolute timing accuracy in the DRIFT period is ~30 ms, with an offset of approximately −17 ms. However, the offset varies with time. That is evident in Figure 4d, which shows the time difference between the TGF and the WWLLN detection, corrected for propagation time, as a function of time between March 2016 and May 2017. "Contact" is the orbit number counting from the first orbit of AGILE, where one orbit is ~94 min. Considering only the SW TGFs, we see that between contact 46,000 and 48,000, the timing uncertainty seems to be approximately ±25 ms, and between contact 49,200 and 49,800, there seems to be a linear negative slope, indicating a constantly decreasing offset. After contact ~51,000 the absolute timing uncertainty is approximately ±100 ms.

4.4. 3D-FIX Period

Figure 5 is the result from the same analysis as for the REF period, applied to the 3D-FIX period. These plots show the same characteristics as in Figure 3. Figure 5a has a peak of ~20 standard deviations at $\delta t \approx 0$. Based on the signal-background ratio in Figure 5c, we selected a threshold of 5 counts per 100 μs and identified a total of 171 TGFs. The expected contamination of false TGFs is 1% . If we exclude the 171 WI TGFs from the stack plot in Figure 5a, we obtain no peak at $\delta t \approx 0$, indicating that the SFC analysis identifies all the WI TGFs in this data set, also. The energy peak in Figure 5b is less bright compared to Figure 3b in the REF period because the noise has slightly increased. This is the reason why we cannot set the threshold to 4 as in the REF period. The differences between the REF and 3D-FIX periods in terms of significance of the TGF peak, energies, and TGF detection rate can be explained by the combination of seasonal variability (different data span) and increased instrumental noise.

5. Discussion

The stacking analysis for the REF period reveals that the selection criteria in Marisaldi et al. (2015) needs to be reviewed as the SC did not identify all the WI TGF found by the SFC analysis. This is discussed further in the companion paper by M20.

Due to the large timing uncertainty in the DRIFT period, we are dependent on selection criteria to identify the TGFs. Therefore, we exclude the DRIFT period from the discussion, except in section 5.1, to prevent introducing a bias due to selection criteria and to keep the sample purely based on WI TGFs. In the following sections, we discuss the absolute timing accuracy of AGILE, the duration of WI TGFs, multipulse TGFs, local time and geographical distributions, and the first Terrestrial Electron Beam (TEB) detected by AGILE.

5.1. Diagnostics of AGILE Timing Accuracy by TGF-WWLLN Correlation

After the issue with the onboard GPS at the start of the DRIFT period, the AGILE team performed a time correction procedure using housekeeping data. The SFC analysis provides an independent assessment of the goodness and effectiveness of this time correction. Due to the low absolute timing uncertainties of WWLLN, it is possible to use TGF-WWLLN correlations to correct the onboard satellite clock. This has previously been done on RHESSI data (Mezentsev et al., 2016). The TGF-WWLLN correlations evidenced previously unidentified trends in the DRIFT period, impossible to identify by house keeping data measurements (Figures 4c and 4d). In the 3D-FIX period, the authors of this paper identified a systematic time offset of 4 ms, constant with time. This time offset correction is already implemented in the gamma-ray data processing pipeline by the AGILE team, prior to the complete data analysis resulting in this paper. In this regard, checking AGILE data against WWLLN data provides a valuable, independent diagnostics of the AGILE timing accuracy.

5.2. Duration of TGFs and the Rate of Association with WWLLN

In Figure 6a, we see that the t_{50} distribution of WI TGFs peaks in the range 20–40 µs. This is consistent with the predictions by Connaughton et al. (2013) showing that a TGF will produce a radio signal with a peak spectral energy density at 10 kHz (which is similar to lightning, and where WWLLN is optimized for), when $t_{50} = 21.5$ µs.

The t_{50} distribution of the TGFs identified with the SC in M20, and the t_{50} distribution of the TGFs in SC that are not WI are also shown. These samples are biased towards longer duration with respect to the WI sample. Figure 6b shows the fraction SW/SC for AGILE TGFs and Fermi-GBM TGFs (from figure 3 in Connaughton et al., 2013). It is hard to do a quantitative comparison of the distributions as the instruments are different, the orbital inclination are different, as well as the data span and the efficiency of WWLLN over different geographical regions. However, the trend from the two missions are compatible, where brief duration TGFs have a higher fraction of WWLLN matches.

5.3. Multipulse TGFs

Mezentsev et al. (2016) observed 16 multipulse TGFs out of 314 TGF-WWLLN matches in RHESSI data. In these 16 multipulse TGFs, the WWLLN detection is always associated with the last TGF peak. Motivated by this finding, we manually checked the 284 TGFs in the REF- and 3D-FIX period looking for multipulse TGFs. We identified seven multipulse TGFs shown in Figures 7a to 7g. The first (a) multipulse TGF is already reported in Mezentsev et al. (2016). TGF (b) has a small time separation between pulses, suggesting that it might not be a multipulse event. However, the two candidate pulses exhibit different spectral characteristics. The second pulse is much softer than the first pulse suggesting spectral evolution with time. The third multipulse TGF (c) has a rather weak first peak. The other multipulse TGFs (d–g) are clearly multipulse TGFs with ~0.5 ms between each peak. The multipulse TGFs observed by AGILE confirms, with an independent data set the findings of Mezentsev et al. (2016), that the WWLLN detection is always associated with the last pulse in a multipulse TGF. We found no multipulse TGFs with WWLLN associated with the first pulse. Note that sometimes WWLLN detect the same lightning flash twice, as seen in Figure 7e. The distance between the locations of the "double" lightning detections are within the uncertainties of WWLLN suggesting that the stroke responsible for the two detections is the same.

5.4. Local Time and Geographical Distribution

Figure 8a shows the local time distribution of AGILE WI TGFs compared with TGFs with a WWLLN association from the first Fermi-GBM TGF catalog (Roberts et al., 2018). The position of Fermi is restricted to the same latitude band as AGILE, giving a total of 142 Fermi-GBM TGFs with a WWLLN match. Figure 8b shows the longitudinal distributions of AGILE WI TGFs and Fermi-GBM TGFs with a WWLLN match. As in Figure 8a, Fermi is restricted to ±2.5° latitude. The distributions show a consistent behavior.

Like in Albrechtsen et al. (2019), we investigated whether the TGFs are located over land, ocean, or coast. We define the coast as ±150 km from the shoreline, and the simultaneous WWLLN matches are used to estimate the production origin of the TGFs. In Table 3, the number and percentage of TGFs detected over ocean, coast and land are shown. We also calculated the number and percentage of WWLLN detections within the TGF FOV in the REF and 3D-FIX period. This parameter basically accounts for both satellite exposure time and WWLLLN efficiency over the different regions. Note that the WWLLN percentage distribution is not uniform like in Albrechtsen et al. (2019) where WWLLN detections below RHESSI is approximately
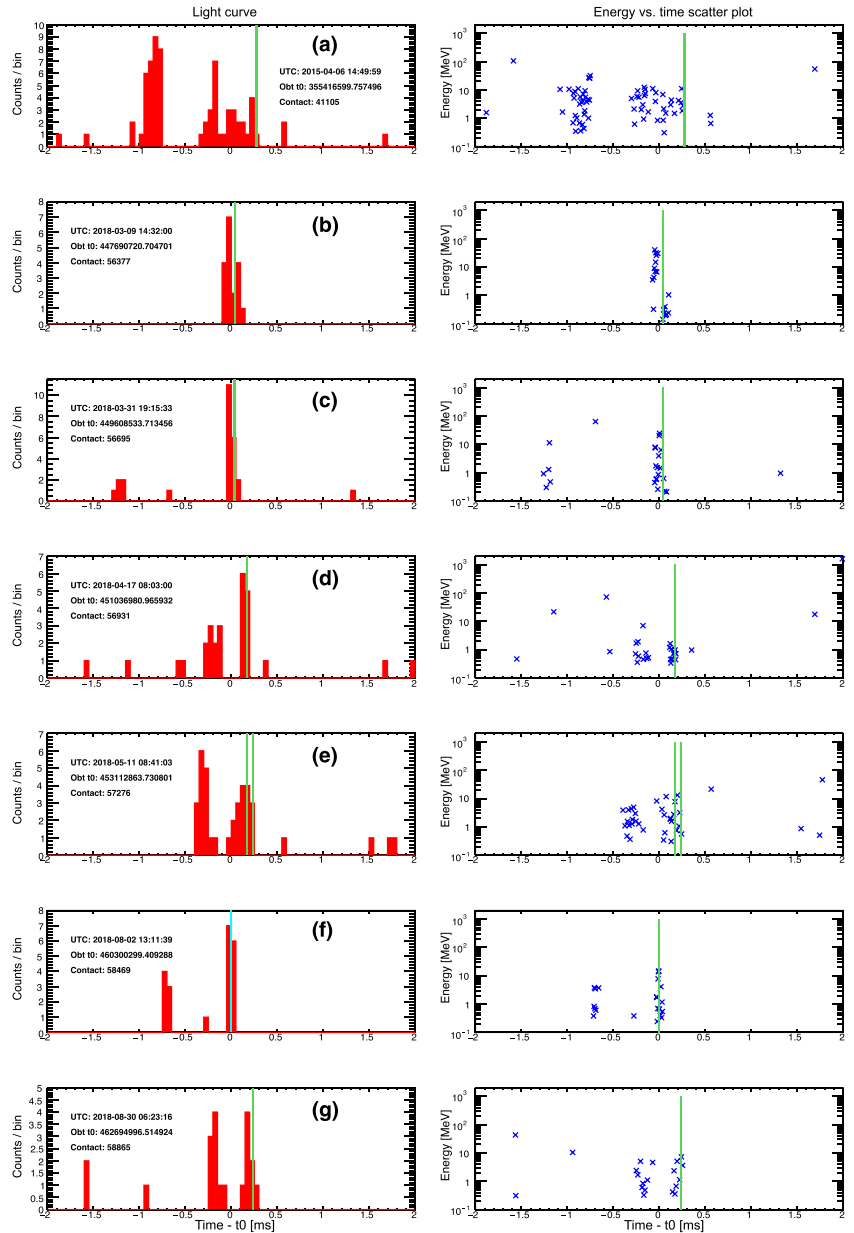
Figure 7. Light curve and energy vs. time scatter plot for the seven multipulse TGFs found in the REF and 3D-FIX periods. The bin size is 50 μs. The WWLLN detections, corrected for propagation time, is indicated as a green vertical line.
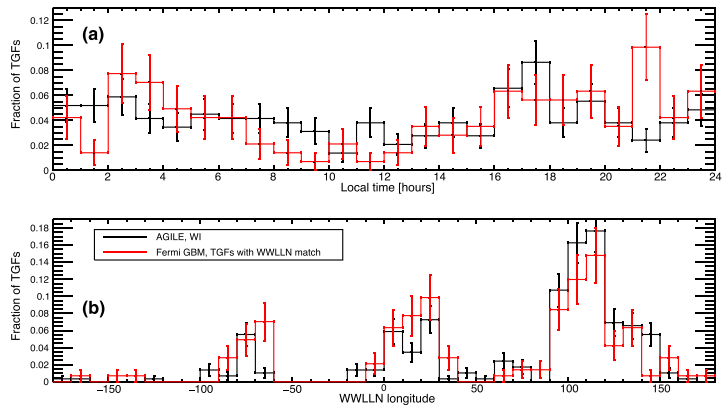
Figure 8. (a) Local time of AGILE WI TGFs in black, and Fermi-GBM TGFs with WWLLN match in red. (b) Longitude distributions of AGILE WI TGFs in black, and Fermi-GBM TGFs with WWLLN match in red. Fermi is restricted to the same latitude band as AGILE ($\pm2.5°$).

one third each over ocean, coast, and land. This may be explained by the much large orbital inclination of RHESSI compared to AGILE. It is evident that TGFs detected by AGILE, like both Fermi-GBM and RHESSI (Albrechtsen et al., 2019; Roberts et al., 2018), are mostly detected over coastal regions. If TGFs follow exactly the lightning distribution, the probability of having a TGF at the coast would be 0.51. If we consider whether a TGF is produced at the coast or not as a binomial process with probability of success 0.51, the probability of having 184 successes out of 282 trials is in the order of 10^{-7}. Doing the same calculation for land and ocean gives a probability of $\sim10^{-5}$ and 0.02, respectively. This shows that the ocean, land, coast distribution of TGFs does not follow the ocean, land, coast distribution of lightning detected by WWLLN. TGF production occurs relatively more often ±150 km from the coastline. This is also evident in Figure 9, where the AGILE WI TGFs, and TGFs with WWLLN matches from Fermi-GBM, are plotted together with the LIS 0.1 Degree Very High Resolution Gridded Lightning Full Climatology (VHRFC) dataset. The VHRFC dataset is gridded lightning rate density from the Lightning Imaging Sensor (LIS) from 1998 to 2013 (Albrecht et al., 2016). The color bar indicates flash rate density with unit flashes per square km per year. Fermi-GBM is not restricted to $\pm2.5°$ latitude in this figure. The three maps corresponds to each of the three lightning chimneys in Figure 8b. Figure 9a shows mainly Colombia and Ecuador, Figure 9b shows West and Central Africa, and Figure 9c shows the Borneo Sumatra regions. The lack of TGFs south of Colombia is due to the South Atlantic Anomaly. We see that the TGFs follow the lightning activity, but clusters more on the coast than over ocean and land. Where there is high lightning activity on land, like in the Congo basin, more TGFs are observed. These results contribute to the discussion of the geographical asymmetry in the TGF/lightning ratio, already addressed in Smith et al. (2010), Fuschino et al. (2011), Briggs et al. (2013), and recently discussed in Fabró et al. (2019) specially concerning the physical characteristics of thunderstorms over Africa.

Table 3
Land, Ocean, Coast Distributions for WI TGFs Detected by AGILE, and Land, Ocean, Coast Distributions of WWLLN Detections Within the TGF FOV in the Same Period the TGFs was Detected

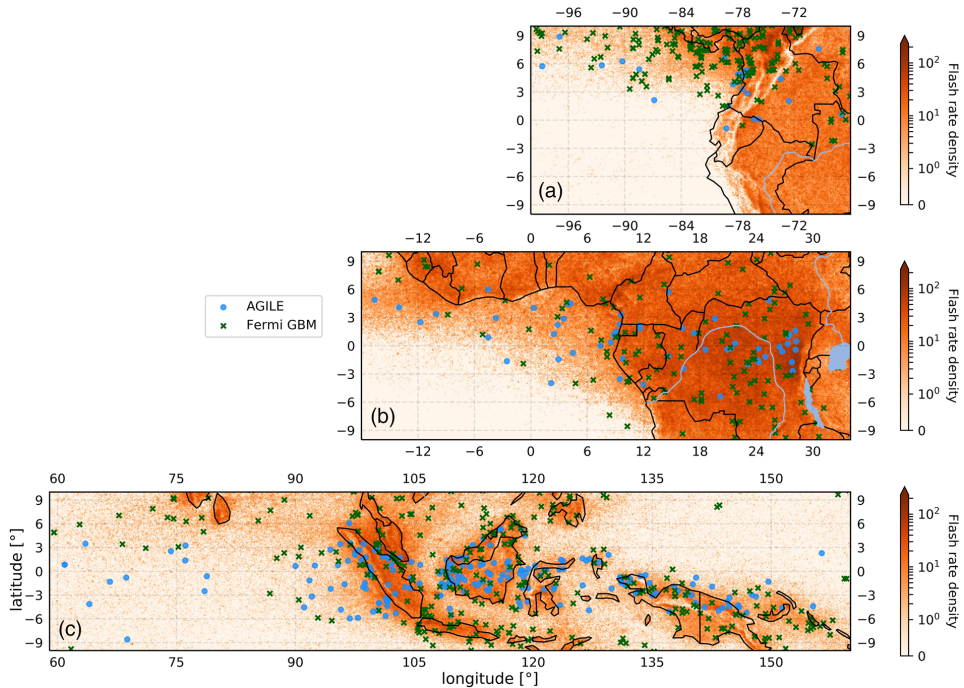|	#TGFs	%TGFs	#WWLLN	%WWLLN
Ocean	49	17.4%	483 498	21%
Coast	184	65.2%	1 155 716	51%
Land	49	17.4%	634 793	28%
Total	282	100%	2 274 007	100%

Figure 9. The position WWLLN matches associated to TGFs detected by AGILE and Fermi-GBM. The color scale shows flash rate density with unit flashes per square kilometer per year from the LIS 0.1 Degree VHRFC dataset.

5.5. Terrestrial Electron Beam

High-energy photons of the TGF will interact with the atmosphere and produce secondary electrons and positrons. A fraction of the secondary electrons and positrons produced above 30–40 km can reach high enough altitudes (above ~120 km) where they stop interacting significantly with the atmosphere (Sarria et al., 2015). The geomagnetic field will then guide the motion of the electrons and positrons so that they stay together, forming a TEB. The TEBs were first described in Dwyer et al. (2008). Spacecraft detecting TGFs, such as BATSE, RHESSI, Fermi, BeppoSAX and ASIM, also detect TEBs (Dwyer et al., 2008; Roberts et al., 2018; Sarria et al., 2019; Ursi et al., 2017).

Here we present the first high confidence TEB identified in AGILE data. The TEB took place over the Indian ocean on 6 April 2018 20:51:50.404601 UTC. There is no lightning activity detected by WWLLN within 1 s of the TEB in a radius of 1,000 km from the subsatellite point, except two WWLLN matches close to the southern footpoint of the magnetic field line that intercepts AGILE at the moment of observation, ~733 km from the subsatellite point. We pick the closest WWLLN match to the magnetic footpoint as the most likely sferic associated with the TGF producing the TEB.

In Figure 10, lightning activity ±1 minute around the time of the TEB, the location of AGILE's subsatellite point, and the magnetic field line and footpoints are shown. The southern magnetic footpoint is located at −8.60° latitude and 68.80° longitude. The subsatellite point of AGILE is located at −2.04° latitude and 68.08° longitude and AGILE has an altitude of 462.6 km. In Figure 10a, it is evident that there is no WWLLN detections directly below AGILE, but there is a cluster of WWLLN detections at the southern magnetic footpoint. The WWLLN match associated with the TEB are found in this cluster. The WWLLN match occurs 0.087 ms before the start of TEB, corrected for propagation time, assuming a straight line.
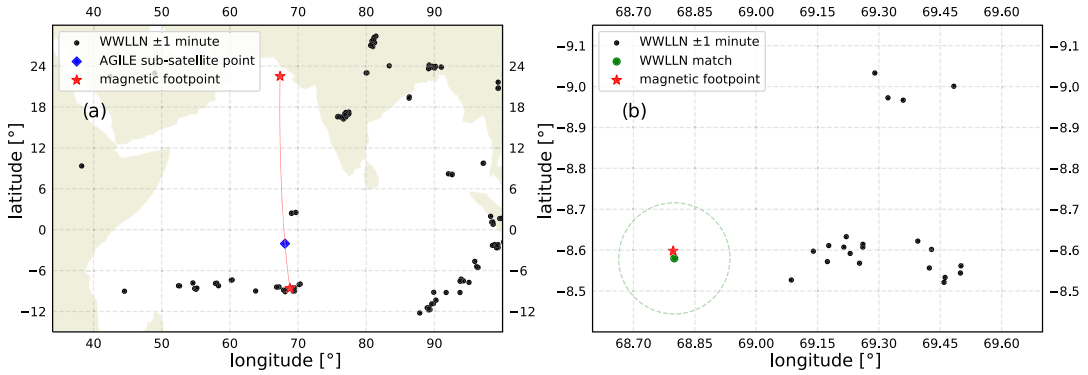
Figure 10. Two maps of the TEB event. (a) Map of WWLLN detections ± 1 minute around the TEB, AGILE's subsatellite point, and the magnetic field line and footpoints. (b) Zoomed version of the southern magnetic footpoint. The 15-km uncertainty of the WWLLN match is indicated as a green circle.

Figure 11 shows the detected energy spectra and time histogram of the TEB, together with a simulation of the TEB. The TEB is simulated with a Geant4 based code assuming a TGF with a RREA energy spectrum proportional to $1/E \cdot \exp(-E/7.3 \text{ MeV})$, up to 40 MeV. The Geant4 code is the same as in Sarria et al. (2019). The source TGF is initiated at the WWLLN match with an assumed production altitude of 15 km. The photons are beamed upward with a Gaussian distribution with $\sigma_\theta = 30°$. The Earth's magnetic field is obtained using the IGRF-12 model (Thébault et al., 2015) and the atmosphere composition is obtained using the NRLMSISE-00 model (Picone et al., 2002). Geant4 includes all the relevant processes physical processes of photon, electron and positron transportation (Compton scattering, pair production, Rayleigh scattering, photoelectric absorption electrons inelastic and elastic scatterings, bremsstrahlung, position annihilation). The photons, electrons, and positrons reaching satellite altitude are saved including their energy and momentum information. The output from this simulation is used as input to the AGILE mass model, which simulates
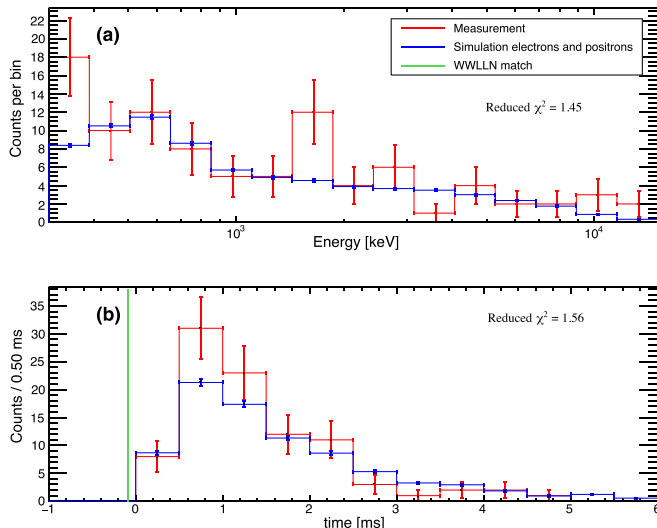

Figure 11. (a) Energy spectra of the detected TEB. (b) Time histogram of the TEB. The measurement by AGILE is in red color. The simulation of the TEB in blue color. The WWLLN match corrected for propagation time is shown in green color.

AGILE's detector response to the particles, in terms of energy spectrum and arrival time. The energy spectrum accounts for energy resolution of the instrument. The proper attitude of the satellite at the TEB time is accounted for. This is shown in blue color in Figure 11. To evaluate the compatibility between the simulation and the measurement, we performed a χ^2 test. The reduced χ^2 value is 1.45 for the energy spectrum and the critical value for compatibility is 1.69 (14 degrees of freedom). The reduced χ^2 value is 1.56 for the time histogram and the critical value for compatibility is 1.94 (8 degrees of freedom and the start of the TEB is a free parameter.). Figure 11 shows the resulting energy spectrum (a) and light curves (b), and the results of the χ^2 tests. In both cases, the simulation is compatible with the measurement.

Given the observed WWLLN detection and the magnetic field line configuration, as well as consistency of simulated and measured spectra and time profile, we conclude that the event on 6 April 2018 20:51:50.404601 UTC is the first observation of a TEB detected by AGILE. The detection of TEBs is difficult for AGILE given the amount of screening material surrounding the detector, as pointed out in the comparative study by Sarria et al. (2017).

6. Summary and Conclusions

In this paper, we analyzed more than 9 years of AGILE gamma-ray data, searching for TGFs correlating with lightning strokes detected by WWLLN. We confirm that the AC shield suppresses the TGF signal in the AC-ON period, as suggested in Marisaldi et al. (2014). We have also selected a total of 282 WWLLN identified (WI) TGFs with high absolute timing accuracy (REF and 3D-FIX period), and 310 WI TGFs with low absolute timing accuracy, which also is satisfied by selection criteria (DRIFT period).

The search for clusters (SFC) method proved successful in identifying all significant TGFs with a WWLLN match where the absolute timing accuracy of AGILE is high. These WI TGFs provided a basis for improvements in selection criteria discussed in the companion paper M20. In the DRIFT period, when AGILE experienced absolute timing issues, the SFC method together with the selection criteria provided a very useful TGF-WWLLN data set capable of independent diagnostics of the AGILE timing accuracy. In the 3D-FIX period, the authors also identified a constant systematic offset of 4 ms.

The analysis of the WI TGF sample can be summarized as follows:

1. The duration of TGFs and the rate of association with WWLLN is assessed and shows, in agreement with Connaughton et al. (2013), that brief duration TGFs have a higher fraction of WWLLN matches than longer duration TGFs.
2. Seven multipulse TGFs detected by AGILE confirms the findings of Mezentsev et al. (2016) that a WWLLN detection associated with a multipulse TGF is always associated with the last pulse. No counterexamples were found.
3. The local time and geographical longitude distributions of WI TGFs, detected by AGILE, is consistent with TGFs with a WWLLN match detected by Fermi GBM.
4. The ocean, land, coast distribution of TGFs does not follow the ocean, land, coast distribution of lightning detected by WWLLN. TGF production occurs relatively more often ±150 km from the coastline.
5. The first TEB detected by AGILE is identified with a WWLLN detection close to the magnetic footpoint of the satellite. Measured and simulated energy spectra and time profiles are consistent.

A catalog of the TGFs, including the TEB, from the REF, DRIFT, and 3D-FIX period are available online for the scientific community (www.ssdc.asi.it/mcal3tgfcat).

References

Abarca, S. F., Corbosiero, K. L., & Galarneau Jr., T. J. (2010). An evaluation of the Worldwide Lightning Location Network (WWLLN) using the national lightning detection network (NLDN) as ground truth. *Journal of Geophysical Research*, *115*, D18206. https://doi.org/10.1029/2009JD013411

Albrecht, Rachel, I., Goodman, S., Buechler, D., Blakeslee, R. J., & Christian., H. (2016). Lis 0.1 degree very high resolution gridded lightning full climatology (vhrfc) [vhrfc_lis_frd]. dataset available online from the NASA Global Hydrology Center DAAC, Huntsville, Alabama, U.S.A. https://ghrc.nsstc.nasa.gov/hydro/details/lisvhrfc

Albrechtsen, K. H., Østgaard, N., Berge, N., & Gjesteland, T. (2019). Observationally weak TGFs in the RHESSI data. *Journal of Geophysical Research: Atmospheres*, *124*, 287–298. https://doi.org/10.1029/2018JD029272

Briggs, M. S., Xiong, S., Connaughton, V., Tierney, D., Fitzpatrick, G., Foley, S., et al. (2013). Terrestrial gamma-ray flashes in the fermi era: Improved observations and analysis methods. *Journal of Geophysical Research: Space Physics*, *118*, 3805–3830. https://doi.org/10.1002/jgra.50205

Bürgesser, R. E. (2017). Assessment of the World Wide Lightning Location Network (WWLLN) detection efficiency by comparison to the lightning imaging sensor (lis). *Quarterly Journal of the Royal Meteorological Society*, *143*(708), 2809–2817. https://doi.org/10.1002/qj.3129

Collier, A. B., Gjesteland, T., & Østgaard, N. (2011). Assessing the power law distribution of TGFs. *Journal of Geophysical Research*, *116*, A10320. https://doi.org/10.1029/2011JA016612

Connaughton, V., Briggs, M. S., Holzworth, R. H., Hutchins, M. L., Fishman, G. J., Wilson-Hodge, C. A., et al. (2010). Associations between fermi gamma-ray burst monitor terrestrial gamma ray flashes and sferics from the World Wide Lightning Location Network. *Journal of Geophysical Research*, *115*, A12307. https://doi.org/10.1029/2010JA015681

Connaughton, V., Briggs, M. S., Xiong, S., Dwyer, J. R., Hutchins, M. L., Grove, J. E., et al. (2013). Radio signals from electron beams in terrestrial gamma ray flashes. *Journal of Geophysical Research: Space Physics*, *118*, 2313–2320. https://doi.org/10.1029/2012JA018288

Cummer, S. A., Zhai, Y., Hu, W., Smith, D. M., Lopez, L. I., & Stanley, M. A. (2005). Measurements and implications of the relationship between lightning and terrestrial gamma ray flashes. *Geophysical Research Letters*, *32*, L08811. https://doi.org/10.1029/2005GL022778

Dwyer, J. R. (2012). The relativistic feedback discharge model of terrestrial gamma ray flashes. *Journal of Geophysical Research*, *117*, A02308. https://doi.org/10.1029/2011JA017160

Dwyer, J. R., Grefenstette, B. W., & Smith, D. M. (2008). High-energy electron beams launched into space by thunderstorms. *Geophysical Research Letters*, *35*, L02815. https://doi.org/10.1029/2007GL032430

Dwyer, J. R., & Smith, D. M. (2005). A comparison between monte carlo simulations of runaway breakdown and terrestrial gamma-ray flash observations. *Geophysical Research Letters*, *32*, L22804. https://doi.org/10.1029/2005GL023848

Fabró, F., Montanyà, J., van der Velde, O. A., Pineda, N., & Williams, E. R. (2019). On the TGF/lightning ratio asymmetry. *Journal of Geophysical Research: Atmospheres*, *124*, 6518–6531. https://doi.org/10.1029/2018JD030075

Fishman, G. J., Bhat, P. N., Mallozzi, R., Horack, J. M., Koshut, T., Kouveliotou, C., et al. (1994). Discovery of intense gamma-ray flashes of atmospheric origin. *Science*, *264*(5163), 1313–1316. https://doi.org/10.1126/science.264.5163.1313

Fuschino, F., Marisaldi, M., Labanti, C., Barbiellini, G., Del Monte, E., Bulgarelli, A., et al. (2011). High spatial resolution correlation of AGILE TGFs and global lightning activity above the equatorial belt. *Geophysical Research Letters*, *38*, L14806. https://doi.org/10.1029/2011GL047817

Gjesteland, T., Østgaard, N., Collier, A. B., Carlson, B. E., Eyles, C., & Smith, D. M. (2012). A new method reveals more TGFs in the RHESSI data. *Geophysical Research Letters*, *39*, L05102. https://doi.org/10.1029/2012GL050899

Grefenstette, B. W., Smith, D. M., Hazelton, B. J., & Lopez, L. I. (2009). First RHESSI terrestrial gamma ray flash catalog. *Journal of Geophysical Research*, *114*, A02314. https://doi.org/10.1029/2008JA013721

Hutchins, M. L., Holzworth, R. H., Brundell, J. B., & Rodger, C. J. (2012). Relative detection efficiency of the World Wide Lightning Location Network. *Radio Science*, *47*, RS6005. https://doi.org/10.1029/2012RS005049

Labanti, C., Marisaldi, M., Fuschino, F., Galli, M., Argan, A., Bulgarelli, A., et al. (2009). Design and construction of the mini-calorimeter of the AGILE satellite. *Nuclear Instruments and Methods in Physics Research Section A: Accelerators, Spectrometers, Detectors and Associated Equipment*, *598*(2), 470–479. https://doi.org/10.1016/j.nima.2008.09.021

Maiorana, C., Marisaldi, M., Lindanger, A., Østgaard, N., Ursi, A., Sarria, D., et al. (2020). The 3rd AGILE terrestrial gamma-ray flashes catalog. part ii: Optimized selection criteria and characteristics of the new sample to be submitted. *Journal of Geophysical Research: Atmospheres*.

Marisaldi, M., Argan, A., Ursi, A., Gjesteland, T., Fuschino, F., Labanti, C., et al. (2015). Enhanced detection of terrestrial gamma-ray flashes by AGILE. *Geophysical Research Letters*, *42*, 9481–9487. https://doi.org/10.1002/2015GL066100

Marisaldi, M., Fuschino, F., Labanti, C., Galli, M., Longo, F., Del Monte, E., et al. (2010). Detection of terrestrial gamma ray flashes up to 40 MeV by the AGILE satellite. *Journal of Geophysical Research*, *115*, A00E13. https://doi.org/10.1029/2009JA014502

Marisaldi, M., Fuschino, F., Tavani, M., Dietrich, S., Price, C., Galli, M., et al. (2014). Properties of terrestrial gamma ray flashes detected by AGILE mcal below 30 MeV. *Journal of Geophysical Research: Space Physics*, *119*, 1337–1355. https://doi.org/10.1002/2013JA019301

Marisaldi, M., Galli, M., Labanti, C., Østgaard, N., Sarria, D., Cummer, S. A., et al. (2019). On the high-energy spectral component and fine time structure of terrestrial gamma ray flashes. *Journal of Geophysical Research: Atmospheres*, *124*, 7484–7497. https://doi.org/10.1029/2019JD030554

Marshall, T., Stolzenburg, M., Karunarathne, S., Cummer, S., Lu, G., Betz, H.-D., et al. (2013). Initial breakdown pulses in intracloud lightning flashes and their relation to terrestrial gamma ray flashes. *Journal of Geophysical Research: Atmospheres*, *118*, 10,907–10,925. https://doi.org/10.1002/jgrd.50866

McTague, L. E., Cummer, S. A., Briggs, M. S., Connaughton, V., Stanbro, M., & Fitzpatrick, G. (2015). A lightning-based search for nearby observationally dim terrestrial gamma ray flashes. *Journal of Geophysical Research: Atmospheres*, *120*, 12,003–12,017. https://doi.org/10.1002/2015JD023475

Mezentsev, A., Østgaard, N., Gjesteland, T., Albrechtsen, K., Lehtinen, N., Marisaldi, M., et al. (2016). Radio emissions from double RHESSI TGFs. *Journal of Geophysical Research: Atmospheres*, *121*, 8006–8022. https://doi.org/10.1002/2016JD025111

Neubert, T., Østgaard, N., Reglero, V., Blanc, E., Chanrion, O., Oxborrow, C. A., et al. (2019). The ASIM mission on the international space station. *Space Science Reviews*, *215*(2), 26. https://doi.org/10.1007/s11214-019-0592-z

Østgaard, N., Albrecthsen, K. H., Gjesteland, T., & Collier, A. (2015). A new population of terrestrial gamma-ray flashes in the RHESSI data. *Geophysical Research Letters*, *42*, 10,937–10,942. https://doi.org/10.1002/2015GL067064

Østgaard, N., Gjesteland, T., Carlson, B. E., Collier, A. B., Cummer, S. A., Lu, G., & Christian, H. J. (2013). Simultaneous observations of optical lightning and terrestrial gamma ray flash from space. *Geophysical Research Letters*, *40*, 2423–2426. https://doi.org/10.1002/grl.50466

Picone, J. M., Hedin, A. E., Drob, D. P., & Aikin, A. C. (2002). Nrlmsise-00 empirical model of the atmosphere: Statistical comparisons and scientific issues. *Journal of Geophysical Research*, *107*(A12), SIA 15–1–SIA 15–16. https://doi.org/10.1029/2002JA009430

Roberts, O. J., Fitzpatrick, G., Stanbro, M., McBreen, S., Briggs, M. S., Holzworth, R. H., et al. (2018). The first Fermi-GBM terrestrial gamma ray flash catalog. *Journal of Geophysical Research: Space Physics*, *123*, 4381–4401. https://doi.org/10.1029/2017JA024837

Rodger, C. J., Brundell, J. B., Holzworth, R. H., & Lay, E. H. (2009). Growing detection efficiency of the world wide lightning location network. *AIP Conference Proceedings*, *1118*(1), 15–20. https://doi.org/10.1063/1.3137706

Rudlosky, S. D., & Shea, D. T. (2013). Evaluating WWLLN performance relative to TRMM/LIS. *Geophysical Research Letters*, *40*, 2344–2348. https://doi.org/10.1002/grl.50428

Sarria, D., Blelly, P.-L., & Forme, F. (2015). Mc-peptita: A Monte Carlo model for photon, electron and positron tracking in terrestrial atmosphere—Application for a terrestrial gamma ray flash. *Journal of Geophysical Research: Space Physics*, *120*, 3970–3986. https://doi.org/10.1002/2014JA020695

Sarria, D., Kochkin, P., Østgaard, N., Lehtinen, N., Mezentsev, A., Marisaldi, M., et al. (2019). The first terrestrial electron beam observed by the atmosphere-space interactions monitor. *Journal of Geophysical Research: Space Physics*, *124*, 10,497–10,511. https://doi.org/10.1029/2019JA027071

Sarria, D., Lebrun, F., Blelly, P.-L., Chipaux, R., Laurent, P., Sauvaud, J.-A., et al. (2017). Taranis XGRE and IDEE detection capability of terrestrial gamma-ray flashes and associated electron beams. *Geoscientific Instrumentation, Methods and Data Systems*, *6*(2), 239–256. https://doi.org/10.5194/gi-6-239-2017

Smith, D. M., Buzbee, P., Kelley, N. A., Infanger, A., Holzworth, R. H., & Dwyer, J. R. (2016). The rarity of terrestrial gamma-ray flashes: 2. RHESSI stacking analysis. *Journal of Geophysical Research: Atmospheres*, *121*, 11,382–11,404. https://doi.org/10.1002/2016JD025395

Smith, D. M., Hazelton, B. J., Grefenstette, B. W., Dwyer, J. R., Holzworth, R. H., & Lay, E. H. (2010). Terrestrial gamma ray flashes correlated to storm phase and tropopause height. *Journal of Geophysical Research*, *115*, A00E49. https://doi.org/10.1029/2009JA014853

Smith, D. M., Lopez, L. I., Lin, R. P., & Barrington-Leigh, C. (2005). Terrestrial gamma-ray flashes observed up to 20 MeV. *Science*, *307*, 1085–1088. https://doi.org/10.1126/science.1107466

Thébault, E., Finlay, C. C., Beggan, C. D., Alken, P., Aubert, J., Barrois, O., et al. (2015). International geomagnetic reference field: The 12th generation. *Earth, Planets and Space*, *67*(1), 79. https://doi.org/10.1186/s40623-015-0228-9

Ursi, A., Guidorzi, C., Marisaldi, M., Sarria, D., & Frontera, F. (2017). Terrestrial gamma-ray flashes in the BeppoSAX data archive. *Journal of Atmospheric and Solar-Terrestrial Physics*, *156*, 50–56. https://doi.org/10.1016/j.jastp.2017.02.014

Wessel, P., & Smith, WalterH. F. (1996). A global, self-consistent, hierarchical, high-resolution shoreline database. *Journal of Geophysical Research*, *101*(B4), 8741–8743. https://doi.org/10.1029/96JB00104

Bibliography

Abbasi, R. U., T. Abu-Zayyad, M. Allen, E. Barcikowski, J. W. Belz, D. R. Bergman, S. A. Blake, M. Byrne, R. Cady, B. Cheon, J. Chiba, M. Chikawa, T. Fujii, M. Fukushima, G. Furlich, T. Goto, W. Hanlon, Y. Hayashi, N. Hayashida, K. Hibino, K. Honda, D. Ikeda, N. Inoue, T. Ishii, H. Ito, D. Ivanov, S. Jeong, C. C. H. Jui, K. Kadota, F. Kakimoto, O. Kalashev, K. Kasahara, H. Kawai, S. Kawakami, K. Kawata, E. Kido, H. B. Kim, J. H. Kim, J. H. Kim, S. S. Kishigami, P. R. Krehbiel, V. Kuzmin, Y. J. Kwon, J. Lan, R. LeVon, J. P. Lundquist, K. Machida, K. Martens, T. Matuyama, J. N. Matthews, M. Minamino, K. Mukai, I. Myers, S. Nagataki, R. Nakamura, T. Nakamura, T. Nonaka, S. Ogio, M. Ohnishi, H. Ohoka, K. Oki, T. Okuda, M. Ono, R. Onogi, A. Oshima, S. Ozawa, I. H. Park, M. S. Pshirkov, J. Remington, W. Rison, D. Rodeheffer, D. C. Rodriguez, G. Rubtsov, D. Ryu, H. Sagawa, K. Saito, N. Sakaki, N. Sakurai, T. Seki, K. Sekino, P. Shah, F. Shibata, T. Shibata, H. Shimodaira, B. K. Shin, H. S. Shin, J. D. Smith, P. Sokolsky, R. W. Springer, B. T. Stokes, T. A. Stroman, H. Takai, M. Takeda, R. Takeishi, A. Taketa, M. Takita, Y. Tameda, H. Tanaka, K. Tanaka, M. Tanaka, R. J. Thomas, S. B. Thomas, G. B. Thomson, P. Tinyakov, I. Tkachev, H. Tokuno, T. Tomida, S. Troitsky, Y. Tsunesada, Y. Uchihori, S. Udo, F. Urban, G. Vasiloff, T. Wong, M. Yamamoto, R. Yamane, H. Yamaoka, K. Yamazaki, J. Yang, K. Yashiro, Y. Yoneda, S. Yoshida, H. Yoshii, and Z. Zundel (2018), Gamma ray showers observed at ground level in coincidence with downward lightning leaders, *Journal of Geophysical Research: Atmospheres*, *123*(13), 6864–6879, doi:https://doi.org/10.1029/2017JD027931. 3.1

Albrecht, R., S. Goodman, D. Buechler, R. Blakeslee, and H. Christian (2016), Lis 0.1 degree very high resolution gridded lightning climatology data collection. 4.4.1

Albrechtsen, K. H., N. Østgaard, N. Berge, and T. Gjesteland (2019), Observationally weak tgfs in the rhessi data, *Journal of Geophysical Research: Atmospheres*, *124*(1), 287–298, doi:https://doi.org/10.1029/2018JD029272. 3.2, 4.3

Babich, L., I. Kutsyk, E. Donskoy, and A. Kudryavtsev (1998), New data on space and time scales of relativistic runaway electron avalanche for thunderstorm environment: Monte carlo calculations, *Physics Letters A*, *245*(5), 460 – 470, doi:https://doi.org/10.1016/S0375-9601(98)00268-0. 3.3.1

Babich, L. P., and R. A. Roussel-Dupré (2007), Origin of neutron flux increases observed in correlation with lightning, *Journal of Geophysical Research: Atmospheres*, *112*(D13), doi: https://doi.org/10.1029/2006JD008340. 2.3

Behnke, S. A., R. J. Thomas, P. R. Krehbiel, and W. Rison (2005), Initial leader velocities during intracloud lightning: Possible evidence for a runaway breakdown effect, *Journal of Geophysical Research: Atmospheres*, *110*(D10), doi:https://doi.org/10.1029/2004JD005312. 4.1

Blakeslee, R. J., T. J. Lang, W. J. Koshak, D. Buechler, P. Gatlin, D. M. Mach, G. T. Stano, K. S. Virts, T. D. Walker, D. J. Cecil, W. Ellett, S. J. Goodman, S. Harrison, D. L. Hawkins, M. Heumesser, H. Lin, M. Maskey, C. J. Schultz, M. Stewart, M. Bateman, O. Chanrion, and H. Christian (2020), Three years of the lightning imaging sensor onboard the international space station: Expanded global coverage and enhanced applications, *Journal of Geophysical Research: Atmospheres*, *125*(16), e2020JD032,918, doi: https://doi.org/10.1029/2020JD032918, e2020JD032918 2020JD032918. 4.4.1

Boccippio, D. J., W. Koshak, R. Blakeslee, K. Driscoll, D. Mach, D. Buechler, W. Boeck, H. J. Christian, and S. J. Goodman (2000), The optical transient detector (otd): Instrument characteristics and cross-sensor validation, *Journal of Atmospheric and Oceanic Technology*, *17*(4), 441 – 458, doi:10.1175/1520-0426(2000)017<0441:TOTDOI>2.0.CO;2. 4.4.1

Briggs, M. S., S. Xiong, V. Connaughton, D. Tierney, G. Fitzpatrick, S. Foley, J. E. Grove, A. Chekhtman, M. Gibby, G. J. Fishman, S. McBreen, V. L. Chaplin, S. Guiriec, E. Layden, P. N. Bhat, M. Hughes, J. Greiner, A. Kienlin, R. M. Kippen, C. A. Meegan, W. S. Paciesas, R. D. Preece, C. Wilson-Hodge, R. H. Holzworth, and M. L. Hutchins (2013), Terrestrial gamma-ray flashes in the fermi era: Improved observations and analysis methods, *Journal of Geophysical Research: Space Physics*, *118*(6), 3805–3830, doi:10.1002/jgra.50205. 1, 3.1, 4.3

Carey, L. D., M. J. Murphy, T. L. McCormick, and N. W. S. Demetriades (2005), Lightning location relative to storm structure in a leading-line, trailing-stratiform mesoscale convective system, *Journal of Geophysical Research: Atmospheres*, *110*(D3), doi:https://doi.org/10.1029/2003JD004371. 2.1

Carlson, B. E., N. G. Lehtinen, and U. S. Inan (2007), Constraints on terrestrial gamma ray flash production from satellite observation, *Geophysical Research Letters*, *34*(8), doi:10.1029/2006GL029229. 3.2

Carlson, B. E., N. G. Lehtinen, and U. S. Inan (2009), Terrestrial gamma ray flash production by lightning current pulses, *Journal of Geophysical Research: Space Physics*, *114*(A12), doi:https://doi.org/10.1029/2009JA014531. 3.2

Cecil, D. J., E. J. Zipser, and S. W. Nesbitt (01 Apr. 2002), Reflectivity, ice scattering, and lightning characteristics of hurricane eyewalls and rainbands. part i: Quantitative description, *Monthly Weather Review*, *130*(4), 769 – 784, doi:10.1175/1520-0493(2002)130<0769:RISALC>2.0.CO;2. 4.2

Celestin, S., and V. P. Pasko (2011), Energy and fluxes of thermal runaway electrons produced by exponential growth of streamers during the stepping of lightning leaders and in transient luminous events, *Journal of Geophysical Research: Space Physics*, *116*(A3), doi:10.1029/2010JA016260. 3.3.3

Celestin, S., W. Xu, and V. P. Pasko (2012), Terrestrial gamma ray flashes with energies up to 100 mev produced by nonequilibrium acceleration of electrons in lightning, *Journal of Geophysical Research: Space Physics*, *117*(A5). 3.3.3

Celestin, S., W. Xu, and V. P. Pasko (2015), Variability in fluence and spectrum of high-energy photon bursts produced by lightning leaders, *Journal of Geophysical Research: Space Physics*, *120*(12), 10,712–10,723, doi:10.1002/2015JA021410. 3.2

Chanrion, O., T. Neubert, I. Lundgaard Rasmussen, C. Stoltze, D. Tcherniak, N. C. Jessen, J. Polny, P. Brauer, J. E. Balling, S. Savstrup Kristensen, S. Forchhammer, P. Hofmeyer, P. Davidsen, O. Mikkelsen, D. Bo Hansen, D. D. V. Bhanderi, C. G. Petersen, and M. Lorenzen (2019), The modular multispectral imaging array (mmia) of the asim payload on the international space station, *Space Science Reviews*, *215*(4), 28, doi:10.1007/s11214-019-0593-y. 3.1.1

Chilingarian, A., A. Daryan, K. Arakelyan, A. Hovhannisyan, B. Mailyan, L. Melkumyan, G. Hovsepyan, S. Chilingaryan, A. Reymers, and L. Vanyan (2010), Ground-based observations of thunderstorm-correlated fluxes of high-energy electrons, gamma rays, and neutrons, *Phys. Rev. D*, *82*, 043,009, doi:10.1103/PhysRevD.82.043009. 2.3

Christian, H. J., R. J. Blakeslee, D. J. Boccippio, W. L. Boeck, D. E. Buechler, K. T. Driscoll, S. J. Goodman, J. M. Hall, W. J. Koshak, D. M. Mach, and M. F. Stewart (2003), Global frequency and distribution of lightning as observed from space by the optical transient detector, *Journal of Geophysical Research: Atmospheres*, *108*(D1), ACL 4–1–ACL 4–15, doi:10.1029/2002JD002347. 4.3, 4.2

Chronis, T., K. Cummins, R. Said, W. Koshak, E. McCaul, E. R. Williams, G. T. Stano, and M. Grant (2015), Climatological diurnal variation of negative cg lightning peak current over the continental united states, *Journal of Geophysical Research: Atmospheres*, *120*(2), 582–589, doi:https://doi.org/10.1002/2014JD022547. 4.2

Chronis, T., M. S. Briggs, G. Priftis, V. Connaughton, J. Brundell, R. Holzworth, S. Heckman, S. McBreen, G. Fitzpatrick, and M. Stanbro (2016), Characteristics of thunderstorms that produce terrestrial gamma ray flashes, *Bulletin of the American Meteorological Society*, *97*(4), 639–653, doi:10.1175/BAMS-D-14-00239.1. 1.1, 4.2

Connaughton, V., M. S. Briggs, R. H. Holzworth, M. L. Hutchins, G. J. Fishman, C. A. Wilson-Hodge, V. L. Chaplin, P. N. Bhat, J. Greiner, A. von Kienlin, R. M. Kippen, C. A. Meegan, W. S. Paciesas, R. D. Preece, E. Cramer, J. R. Dwyer, and D. M. Smith (2010), Associations between fermi gamma-ray burst monitor terrestrial gamma ray flashes and sferics from the world wide lightning location network, *Journal of Geophysical Research: Space Physics*, *115*(A12), doi:https://doi.org/10.1029/2010JA015681. 4.1

Connaughton, V., M. S. Briggs, S. Xiong, J. R. Dwyer, M. L. Hutchins, J. E. Grove, A. Chekhtman, D. Tierney, G. Fitzpatrick, S. Foley, S. McBreen, P. N. Bhat, V. L. Chaplin, E. Cramer, G. J. Fishman, R. H. Holzworth, M. Gibby, A. Kienlin, C. A. Meegan, W. S. Paciesas, R. D. Preece, and C. Wilson-Hodge (2013), Radio signals from electron beams in terrestrial gamma ray flashes, *Journal of Geophysical Research: Space Physics*, *118*(5), 2313–2320, doi:10.1029/2012JA018288. 3.1.1, 4.1, 5.1.1, 5.1.2

Cooray, V. (2015), *An Introduction to Lightning*, Springer, doi:https://doi.org/10.1007/978-94-017-8938-7. 2.1, 2.2

Cummer, S. A., Y. Zhai, W. Hu, D. M. Smith, L. I. Lopez, and M. A. Stanley (2005), Measurements and implications of the relationship between lightning and terrestrial gamma ray flashes, *Geophysical research letters*, *32*(8). 1, 3.1, 4.1

Cummer, S. A., F. Lyu, M. S. Briggs, G. Fitzpatrick, O. J. Roberts, and J. R. Dwyer (2015), Lightning leader altitude progression in terrestrial gammaray flashes, *Geophysical Research Letters*, *42*(18), 7792–7798, doi:10.1002/2015GL065228. 4.1

Cummins, K. L., and M. J. Murphy (2009), An overview of lightning locating systems: History, techniques, and data uses, with an in-depth look at the u.s. nldn, *IEEE Transactions on Electromagnetic Compatibility*, *51*(3), 499–518, doi:10.1109/TEMC.2009.2023450. 4.3, 4.4.1

Dwyer, J. R. (2003), A fundamental limit on electric fields in air, *Geophysical research letters*, *30*(20), n/a–n/a. 1, 3.3.1, 3.3.2

Dwyer, J. R., and S. A. Cummer (2013), Radio emissions from terrestrial gamma-ray flashes, *Journal of Geophysical Research: Space Physics*, *118*(6), 3769–3790, doi:10.1002/jgra.50188. 3.1.1, 4.1

Dwyer, J. R., and D. M. Smith (2005), A comparison between monte carlo simulations of runaway breakdown and terrestrial gamma-ray flash observations, *Geophysical Research Letters*, *32*(22), doi:10.1029/2005GL023848. 3.1, 3.2

Dwyer, J. R., and D. M. Smith (2012), Deadly rays from clouds, *Scientific American*, *307*(2), 54–59. 3.6

Dwyer, J. R., and M. A. Uman (2014), The physics of lightning, *Physics reports*, *534*(4), 147–241. 2.2

Dwyer, J. R., M. A. Uman, H. K. Rassoul, M. Al-Dayeh, L. Caraway, J. Jerauld, V. A. Rakov, D. M. Jordan, K. J. Rambo, V. Corbin, and B. Wright (2003), Energetic radiation produced during rocket-triggered lightning, *Science*, *299*(5607), 694–697, doi:10.1126/science.1078940. 2.3

Dwyer, J. R., B. W. Grefenstette, and D. M. Smith (2008), High-energy electron beams launched into space by thunderstorms, *Geophysical Research Letters*, *35*(2), doi:https://doi.org/10.1029/2007GL032430. 2.3, 4.2

Dwyer, J. R., D. M. Smith, and S. A. Cummer (2012a), High-energy atmospheric physics: Terrestrial gamma-ray flashes and related phenomena, *Space Science Reviews*, *173*(1), 133–196, doi:10.1007/s11214-012-9894-0. 2.3, 3.5, 3.7

Dwyer, J. R., M. M. Schaal, E. Cramer, S. Arabshahi, N. Liu, H. K. Rassoul, J. D. Hill, D. M. Jordan, and M. A. Uman (2012b), Observation of a gamma-ray flash at ground level in association with a cloud-to-ground lightning return stroke, *Journal of Geophysical Research: Space Physics*, *117*(A10), doi:https://doi.org/10.1029/2012JA017810. 3.1

Eack, K. B., W. H. Beasley, W. D. Rust, T. C. Marshall, and M. Stolzenburg (1996), Initial results from simultaneous observation of x-rays and electric fields in a thunderstorm, *Journal of Geophysical Research: Atmospheres*, *101*(D23), 29,637–29,640, doi:https://doi.org/10.1029/96JD01705. 2.3

Enoto, T., Y. Wada, Y. Furuta, K. Nakazawa, T. Yuasa, K. Okuda, K. Makishima, M. Sato, Y. Sato, T. Nakano, D. Umemoto, and H. Tsuchiya (2017), Photonuclear reactions triggered by lightning discharge, *Nature*, *551*(7681), 481–484, doi:10.1038/nature24630. 2.3

Fabró, F., J. Montanyà, M. Marisaldi, O. A. van der Velde, and F. Fuschino (2015), Analysis of global terrestrial gamma ray flashes distribution and special focus on agile detections over south america, *Journal of Atmospheric and Solar-Terrestrial Physics*, *124*, 10 – 20, doi:https://doi.org/10.1016/j.jastp.2015.01.009. 4.2, 4.3

Fabró, F., J. Montanyà, O. A. van der Velde, N. Pineda, and E. R. Williams (2019), On the tgf/lightning ratio asymmetry, *Journal of Geophysical Research: Atmospheres*, *124*(12), 6518–6531, doi:https://doi.org/10.1029/2018JD030075. 4.3

Fishman, G. J., P. N. Bhat, R. Mallozzi, J. M. Horack, T. Koshut, C. Kouveliotou, G. N. Pendleton, C. A. Meegan, R. B. Wilson, W. S. Paciesas, S. J. Goodman, and H. J. Christian (1994), Discovery of intense gamma-ray flashes of atmospheric origin., *Science*, *264*(5163), 1313–1316. 1, 2.3, 3.1, 3.2

Fishman, G. J., M. S. Briggs, V. Connaughton, P. N. Bhat, W. S. Paciesas, A. von Kienlin, C. Wilson-Hodge, R. M. Kippen, R. Preece, C. A. Meegan, and J. Greiner (2011), Temporal properties of the terrestrial gamma-ray flashes from the gamma-ray burst monitor on the fermi observatory, *Journal of Geophysical Research: Space Physics*, *116*(A7), doi:https://doi.org/10.1029/2010JA016084. 3.1

Foley, S., G. Fitzpatrick, M. S. Briggs, V. Connaughton, D. Tierney, S. McBreen, J. R. Dwyer, V. L. Chaplin, P. N. Bhat, D. Byrne, E. Cramer, G. J. Fishman, S. Xiong, J. Greiner, R. M. Kippen, C. A. Meegan, W. S. Paciesas, R. D. Preece, A. von Kienlin, and C. Wilson-Hodge (2014), Pulse properties of terrestrial gamma-ray flashes detected by the fermi gamma-ray burst monitor, *Journal of Geophysical Research: Space Physics*, *119*(7), 5931–5942, doi:10.1002/2014JA019805. 3.2

Füllekrug, M. (2017), Introduction to lightning detection, *Weather*, *72*(2), 32–35, doi:https://doi.org/10.1002/wea.2810. 4.4.1

Fuschino, F., M. Marisaldi, C. Labanti, G. Barbiellini, E. Del Monte, A. Bulgarelli, M. Trifoglio, F. Gianotti, M. Galli, A. Argan, A. Trois, M. Tavani, E. Moretti, A. Giuliani, F. Longo, E. Costa, P. Caraveo, P. W. Cattaneo, A. Chen, F. D'Ammando, G. De Paris, G. Di Cocco, G. Di Persio, I. Donnarumma, Y. Evangelista, M. Feroci, A. Ferrari, M. Fiorini, I. Lapshov, F. Lazzarotto, P. Lipari, S. Mereghetti, A. Morselli, L. Pacciani, A. Pellizzoni, F. Perotti, P. Picozza, G. Piano, M. Pilia, M. Prest, G. Pucella, M. Rapisarda, A. Rappoldi, A. Rubini, S. Sabatini, P. Soffitta, E. Striani, E. Vallazza, S. Vercellone, V. Vittorini, A. Zambra, D. Zanello, L. Antonelli, S. Colafrancesco, S. Cutini, P. Giommi, F. Lucarelli, C. Pittori, P. Santolamazza, F. Verrecchia, and L. Salotti (2011), High spatial resolution correlation of agile tgfs and global lightning activity above the equatorial belt, *Geophysical Research Letters*, *38*(14), doi:10.1029/2011GL047817. 1.1

Gjesteland, T., N. Østgaard, P. H. Connell, J. Stadsnes, and G. J. Fishman (2010), Effects of dead time losses on terrestrial gamma ray flash measurements with the burst and transient source experiment, *Journal of Geophysical Research: Space Physics*, *115*(A5), doi:https://doi.org/10.1029/2009JA014578. 3.2

Gjesteland, T., N. Østgaard, S. Laviola, M. M. Miglietta, E. Arnone, M. Marisaldi, F. Fuschino, A. B. Collier, F. Fabró, and J. Montanya (2015), Observation of intrinsically bright terrestrial gamma ray flashes from the mediterranean basin, *Journal of Geophysical Research: Atmospheres*, *120*(23), 12,143–12,156, doi:10.1002/2015JD023704. 4.3

Grefenstette, B. W., D. M. Smith, J. R. Dwyer, and G. J. Fishman (2008), Time evolution of terrestrial gamma ray flashes, *Geophysical Research Letters*, *35*(6), doi:https://doi.org/10.1029/2007GL032922. 3.2

Grefenstette, B. W., D. M. Smith, B. J. Hazelton, and L. I. Lopez (2009), First rhessi terrestrial gamma ray flash catalog, *Journal of Geophysical Research: Space Physics*, *114*(A2), doi: 10.1029/2008JA013721. 3.1, 3.2

Gurevich, A. (1961), On the theory of runaway electrons, *Sov. Phys. JETP*, *12*(5), 904–912. 3.3.1

Gurevich, A., G. Milikh, and R. Roussel-Dupre (1992), Runaway electron mechanism of air breakdown and preconditioning during a thunderstorm, *Physics Letters A*, *165*(5), 463 – 468, doi:https://doi.org/10.1016/0375-9601(92)90348-P. 1, 3.3.1

Hare, B. M., M. A. Uman, J. R. Dwyer, D. M. Jordan, M. I. Biggerstaff, J. A. Caicedo, F. L. Carvalho, R. A. Wilkes, D. A. Kotovsky, W. R. Gamerota, J. T. Pilkey, T. K. Ngin, R. C. Moore, H. K. Rassoul, S. A. Cummer, J. E. Grove, A. Nag, D. P. Betten, and A. Bozarth (2016), Ground-level observation of a terrestrial gamma ray flash initiated by a triggered lightning, *Journal of Geophysical Research: Atmospheres*, *121*(11), 6511–6533, doi:https://doi.org/10.1002/2015JD024426. 3.1

Hazelton, B. J., B. W. Grefenstette, D. M. Smith, J. R. Dwyer, X.-M. Shao, S. A. Cummer, T. Chronis, E. H. Lay, and R. H. Holzworth (2009), Spectral dependence of terrestrial gamma-ray flashes on source distance, *Geophysical Research Letters*, *36*(1), doi: 10.1029/2008GL035906. 3.2

Hutchins, M. L., R. H. Holzworth, J. B. Brundell, and C. J. Rodger (2012), Relative detection efficiency of the world wide lightning location network, *Radio Science*, *47*(6), doi:https://doi.org/10.1029/2012RS005049. 4.4.1

Hutchins, M. L., R. H. Holzworth, K. S. Virts, J. M. Wallace, and S. Heckman (2013), Radiated vlf energy differences of land and oceanic lightning, *Geophysical Research Letters*, *40*(10), 2390–2394, doi:https://doi.org/10.1002/grl.50406. 4.2

Inan, U. S., S. C. Reising, G. J. Fishman, and J. M. Horack (1996), On the association of terrestrial gamma-ray bursts with lightning and implications for sprites, *Geophysical research letters*, *23*(9), 1017–1020. 1

Jayaratne, E. R., C. P. R. Saunders, and J. Hallett (1983), Laboratory studies of the charging of soft-hail during ice crystal interactions, *Quarterly Journal of the Royal Meteorological Society*, *109*(461), 609–630, doi:https://doi.org/10.1002/qj.49710946111. 2.1

Köhn, C., and U. Ebert (2015), Calculation of beams of positrons, neutrons, and protons associated with terrestrial gamma ray flashes, *Journal of Geophysical Research: Atmospheres*, *120*(4), 1620–1635. 3.3.3

Labanti, C., M. Marisaldi, F. Fuschino, M. Galli, A. Argan, A. Bulgarelli, G. Di Cocco, F. Gianotti, M. Tavani, and M. Trifoglio (2009), Design and construction of the mini-calorimeter of the agile satellite, *Nuclear Instruments and Methods in Physics Research Section A: Accelerators, Spectrometers, Detectors and Associated Equipment*, *598*(2), 470–479, doi: https://doi.org/10.1016/j.nima.2008.09.021. 3.1, 3.1.1

Larkey, R. K., J. G. Sample, D. M. Smith, M. S. Briggs, J. L. Lapierre, and R. H. Holzworth (2019), Evidence for extended charging periods prior to terrestrial gamma ray flashes, *Geophysical Research Letters*, *46*(17-18), 10,619–10,626, doi:https://doi.org/10.1029/2019GL083827. 1.1, 4.2

Lindanger, A., M. Marisaldi, C. Maiorana, D. Sarria, K. Albrechtsen, N. Østgaard, M. Galli, A. Ursi, C. Labanti, M. Tavani, C. Pittori, and F. Verrecchia (2020), The 3rd agile terrestrial gamma ray flash catalog. part i: Association to lightning sferics, *Journal of Geophysical Research: Atmospheres*, *125*(11), e2019JD031,985, doi:10.1029/2019JD031985, e2019JD031985 10.1029/2019JD031985. 1.1, 4.3

Lu, G., R. J. Blakeslee, J. Li, D. M. Smith, X.-M. Shao, E. W. McCaul, D. E. Buechler, H. J. Christian, J. M. Hall, and S. A. Cummer (2010), Lightning mapping observation of a terrestrial gamma-ray flash, *Geophysical Research Letters*, *37*(11), doi:https://doi.org/10.1029/2010GL043494. 4.1

Lyu, F., S. A. Cummer, and L. McTague (2015), Insights into high peak current in-cloud lightning events during thunderstorms, *Geophysical Research Letters*, *42*(16), 6836–6843, doi:https://doi.org/10.1002/2015GL065047. 4.1, 4.2

Lyu, F., S. A. Cummer, M. Briggs, M. Marisaldi, R. J. Blakeslee, E. Bruning, J. G. Wilson, W. Rison, P. Krehbiel, G. Lu, E. Cramer, G. Fitzpatrick, B. Mailyan, S. McBreen, O. J. Roberts, and M. Stanbro (2016), Ground detection of terrestrial gamma ray flashes from distant radio signals, *Geophysical Research Letters*, *43*(16), 8728–8734, doi:https://doi.org/10.1002/2016GL070154. 4.1

Mailyan, B. G., M. S. Briggs, E. S. Cramer, G. Fitzpatrick, O. J. Roberts, M. Stanbro, V. Connaughton, S. McBreen, P. N. Bhat, and J. R. Dwyer (2016), The spectroscopy of individual terrestrial gamma-ray flashes: Constraining the source properties, *Journal of Geophysical Research: Space Physics*, *121*(11), 11,346–11,363, doi:https://doi.org/10.1002/2016JA022702. 3.2

Mailyan, B. G., W. Xu, S. Celestin, M. S. Briggs, J. R. Dwyer, E. S. Cramer, O. J. Roberts, and M. Stanbro (2019), Analysis of individual terrestrial gamma-ray flashes with lightning leader models and fermi gamma-ray burst monitor data, *Journal of Geophysical Research: Space Physics*, *124*(8), 7170–7183, doi:https://doi.org/10.1029/2019JA026912. 3.2

Maiorana, C., M. Marisaldi, A. Lindanger, N. Østgaard, A. Ursi, D. Sarria, M. Galli, C. Labanti, M. Tavani, C. Pittori, and F. Verrecchia (2020), The 3rd agile terrestrial gamma-ray flashes catalog. part ii: Optimized selection criteria and characteristics of the new sample, *Journal of Geophysical Research: Atmospheres*, *125*(11), e2019JD031,986, doi:10.1029/2019JD031986, e2019JD031986 10.1029/2019JD031986. 1.1, 3.2, 4.2

Maiorana, C., M. Marisaldi, M. Füllekrug, S. Soula, J. Lapierre, A. Mezentsev, C. A. Skeie, M. Heumesser, O. Chanrion, N. Østgaard, T. Neubert, and V. Reglero (2021), Observation of tgfs at mid latitude. 1.1

Marisaldi, M., F. F., L. C., G. M., L. F., D. M. E., B. G., T. M., G. A., M. E., V. S., C. E., C. S., D. I., E. Y., F. M., L. I., L. F., L. P., M. S., P. L., R. M., S. P., T. M., A. A., B. F., B. A., C. P., C. P. W., C. A., C. V., D. F., D. P. G., D. C. G., D. P. G., F. A., F. M., F. T., G. F., M. A., P. A., P. F., P. P., P. G., P. M., P. M., P. G., R. A., R. A., S. S., S. E., T. A., V. E., V. V., Z. A., Z. D., A. L. A., C. S., G. D., G. P., P. C., P. B., S. P., V. F., and S. L. (2010), Detection of terrestrial gamma ray flashes up to 40 mev by the agile satellite, *Journal of Geophysical Research: Space Physics*, *115*(A3), doi:10.1029/2009JA014502. 1, 3.2

Marisaldi, M., F. Fuschino, M. Tavani, S. Dietrich, C. Price, M. Galli, C. Pittori, F. Verrecchia, S. Mereghetti, P. W. Cattaneo, S. Colafrancesco, A. Argan, C. Labanti, F. Longo, E. Del Monte, G. Barbiellini, A. Giuliani, A. Bulgarelli, R. Campana, and A. Chen (2014), Properties of terrestrial gamma ray flashes detected by agile mcal below 30 mev, *Journal of geophysical research. Space physics.*, *119*(2), 1337–1355. 3.2

Marisaldi, M., A. Argan, A. Ursi, T. Gjesteland, F. Fuschino, C. Labanti, M. Galli, M. Tavani, C. Pittori, F. Verrecchia, F. D'Amico, N. Østgaard, S. Mereghetti, R. Campana, P. Cattaneo, A. Bulgarelli, S. Colafrancesco, S. Dietrich, F. Longo, and F. Gianotti (2015), Enhanced detection of terrestrial gamma-ray flashes by agile, *Geophysical research letters*, *42*(21), 9481–9487. 3.1.1, 5.1.1

Marisaldi, M., M. Galli, C. Labanti, N. Østgaard, D. Sarria, S. A. Cummer, F. Lyu, A. Lindanger, R. Campana, A. Ursi, M. Tavani, F. Fuschino, A. Argan, A. Trois, C. Pittori, and F. Verrecchia (2019), On the high-energy spectral component and fine time structure of terrestrial gamma-ray flashes, *Journal of Geophysical Research: Atmospheres*, *0*(ja), doi: 10.1029/2019JD030554. 3.2

Marshall, T., M. Stolzenburg, S. Karunarathne, S. Cummer, G. Lu, H.-D. Betz, M. Briggs, V. Connaughton, and S. Xiong (2013), Initial breakdown pulses in intracloud lightning flashes and their relation to terrestrial gamma ray flashes, *Journal of Geophysical Research: Atmospheres*, *118*(19), 10,907–10,925, doi:https://doi.org/10.1002/jgrd.50866. 4.1

Marshall, T. C., and W. D. Rust (1991), Electric field soundings through thunderstorms, *Journal of Geophysical Research: Atmospheres*, *96*(D12), 22,297–22,306, doi:https://doi.org/10.1029/91JD02486. 2.1

McCarthy, M., and G. K. Parks (1985), Further observations of x-rays inside thunderstorms, *Geophysical Research Letters*, *12*(6), 393–396, doi:https://doi.org/10.1029/GL012i006p00393. 2.3

Meek, J. M. (1940), A theory of spark discharge, *Phys. Rev.*, *57*, 722–728, doi:10.1103/PhysRev.57.722. 2.2

Mezentsev, A., N. Østgaard, T. Gjesteland, K. Albrechtsen, N. Lehtinen, M. Marisaldi, D. Smith, and S. Cummer (2016), Radio emissions from double rhessi tgfs, *Journal of Geophysical Research: Atmospheres*, *121*(13), 8006–8022, doi:10.1002/2016JD025111. 3.2

Moore, C. B., K. B. Eack, G. D. Aulich, and W. Rison (2001), Energetic radiation associated with lightning stepped-leaders, *Geophysical Research Letters*, *28*(11), 2141–2144, doi: https://doi.org/10.1029/2001GL013140. 2.3

Moss, G. D., V. P. Pasko, N. Liu, and G. Veronis (2006), Monte carlo model for analysis of thermal runaway electrons in streamer tips in transient luminous events and streamer zones of lightning leaders, *Journal of Geophysical Research: Space Physics*, *111*(A2), doi: 10.1029/2005JA011350. 3.3.3

Neubert, T., N. Østgaard, V. Reglero, E. Blanc, O. Chanrion, C. A. Oxborrow, A. Orr, M. Tacconi, O. Hartnack, and D. D. V. Bhanderi (2019), The asim mission on the international space station, *Space Science Reviews*, *215*(2), 26, doi:10.1007/s11214-019-0592-z. 1, 3.1.1

Neubert, T., N. Østgaard, V. Reglero, O. Chanrion, M. Heumesser, K. Dimitriadou, F. Christiansen, C. Budtz-Jørgensen, I. Kuvvetli, I. L. Rasmussen, A. Mezentsev, M. Marisaldi, K. Ullaland, G. Genov, S. Yang, P. Kochkin, J. Navarro-Gonzalez, P. H. Connell, and C. J. Eyles (2020), A terrestrial gamma-ray flash and ionospheric ultraviolet emissions powered by lightning, *Science*, *367*(6474), 183–186, doi:10.1126/science.aax3872. 2.3

Østgaard, N., T. Gjesteland, R. S. Hansen, A. B. Collier, and B. Carlson (2012), The true fluence distribution of terrestrial gamma flashes at satellite altitude, *Journal of Geophysical Research: Space Physics*, *117*(A3), doi:https://doi.org/10.1029/2011JA017365. 3.2

Østgaard, N., T. Gjesteland, B. E. Carlson, A. B. Collier, S. A. Cummer, G. Lu, and H. J. Christian (2013), Simultaneous observations of optical lightning and terrestrial gamma ray flash from space, *Geophysical Research Letters*, *40*(10), 2423–2426, doi:https://doi.org/10. 1002/grl.50466. 4.1

Østgaard, N., J. E. Balling, T. Bjørnsen, P. Brauer, C. Budtz-Jørgensen, W. Bujwan, B. Carlson, F. Christiansen, P. Connell, C. Eyles, D. Fehlker, G. Genov, P. Grudziński, P. Kochkin, A. Kohfeldt, I. Kuvvetli, P. L. Thomsen, S. M. Pedersen, J. Navarro-Gonzalez, T. Neubert, K. Njøten, P. Orleanski, B. H. Qureshi, L. R. Cenkeramaddi, V. Reglero, M. Reina, J. M. Rodrigo, M. Rostad, M. D. Sabau, S. S. Kristensen, Y. Skogseide, A. Solberg, J. Stadsnes, K. Ullaland, and S. Yang (2019a), The modular x- and gamma-ray sensor (mxgs) of the asim payload on the international space station, *Space Science Reviews*, *215*(2), 23, doi: 10.1007/s11214-018-0573-7. 3.2, 3.1.1

Østgaard, N., T. Neubert, V. Reglero, K. Ullaland, S. Yang, G. Genov, M. Marisaldi, A. Mezentsev, P. Kochkin, N. Lehtinen, D. Sarria, B. H. Qureshi, A. Solberg, C. Maiorana, K. Albrechtsen, C. Budtz-Jørgensen, I. Kuvvetli, F. Christiansen, O. Chanrion, M. Heumesser, J. Navarro-Gonzalez, P. Connell, C. Eyles, H. Christian, and S. Al-nussirat (2019b), First 10 months of tgf observations by asim, *Journal of Geophysical Research: Atmospheres*, *124*(24), 14,024–14,036, doi:10.1029/2019JD031214. 3.2, 3.4, 4.1

Østgaard, N., H. J. Christian, J. E. Grove, D. Sarria, A. Mezentsev, P. Kochkin, N. Lehtinen, M. Quick, S. Al-Nussirat, E. Wulf, G. Genov, K. Ullaland, M. Marisaldi, S. Yang, and R. J. Blakeslee (2019c), Gamma ray glow observations at 20-km altitude, *Journal of Geophysical Research: Atmospheres*, *124*(13), 7236–7254, doi:https://doi.org/10.1029/2019JD030312. 4.2

Pu, Y., S. A. Cummer, F. Lyu, M. Briggs, B. Mailyan, M. Stanbro, and O. Roberts (2019), Low frequency radio pulses produced by terrestrial gamma-ray flashes, *Geophysical Research Letters*, *46*(12), 6990–6997, doi:https://doi.org/10.1029/2019GL082743. 4.1

Rakov, V., and M. Uman (2007), *Lightning: physics and effects*, Cambridge University Press. 2.2, 2.2, 3.3.1

Roberts, O. J., G. Fitzpatrick, G. Priftis, K. Bedka, T. Chronis, S. McBreen, M. S. Briggs, E. Cramer, B. Mailyan, and M. Stanbro (2017), Terrestrial gamma ray flashes due to particle acceleration in tropical storm systems, *Journal of Geophysical Research: Atmospheres*, *122*(6), 3374–3395, doi:https://doi.org/10.1002/2016JD025799. 3.2, 4.2, 4.3

Saunders, C. (2008), Charge separation mechanisms in clouds, *Space Science Reviews*, *137*(1-4), 335. 2.1, 2.1

Shah, G. N., H. Razdan, C. L. Bhat, and Q. M. Ali (1985), Neutron generation in lightning bolts, *Nature*, *313*(6005), 773–775, doi:10.1038/313773a0. 2.3

Shao, X.-M., T. Hamlin, and D. M. Smith (2010), A closer examination of terrestrial gamma-ray flash-related lightning processes, *Journal of Geophysical Research: Space Physics*, *115*(A6), doi:https://doi.org/10.1029/2009JA014835. 4.1

Sherwood, S. C., J.-H. Chae, P. Minnis, and M. McGill (2004), Underestimation of deep convective cloud tops by thermal imagery, *Geophysical Research Letters*, *31*(11), doi:https://doi.org/10.1029/2004GL019699. 4.4.2

Skeltved, A. B., N. Østgaard, A. Mezentsev, N. Lehtinen, and B. Carlson (2017), Constraints to do realistic modeling of the electric field ahead of the tip of a lightning leader, *Journal of Geophysical Research: Atmospheres*, *122*(15), 8120–8134, doi:https://doi.org/10.1002/2016JD026206. 3.2

Smith, D. M., L. I. Lopez, R. P. Lin, and C. Barrington-Leigh (2005), Terrestrial gamma-ray flashes observed up to 20 mev, *Science (New York, N.Y.)*, *307*, 1085–8, doi:10.1126/science.1107466. 1, 3.2

Smith, D. M., B. J. Hazelton, B. W. Grefenstette, J. R. Dwyer, R. H. Holzworth, and E. H. Lay (2010), Terrestrial gamma ray flashes correlated to storm phase and tropopause height, *Journal of geophysical research*, *115*(A8). 1.1, 3.1, 4.2, 4.3, 6.1

Smith, D. M., J. R. Dwyer, B. J. Hazelton, B. W. Grefenstette, G. F. M. Martinez-McKinney, Z. Y. Zhang, A. W. Lowell, N. A. Kelley, M. E. Splitt, S. M. Lazarus, W. Ulrich, M. Schaal, Z. H. Saleh, E. Cramer, H. Rassoul, S. A. Cummer, G. Lu, X.-M. Shao, C. Ho, T. Hamlin, R. J. Blakeslee, and S. Heckman (2011), A terrestrial gamma ray flash observed from an aircraft, *Journal of Geophysical Research: Atmospheres*, *116*(D20), doi:https://doi.org/10.1029/2011JD016252. 4.2

Smith, D. M., P. Buzbee, N. A. Kelley, A. Infanger, R. H. Holzworth, and J. R. Dwyer (2016), The rarity of terrestrial gamma-ray flashes: 2. rhessi stacking analysis, *Journal of Geophysical Research: Atmospheres*, *121*(19), 11,382–11,404, doi:https://doi.org/10.1002/2016JD025395. 4.2

Smith, D. M., N. A. Kelley, P. Buzbee, A. Infanger, M. Splitt, R. H. Holzworth, and J. R. Dwyer (2020), Special classes of terrestrial gamma ray flashes from rhessi, *Journal of Geophysical Research: Atmospheres*, *125*(20), e2020JD033,043, doi:https://doi.org/10.1029/2020JD033043, e2020JD033043 10.1029/2020JD033043. 3.1, 3.2, 4.2

Smith, W. L., and C. M. R. Platt (1978), Comparison of satellite-deduced cloud heights with indications from radiosonde and ground-based laser measurements, *Journal of Applied Meteorology and Climatology*, *17*(12), 1796 – 1802, doi:10.1175/1520-0450(1978)017<1796:COSDCH>2.0.CO;2. 4.4.2

Splitt, M. E., S. M. Lazarus, D. Barnes, J. R. Dwyer, H. K. Rassoul, D. M. Smith, B. Hazelton, and B. Grefenstette (2010), Thunderstorm characteristics associated with rhessi identified terrestrial gamma ray flashes, *Journal of geophysical research*, *115*(A6). 1.1, 4.2, 4.3

Stanley, M. A., X.-M. Shao, D. M. Smith, L. I. Lopez, M. B. Pongratz, J. D. Harlin, M. Stock, and A. Regan (2006), A link between terrestrial gamma-ray flashes and intracloud lightning discharges, *Geophysical Research Letters*, *33*(6), doi:https://doi.org/10.1029/2005GL025537. 4.1

Takahashi, T. (1978), Riming electrification as a charge generation mechanism in thunderstorms, *Journal of Atmospheric Sciences*, *35*(8), 1536 – 1548, doi:10.1175/1520-0469(1978)035<1536:REAACG>2.0.CO;2. 2.1

Tavani, M., G. Barbiellini, A. Argan, F. Boffelli, A. Bulgarelli, P. Caraveo, P. W. Cattaneo, A. W. Chen, V. Cocco, E. Costa, F. D'Ammando, E. Del Monte, G. De Paris, G. Di Cocco, G. Di Persio, I. Donnarumma, Y. Evangelista, M. Feroci, A. Ferrari, M. Fiorini, F. Fornari, F. Fuschino, T. Froysland, M. Frutti, M. Galli, F. Gianotti, A. Giuliani, C. Labanti, I. Lapshov, F. Lazzarotto, F. Liello, P. Lipari, F. Longo, E. Mattaini, M. Marisaldi, M. Mastropietro, A. Mauri, F. Mauri, S. Mereghetti, E. Morelli, A. Morselli, L. Pacciani, A. Pellizzoni, F. Perotti, G. Piano, P. Picozza, C. Pontoni, G. Porrovecchio, M. Prest, G. Pucella, M. Rapisarda, A. Rappoldi, E. Rossi, A. Rubini, P. Soffitta, A. Traci, M. Trifoglio, A. Trois, E. Vallazza, S. Vercellone, V. Vittorini, A. Zambra, D. Zanello, C. Pittori, B. Preger, P. Santolamazza, F. Verrecchia, P. Giommi, S. Colafrancesco, A. Antonelli, S. Cutini, D. Gasparrini, S. Stellato, G. Fanari, R. Primavera, F. Tamburelli, F. Viola, G. Guarrera, L. Salotti, F. D'Amico, E. Marchetti, M. Crisconio, P. Sabatini, G. Annoni, S. Alia, A. Longoni, R. Sanquerin, M. Battilana, P. Concari, E. Dessimone, R. Grossi, A. Parise, F. Monzani, E. Artina, R. Pavesi, G. Marseguerra, L. Nicolini, L. Scandelli, L. Soli, V. Vettorello, E. Zardetto, A. Bonati, L. Maltecca, E. D'Alba, M. Patané, G. Babini, F. Onorati, L. Acquaroli, M. Angelucci, B. Morelli, C. Agostara, M. Cerone, A. Michetti, P. Tempesta, S. D'Eramo, F. Rocca, F. Giannini, G. Borghi, B. Garavelli, M. Conte, M. Balasini, I. Ferrario, M. Vanotti, E. Collavo, and M. Giacomazzo (2009), The agile mission, *A&A*, *502*(3), 995–1013, doi:10.1051/0004-6361/200810527. 3.1.1

Tavani, M., M. Marisaldi, C. Labanti, F. Fuschino, A. Argan, A. Trois, P. Giommi, S. Colafrancesco, C. Pittori, F. Palma, M. Trifoglio, F. Gianotti, A. Bulgarelli, V. Vittorini, F. Verrecchia, L. Salotti, G. Barbiellini, P. Caraveo, P. W. Cattaneo, A. Chen, T. Contessi, E. Costa, F. D'Ammando, E. Del Monte, G. De Paris, G. Di Cocco, G. Di Persio, I. Donnarumma, Y. Evangelista, M. Feroci, A. Ferrari, M. Galli, A. Giuliani, M. Giusti, I. Lapshov, F. Lazzarotto, P. Lipari, F. Longo, S. Mereghetti, E. Morelli, E. Moretti, A. Morselli, L. Pacciani, A. Pellizzoni, F. Perotti, G. Piano, P. Picozza, M. Pilia, G. Pucella, M. Prest, M. Rapisarda, A. Rappoldi, E. Rossi, A. Rubini, S. Sabatini, E. Scalise, P. Soffitta, E. Striani, E. Vallazza, S. Vercellone, A. Zambra, and D. Zanello (2011), Terrestrial gamma-ray flashes as powerful particle accelerators, *Phys. Rev. Lett.*, *106*, 018,501, doi:10.1103/PhysRevLett.106.018501. 3.2

Thornton, J. A., K. S. Virts, R. H. Holzworth, and T. P. Mitchell (2017), Lightning enhancement over major oceanic shipping lanes, *Geophysical Research Letters*, *44*(17), 9102–9111, doi:https://doi.org/10.1002/2017GL074982. 4.3

Tierney, D., M. S. Briggs, G. Fitzpatrick, V. L. Chaplin, S. Foley, S. McBreen, V. Connaughton, S. Xiong, D. Byrne, M. Carr, P. N. Bhat, G. J. Fishman, J. Greiner, R. M. Kippen, C. A. Meegan, W. S. Paciesas, R. D. Preece, A. von Kienlin, and C. Wilson-Hodge (2013), Fluence distribution of terrestrial gamma ray flashes observed by the fermi gamma-

ray burst monitor, *Journal of Geophysical Research: Space Physics*, *118*(10), 6644–6650, doi:https://doi.org/10.1002/jgra.50580. 3.2

Tran, M., V. Rakov, S. Mallick, J. Dwyer, A. Nag, and S. Heckman (2015), A terrestrial gamma-ray flash recorded at the lightning observatory in gainesville, florida, *Journal of Atmospheric and Solar-Terrestrial Physics*, *136*, 86–93, doi:https://doi.org/10.1016/j.jastp.2015.10.010, advances in Lightning Research. 3.1

Tsuchiya, H., T. Enoto, S. Yamada, T. Yuasa, K. Nakazawa, T. Kitaguchi, M. Kawaharada, M. Kokubun, H. Kato, M. Okano, and K. Makishima (2011), Long-duration ray emissions from 2007 and 2008 winter thunderstorms, *Journal of Geophysical Research: Atmospheres*, *116*(D9), doi:https://doi.org/10.1029/2010JD015161. 2.3

Ursi, A., M. Marisaldi, S. Dietrich, M. Tavani, A. Tiberia, and F. Porcù (2019), Analysis of thunderstorms producing terrestrial gamma ray flashes with the meteosat second generation, *Journal of Geophysical Research: Atmospheres*, *124*(23), 12,667–12,682, doi:10.1029/2018JD030149. 1.1, 4.2

Vonnegut, B., C. B. Moore, R. G. Semonin, J. W. Bullock, D. W. Staggs, and W. E. Bradley (1962), Effect of atmospheric space charge on initial electrification of cumulus clouds, *Journal of Geophysical Research (1896-1977)*, *67*(10), 3909–3922, doi:https://doi.org/10.1029/JZ067i010p03909. 2.1

Williams, E., R. Boldi, J. Bór, G. Sátori, C. Price, E. Greenberg, Y. Takahashi, K. Yamamoto, Y. Matsudo, Y. Hobara, M. Hayakawa, T. Chronis, E. Anagnostou, D. M. Smith, and L. Lopez (2006), Lightning flashes conducive to the production and escape of gamma radiation to space, *Journal of Geophysical Research: Atmospheres*, *111*(D16), doi:10.1029/2005JD006447. 4.1, 4.2, 5.1.3, 6.1

Williams, E. R., M. E. Weber, and R. E. Orville (1989), The relationship between lightning type and convective state of thunderclouds, *Journal of Geophysical Research: Atmospheres*, *94*(D11), 13,213–13,220, doi:https://doi.org/10.1029/JD094iD11p13213. 2.1

Wilson, C. T. R. (1920), Investigations on lightning discharges and on the electric field of thunderstorms, *Phylosophical Transactions*, *221*, 73–115. 1, 2.1

Wilson, C. T. R. (1925), The acceleration of -particles in strong electric fields such as those of thunderclouds, *Mathematical Proceedings of the Cambridge Philosophical Society*, *22*(4), 534538, doi:10.1017/S0305004100003236. 3.3.1

Wu, T., S. Yoshida, T. Ushio, Z. Kawasaki, and D. Wang (2014), Lightning-initiator type of narrow bipolar events and their subsequent pulse trains, *Journal of Geophysical Research: Atmospheres*, *119*(12), 7425–7438, doi:https://doi.org/10.1002/2014JD021842. 4.1

Østgaard, N., T. Gjesteland, J. Stadsnes, P. H. Connell, and B. Carlson (2008), Production altitude and time delays of the terrestrial gamma flashes: Revisiting the burst and transient source experiment spectra, *Journal of Geophysical Research: Space Physics*, *113*(A2), doi: https://doi.org/10.1029/2007JA012618. 3.2

uib.no